UNIVERSITÁ DEGLI STUDI DI PARMA

Facoltá di Scienze Matematiche Fisiche Naturali

Dottorato di Ricerca in Scienza e Tecnologia dei Materiali Innovativi.
Ciclo XXIV- Anno: 2012

Heterostructures based on $L1_0$-FePt for spintronics and magnetic recording.

Coordinatore:
Chiar.mo Prof. Enrico Dalcanale.

Tutor:
Dott.ssa Franca Albertini.
Dott.ssa Francesca Casoli.

Dottorando: Pierpaolo Lupo

Introduction

Nowadays, the challenges of nanoscience and nanotechnology open a scientific field in which physicists, materials scientists, chemists, biologist and engineers practice together to found new discoveries that can change our way of life. This new promising field introduces the great possibility to engineer material characteristics and also to exploit new physical phenomena fitting the final application demand. All of the greatest goals for nanoscience are dependent upon materials and the reliable ways to fabricate nanostructures, thus these aspects have to be faced to obtain significant technological progress. Due to the rapid improvement in the fabrication of nanostructures, it is now possible to realize a broad variety of shapes and architectures. The outcomes have been exploited in many research fields from biology to solid state physics. In particular concerning magnetism, the combination between the wide range of nanostructure geometries and the choice of magnetic materials has introduced new challenges, unveiling interesting physical phenomena at the nanoscale, and has led to many developments in magnetic recording media [1, 2, 3], micro-electro-mechanical technology [4], and more recently spintronic devices [5, 6].

This Thesis is focused on the design, growth and characterization of thin films and heterostructures, based on FePt, with potential applications in magnetic recording [7] and spintronics [8], where the nanometric scale phenomena play a important role.

With this aim, heterostructures with peculiar properties like high perpendicular anisotropy, exchange-spring effect, magnetoresistance and spin polarization have been developed. The studied systems have been produced mainly by means of physical deposition techniques, such as radio frequency sputtering and pulsed laser deposition. The structural, morphological and magnetic studies have been performed through a variety of techniques, allowing a constant feedback with the design and preparation of materials.

This work has involved a considerable effort to reach a better understanding of various

and innovative scientific aspects. The study of new nanocomposites recording media, based on FePt, has highlighted the dependence of the exchange-spring behavior on the soft magnetic layer properties. For example, varying its thickness and chemical composition it is possible to change the effect of exchange interaction between hard and soft layers. Furthermore, the lattice mismatching with the substrate, which influences the morphology and chemical order of the nanostructure, can be exploited to tailor the magnetic behavior. Moreover, ion irradiation on $L1_0$-FePt thin film has been studied as possible technique to develop exchange-spring media with suitable characteristics closely defined by the irradiation parameters. The objective is to study innovative perpendicular recording media that exploit the exchange-spring interaction between a hard and soft magnetic phase, in bilayers or graded systems, to increase the storage density in future hard disks. In spintronics, the original choice of ferromagnetic electrodes (i.e., $L1_0$-FePt and Fe_3O_4) and their magnetization configuration in the heterostructure for magnetic tunnel junctions (MTJs) has led to deepen the extrinsic properties effects on the electrical transport through the tunnel barrier and on tunnel magnetic resistance. The inverse tunneling effect, as expected for Fe_3O_4/MgO interface, has been studied as a function of film thickness and junction area. The perpendicular direction between the easy magnetization axes of the electrodes gives rise to a suitable configuration in spin-torque devices [9].

The first part of my work (chapter 3) starts describing the optimization of thin films growth conditions, with emphasis on $L1_0$-FePt films grown on MgO and $SrTiO_3$ substrates, studying the correlation among morphology, magnetism, crystalline order and substrate lattice mismatch. Chapter number 4 describes the next implementation of FePt layers with optimized properties, tailored interfaces and morphology in nanostructures for future recording media. Moreover, a numerical micromagnetic model is proposed to describe the reversal magnetization mechanism in these systems. The final chapter (number 5) is focused to the growth and characterization of heterostructures, based on $L1_0$-FePt, and their lithography process in order to obtain MTJs with new characteristics for application in spintronics.

The first chapter presents some basic concepts of magnetism, in order to understand the underlying physics and a brief summary of the employed experimental techniques is given in the second chapter.

Contents

1

Elements of Magnetism

1.1 Magnetic Free Energy

Ferromagnetic materials are characterized by long-range ordering of their magnetic moments, which are aligned parallel to each other and show a spontaneous magnetization, even without applying an external magnetic field, which vanishes above the ordering Curie Temperature (T_c). Thus, any satisfactory theory must explain experimental features such as the existence of the spontaneous magnetization, the value of the transition temperature and the associate thermal phenomena. The total free energy of a ferromagnetic specimen in an applied magnetic field may be written as the sum of several free energy terms

$$E_T = E_{ex} + E_{anis} + E_{demag} + E_H + E_0 \tag{1.1}$$

where E_{ex} is the exchange energy, E_{anis} is the anisotropy energy, E_{demag} is the demagnetizing energy, E_H is the Zeeman contribution at the applied field H and E_0 represents any other contribution to the free energy that may be present. In this chapter we will discuss briefly these magnetic interactions, which are responsible for the properties of ferromagnetic materials. We will start our considerations with the exchange interaction, which is a pure quantum mechanical effect and is due to the Coulomb interaction and Pauli exclusion principle. Subsequently, we will discuss the anisotropy and then the demagnetizing energy.

1.1.1 Exchange Energy

In this section we will discuss different types of magnetic interaction which are responsible for properties which base on the fact that magnetic moments feel each other. As

result, a magnetic long range order can occur. We will start our considerations with the *exchange interaction* which is a pure quantum mechanical effect and is due to the Coulomb interaction and Pauli exclusion principle. Depending on the distance between the magnetic moments we distinguish between the direct and indirect exchange. The situation that the electrons of neighboring magnetic atoms directly interact is called direct exchange because the interaction is present without needing of any other intermediate species (i.e. atoms or molecules). If the overlap of the involved wave functions is only small (e.g. for rare earth metal atoms with their localized 4f electrons) then the direct exchange does not represent the dominating mechanism for magnetic properties. For this class of systems the indirect exchange interaction is responsible for magnetism. The idea that spontaneous magnetization is due to the interactions between magnetic moments was proposed by Weiss but the dipolar interaction he had in mind proved to be too small to account for the observed transition temperatures. It was not until the arrival of quantum theory by which Heisenberg and others showed that the interactions have a quantum mechanical origin and they are a direct consequence of the restriction places on the wave functions by the Pauli principle. Specifically, this principle requires that the electronic wave functions be antisymmetric with respect to exchange of space and spin coordinates of a pair of electrons, and it turns out that such a requirement makes the energy eigenvalues depend on the relative spin orientations of the electrons; this effect can then be interpreted in terms of an interaction which tends to orient the spin angular momenta (and consequently, the magnetic moments) of the atoms. The origin of this interaction can be seen in the quantum-mechanics of two electron system approach with spin value $S = \frac{1}{2}$. Considering the electrostatic interaction energy between two electrons as perturbation and taking into account the Pauli principle, only two energy level are possible. One singlet state with total spin $S_{tot} = 0$ and energy $E_s = E_0 + K_{12} + J_{12}$, and one triplet state with $S_{tot} = 1$ and energy $E_t = E_0 + K_{12} - J_{12}$, where $K_{12} = average\, Coulomb\, interaction$ and $J_{12} = exchange\, integral$. Thus the singlet and triplet energies are now different; whether the singlet state(spin $\uparrow\downarrow$) or triplet state (spin $\uparrow\uparrow$) has the lower state and the ground state depends on the sign of J_{12}. The difference in energy between the two state is $\Delta E_{ST} = E_s - E_t = 2J_{12}$, and if $J_{12} > 0$ the ground state is the triplet state (spin $\uparrow\uparrow$). In 1928, Dirac showed that the spin-dependent contributions to the energy arising from the Pauli principle may be

regarded as a two-body spin-spin interaction of the form:

$$H_{Heis} = -2\sum_{i<j} J_{ij}\vec{S}_i \cdot \vec{S}_j \tag{1.2}$$

This operator is known as the *Heisenberg Hamiltonian*. Here J_{ij} is the exchange integral for the couple of ions i and j with total spin moment S_i. By regarding the operators as classical spins, we can see in a qualitative way that parallel or antiparallel alignment of the spin is favored according to whether if $J > 0$ or if $J < 0$. It worthwhile to underline that the the exchange interaction is isotropic. Taking into consideration only crystals with a single kind of magnetic atom with all magnetic lattice sites equivalent and assuming that the exchange interactions fall off rapidly with increasing distance, we can extract, from the previous equation, a single atom Hamiltonian in which an atom i interacts with its j nearest neighbors. Following this way it is possible to introduce the molecular field approximation, already suggested by Weiss, which leads to a good physical explanation of the macroscopic phenomena governed by exchange-interaction. It is assumed that all the operators S_j, with $j \neq i$, are replaced their mean value. Thus, exchange among spins is reduced to the interaction with a mean magnetic field (H_M), called molecular field,

$$E_{ex} = -\mu_m \cdot H_{eff} = g\mu_B \vec{S_i} \cdot \vec{H_M} \tag{1.3}$$

with

$$H_M = \frac{2J}{g\mu_B}\sum_j S_j \cong \frac{2zJ}{g\mu_B} < \vec{S_j} >= \frac{2zJ}{Ng^2\mu_B^2}\vec{M} \tag{1.4}$$

since the mean value of $< \vec{S_j} >$ is related to the total magnetic moment of the crystal by $\vec{M} = Ng\mu_B < \vec{S_j} >$, and only the exchange interaction ($J = J_{ex}$) is considered along the z-axis. The molecular field approximation (MFA) predicts the critical transition temperature from the ferromagnetic to the paramagnetic state which are qualitatively in agreement with experimental observations. The MFA, using a quantized Brillouin function, gives a surprisingly good qualitative picture of the most important physical properties of a ferromagnet, namely, the spontaneous magnetization, and its temperature dependence. However when a more detailed comparison is made between theory and experiment, it is found that the quantitative agreement is not very good. The low temperature does not behave according to exponential behavior predicted by the MFA but instead follows the much more rapid decrease predicted by the spin wave

theory $T^{3/2}$. The experimental magnetization near the Curie varies as $(T_C - T)^n$ with n approximatively 1/3, rather than 1/2 as given by the MFA.
Heisenberg Hamiltonian is applied to magnetic materials for which electrons are localized on the atomic sites or there is little hopping character in the valence electrons (i.e. oxides). In presence of a strong electron-electron interaction, as in metals and in alloys, exchange interaction is much more complex than ferromagnetism or antiferromagnetism defined by Heisenberg Hamiltonian. Stoner model overcomes this problem giving a good description of magnetism in 3d-metals (Fe, Co and Ni) in which particles which move freely in the periodic potential of the solid as a more or less free electron gas. Exchange in metals is usually introduced into band-structure calculations by means of an exchange/correlation factor. Since for these crystal electrons the total angular momentum is no longer a good quantum number (the orbital moment is quenched by the crystal field), their properties are governed by their momentum described by the wave vector k and the spin. The overlapping of the electron states leads to the formation of bands with a corresponding density of states rather than discrete levels. Consequently one finds that the magnetic moments of the transition metal are rational numbers rather than integers (as they are for the rare earths, where the f-electrons are localized). These rational numbers cannot be explained from a successive orbital occupation as described by Hunds rules. In the Stoner model the *3d* band can splits into two sub-bands, one with spin up and the other with spin down. The band splitting originates from Pauli exclusion principle, in particular, a couple of electrons with opposite spin has a higher probability of occupying the same spatial region, therefore experiencing a higher repulsion with respect to electrons with the same spin. The interaction energy between spin placed in different spin sub-bands is defined as:

$$E_{int} = U\, n_{\uparrow} n_{\downarrow} \tag{1.5}$$

where $n_{\uparrow}$ and $n_{\downarrow}$ are the number of electrons per atom with up and down spin, respectively. U is the energy cost for putting a second electron of opposite spin on a localized orbital. The existence of a magnetic moment is associated with the appearance of magnetic ordering, while in the localized description the magnetic moment also exists above the ordering temperature (T_c). In a non magnetic state, moving one spin from one sub-band to the other sub-band costs an energy equal to:

$$\Delta E_{int} = U[\frac{n}{2} + n(\varepsilon_F)d\varepsilon][\frac{n}{2} - n(\varepsilon_F)d\varepsilon] - U\frac{n^2}{4} = -U\, n(\varepsilon_F)^2 d\varepsilon^2 \tag{1.6}$$

Here, $n(\varepsilon_F)d\varepsilon$ is the number of electron with energy below Fermi level. This decrease in magnetic energy must be followed by an increase in kinetic energy (E_K), due to the occupation of higher-energy states, that state can be written as:

$$\Delta E_K = n(\varepsilon_F)(d\varepsilon)^2 \tag{1.7}$$

and the total-energy variation is

$$\Delta E_{tot} = \Delta E_K + \Delta E_{int} = n(\varepsilon_F)d\varepsilon^2 - U\, n(\varepsilon_F)^2(d\varepsilon)^2 = n(\varepsilon_F)[1 - U\, n(\varepsilon_F)](d\varepsilon)^2 \tag{1.8}$$

Spontaneous spin splitting entails spontaneous magnetization and then ferromagnetism, when $\Delta E_{tot} < 0$ which is strictly condition fulfilled if $1 - Un(\varepsilon_F) < 0$ (Stoner criteria) like in case of Fe,Co and Ni elements [10]. The criterion implies $n_\uparrow - n_\downarrow > 0$ thus splitting of spin sub-bands occurs without an external magnetic field.
Stoner model is based on simple parabolic density of state (D_{ε_F}), but density of states curves are much more complex as show in figure 1.1.
A more realistic approach to evaluate the magnetic moment values for *3d* metals is

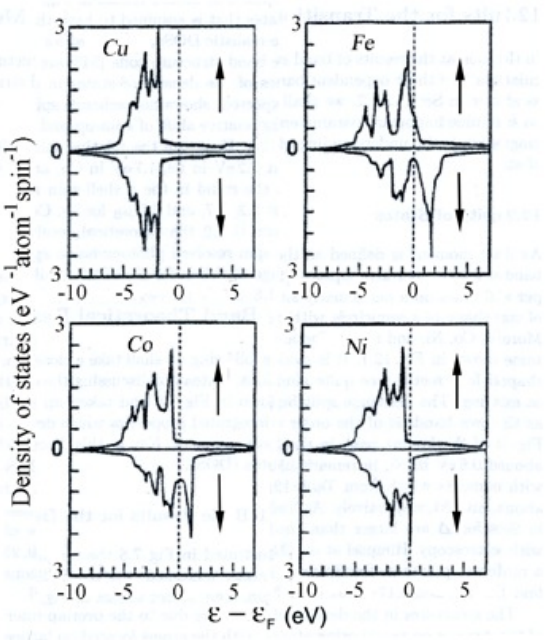

Figure 1.1: - Calculated state density of the *3d*-metals Cu,Fe,Co,Ni.

within the rigid-band model which assumes a rigid shape for d bands as the atomic number increases from Mn to Ni. The higher density of state in *3d* band than *4s*

band facilitates the transition of electrons between d sub-bands, the only one that contribute to ferromagnetism. The moment can be calculated as the difference between the occupation numbers of the spin-up and spin-down sub-bands, with

$$\mu_m \approx (n_{d\uparrow} - n_{d\downarrow})\mu_B \tag{1.9}$$

the Fermi shifted through to the rigid band structure as show in figure 1.2. When the Fermi level lies above the top of the spin-up band, such as in Ni e Co, we have strong ferromagnetism. Spin sub-bands with empty states give rise to *weak ferromagnet*.
This simple model is not completely reliable. In fact, it predicts, for example, that Mn

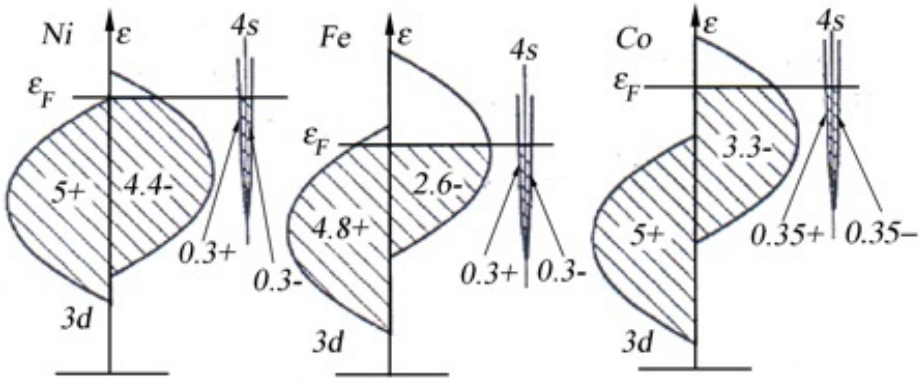

Figure 1.2: - Simple rigid 3d and 4s band pictures for nickel (left), iron (center) and cobalt (right).

should have a magnetic moment higher than the Fe moment, against the experimental evidence. As already mentioned above the rigid band model is a rather naive view due to the assumption that the magnetization vector M(r) changes its direction inside the material. When there is a misalignment of neighboring magnetic moments, there is also an extra cost in exchange energy. Rigid band is a isotropic model.

- The electrons must be in partially filled bands so that there are levels available to be occupied by electrons with unpaired spin.
- The density of levels in the band must be high, so that the increase in energy caused by the alignment of the spins is small.
- The atoms must be at the right distance to allow the exchange forces to align the spins of the electrons of an atom with those of an near atom.

Landau and Lifshitz, in 1935, proposed a micro magnetic model in which an energy term is introduced in the free energy to take into account symmetry [11]. This term, in the isotropic case (i.e. cubic cell) is consisted of an expansion in even power series of the gradients of magnetization components. If the expansion is stopped to the first term, the resulting exchange-energy density assumes the form:

$$e_{ex} = A[(\bigtriangledown m_x)^2 + (\bigtriangledown m_y)^2 + (\bigtriangledown m_z)^2] \tag{1.10}$$

where the constant A, having dimension of [J/m], has to be somehow determined. The value of A can be estimated from experiments, but it is also possible to estimate it with a theoretical approach by the Heisenberg Hamiltonian. Typical values of A are in the order of 10^{-6} erg/cm (10^{-11} J/m) which can be particularized for different lattice geometries (body-centered, face-centered cubic crystals).

Superexchange.

The electrons interactions in magnetic oxides can be described by the same phenomenological background explained above. Equation 1.2 is used to describe parallel ($J > 0$) or antiparallel ($J < 0$) alignment of neighboring localized magnetic moment. The strength of the exchange interaction depends on the orbital overlap. When the atomic electron orbit are too distant there is not enough wavefunction overlap, it is not possible to speak of direct exchange. In this case, common to most of ionic magnetic compounds, there must be some form of mediated electrons interaction from another non magnetic atom (e.g. O_2, F, Cl, Te) that couples nearest neighbors. The third atom lies midway on the line between next nearest neighbors. First Néel and more in details Anderson describe this effect called *superexchange*.

1.1.2 Magnetic Anisotropy

Up to now only isotropic systems have been taken into account, i.e. all physical properties are identical for different directions. The Heisenberg Hamiltonian is completely isotropic and its energy levels do not depend on the direction in space which the crystal is magnetized in. If there is no other energy term the magnetization remanence would always vanish in zero applied field. However, real magnetic materials are not isotropic. Experimentally it is found that the magnetization tends to lie along particular crystallographic axes in the magnetic solid. The orientation of these axes (easy direction)

is a position of stable equilibrium for the magnetization. It costs energy to rotate it into any different directions (hard direction). The magnetic anisotropy is defined as the energy that it takes to rotate the magnetization direction from the favorable into unfavorable direction. Magnetic anisotropy takes origin from the crystalline electric field (CEF) of the solid or crystal, the shape of the magnetic body, or from mechanical stress. It is worth to note that without the existence of magnetic anisotropy, very thin films could not order magnetically. That because the exchange interaction is a short range interaction and the magnetization can be rotated within a distance, called the magnetic coherence length, into a new direction at a very low expense of energy. When a external magnetic field is applied on a ferromagnetic material, can be shown that the free energy density (defined as $F = U - TS$ where U is the internal energy, T the temperature and S the entropy) increases of a quantity δE_m. Keeping constant the temperature, the free energy density variation (dF) is given by:

$$dF = -PdV + HdM \tag{1.11}$$

This means that the change in free energy density can be attributed to a mechanical work (magnetostriction), i.e. -PdV term, by the body and a magnetic work ,i.e. HdM term, on the body by the applied field. Assuming dV=0, the eqn. 1.11 is:

$$\delta F_M = \int dF = \int_0^{M_s} HdM \tag{1.12}$$

The integral solution is graphically represented by the area between the magnetization curve and the y-axis up to the saturation magnetization M_s in a M-H plot, which is minimum when the field is applied along easy magnetization axis and maximum when it is applied along hard magnetization axis (an example is given in figure 1.3). When the saturation field is reached, equation 1.12 is divided in two term for a single crystal of unit volume magnetized along a non- easy $< uvw >$ direction, such as:

$$\delta E_m = (\delta F)^{M_s}_{<uvw>} - (\delta F)^{M_s}_{<easy>} = \int_0^{M_s} (HdM)_{<uvw>} - \int_0^{M_s} (HdM)_{easy} \tag{1.13}$$

This underline the fact that δE_m represents an extra work needed to rotate M in the directions different from the easy one.

Magnetocrystalline anisotropy-

The most important type of anisotropy is the magnetocrystalline anisotropy which is

caused by the spin-orbit interaction (LS) of the electrons. MCA is due to the attractive-repulsive interactions exerted on electrons of the magnetic shell of an atom by the electric field created by all nearby ions (the crystal field). This coupling leads to a preferential orientation (corresponding to a minimum energy) of the electronic distribution and the associated orbital moments when neither the electronic orbitals of the magnetic shell considered, nor the crystal field have spherical symmetry. In addition, the spin moment is induced to follow the orbital moment by the spin-orbit coupling. Therefore, the global magnetic moment of the atom orients along a particular crystallographic direction. A quantitative discussion of the MCA should take into account all the energy terms involved, notably exchange (which determines the spin moment), spin-orbit coupling and coupling between the magnetic shell and the crystal field. The relative importance of these contributions is different for transition metals and rare earth metals. In transitions metals (Fe, Co, Ni) the 3d shell is strongly coupled to the local crystal field because it is an external shell. This coupling is the dominant energy term. The electronic distribution adopts a configuration which minimizes its interaction with the crystal field, and the values of the orbital and spin moments are strongly modified. In particular, the orbital moment vanishes or it is weak for cubic symmetry. The energy terms to be considered are, in order of decreasing intensity, crystal field, exchange coupling between spins and spin-orbit coupling (λ_{LS}). The intensity of this last term is of the order of 10^{-2}eV/atom. The spin moment S can freely orient along any crystallographic direction without notably affecting the energy of the system. Therefore the magnetic anisotropy is weak (of the order of 10^{-6}eV/atom or 10^{5}erg/cm^{3}) which is the case for metallic iron and nickel. The orbital moment is non-zero when the symmetry of the crystal field is uniaxial, and it is maximum along a particular crystallographic direction. Due to the spin-orbit coupling λ_{LS}, the spin moment follows the orbital moment, and this particular direction becomes the easy magnetization direction. The anisotropy energy thus obtained in hexagonal cobalt has a value of the order of 10^{-5}eV/atom (10^{4}erg/cm^{3}) . In rare earth metals the deep 4f electron distribution is much less influenced by the crystal field as it is shielded by more external electronic shells. Thus, spin-orbit coupling is the dominant term in the rare earths. For such systems, the energy terms to be considered are, in order of decreasing intensity, spin-orbit coupling (λ_{LS}), exchange coupling between spins and crystal field interaction. The electronic distribution of the 4f shell is entirely determined by the

exchange and spin-orbit coupling with S_z and L_z taking their maximum values. The orbital moment strongly interacts with the lattice (CEF) and orients itself with respect to the crystallographic directions in order to minimize the energy of interaction with the crystal field, and this defines the easy magnetization direction since the spin magnetic moment is constrained by the spin-orbit interaction to follow the orbital moment. The magnetic anisotropy represents the change in the coupling energy between the 4f electronic distribution and the crystal field depending on whether the orientation of the orbital is along an easy direction or a hard direction. In a uniaxial system, the crystal field is strongly aspheric, and the anisotropy can be very high 10^{-3}eV/atom (10^8 erg/cm^3). The magnetocrystalline energy is usually small compared to the exchange energy with the direction of the magnetization determined only by the anisotropy because the exchange interaction aligns the magnetic moments parallel, no matter in which direction. Due to the complexity of a quantum mechanical approach to the MCA a phenomenological one is generally used to describe the magnetic anisotropy. The magnetocrystalline energy density E_{anis} may be formally expressed as a power series expansion where the α are direction cosines and the β are tensors whose formulation is dictated entirely by the symmetry property of the crystallographic class to which the crystal belongs. It is possible, in principle, to expand E indefinitely in ascending powers of the α but the higher terms $O(\alpha^5)$ and higher are, as found experimentally, be neglected. The assumption that there is no preferred direction in time, which is valid as magnetocrystalline anisotropy is a static property, leads to $\mathrm{E}(\alpha) = \mathrm{E}(-\alpha)$, i.e., an even function of the direction cosines. Then we have for the energy density E_{crys} the following relation:

$$E_{ani} = E_0 + \sum_{ij} \beta ij \alpha_i \alpha_j + \sum_{ijkl} \beta_{ijkl} \alpha_i \alpha_j \alpha_k \alpha_l + O(\alpha^5) \tag{1.14}$$

For uniaxial system anisotropy energy density is given by:

$$E_{ani}^{uniaxis} = K_0 + K_1 sin^2\theta + K_2 sin^4\theta \tag{1.15}$$

For cubic and tetragonal crystals the symmetry relations leads, respectively, to the following expressions for the energy density:

- ***Cubic:***

$$E_{ani}^{cubic} = K_0 + K_1(\alpha_1^2\alpha_2^2 + \alpha_2^2\alpha_3^2 + \alpha_1^2\alpha_3^2) + K_2(\alpha_1^2\alpha_2^2\alpha_3^2) \tag{1.16}$$

where coefficients K_i (magneto crystalline anisotropy constants) which are functions of the coefficients β.

- ***Tetragonal:***

$$E_{ani}^{tetra} = K_0 + K_1\alpha_3^2 + K_2\alpha_3^4 + K_3(\alpha_1^4 + \alpha_2^4) + ... \tag{1.17}$$

Replacing the direction cosine α_i by the angles θ and ϕ, where θ is the angle between magnetization vector and z-axis and ϕ is the angle between x-axis and the magnetization projection on xy-plane, we get:

$$E_{ani}^{tetra} = K_0 + K_1 sin^2\theta + K_2 sin^4\theta + K_3 sin^4\theta cos^4\phi \tag{1.18}$$

The last term reflects the fourfold symmetry of this crystallographic system.

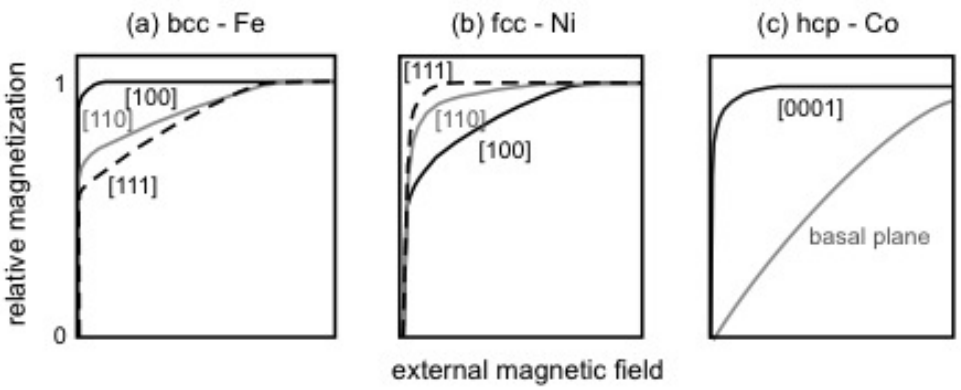

Figure 1.3: - Magnetization curves of (a) bcc-Fe, (b) fcc-Ni, and (c) hcp-Co. The easy magnetization axes are [100]- for Fe, [111]- for Ni, and [0001]-directions for Co. After *Introduction to solid state physics*-8th ed., C. Kittel

A comparison of the curves for single crystals of Ni-MH, Fe, Co (Fig. 1.3) reveals immediately the physical meaning of the magnetocrystalline anisotropy. The curves are graphs of MH up to saturation with the applied field in the easy, intermediate and hard directions respectively.

Magnetic anisotropy can be represented by a an effective magnetic eld H_{ani}, called the anisotropy eld, and is defined as the field acting in the extremal direction, which would lead to a torque on the magnetization equal to that determined by "forces" of

anisotropy (H_{ani}) can be derived for the simplest, but most common case of uniaxial anisotropy (see figure 1.4). Take into account the equation 1.15 and the torque force:

$$\vec{\tau} = \vec{M_s} \times \vec{H_{ani}} = M_s H_{ani} sin\theta = \frac{dE_{ani}}{d\theta} \tag{1.19}$$

when easy axis is along z-axis and $\theta = 0°$, the energy density minimum is obtained when :

$$\frac{d^2 E_{ani}}{d\theta^2} = 2K_1 \rightarrow H_{ani} = \frac{2K_1}{M_S} \tag{1.20}$$

In general, the anisotropy constant K in is the sum over contributions of different order, but the most important is the first corresponding to K_1 for uniaxial anisotropy system. Whereas, for easy-plane anisotropy system also the second order constant K_2 have to be taken into account since $H_{ani} = \frac{2(K_1+2K_2)}{M_s}$.

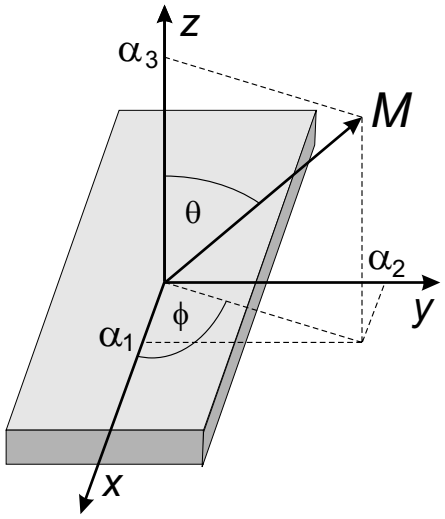

Figure 1.4: - The angle (θ) is the direction of the saturation magnetization M_S with respect to a unique axis of the sample.

Shape Anisotropy-

A magnetized body having a finite dimension is characterized by the presence of free poles at its surface that, besides producing a magnetic field in the space, give rise to a magnetic field inside the sample ($\Delta B = 0$, $\vec{\nabla} \cdot \vec{B} = 0$). Such a field is called demagnetizing field H_d and its direction is opposed to that of the magnetization M and of the external magnetic field. H_d is proportional to the magnetization of the body and sensitive to

the shape, its value is given by:

$$H_d = -N \cdot \vec{M} \tag{1.21}$$

where N (demagnetizing factor) is a second order tensor which is a function of both the sample shape and the considered direction. Only homogeneous body, delimited by second order surfaces (spheres and rotation ellipsoids) magnetize uniformly. In these cases, assuming the principal axes of the body as reference axes, a diagonal tensor is obtained for N

$$\mathcal{N} = \begin{pmatrix} \alpha_a & 0 & 0 \\ 0 & \alpha_b & 0 \\ 0 & 0 & \alpha_c \end{pmatrix} \tag{1.22}$$

In a rotation ellipsoid the energy density due to the demagnetizing field (self energy of M) is

$$E_m = -(\overrightarrow{H_d} \cdot \overrightarrow{M})/2 = M_s^2 sin^2\theta(N_x - N_z) + N_z M_s^2 \tag{1.23}$$

The coefficient of the part of the energy which depend on θ describes the shape anisotropy. In analogy with the expression for the magnetocrystalline anisotropy $E_{anis} = K_1 sin^2\theta$, we can define

$$K_{shape} = \frac{1}{2} M_s^2 (N_x - N_z) \tag{1.24}$$

It is evident that in a spherical sample ($N_x = N_y = N_z = 4\pi/3$) there is no shape anisotropy, but the value of H_d is not negligible. For a prolate spheroid, where $N_z < N_x = N_y$ a positive value for K_{shape} is found, corresponding to an axial contribution to the anisotropy. On the other end in an oblate spheroid, being $N_z = N_x > N_y$, a negative K_{shape} is found which correspond to a planar anisotropy, that is the energy of the system is in a minimum when M_s lays in the xy plane. For an infinitely or very thin film the demagnetizing tensor is

$$\mathcal{N} = \begin{pmatrix} 0 & 0 & 0 \\ 0 & 0 & 0 \\ 0 & 0 & 1 \end{pmatrix} \tag{1.25}$$

and the demagnetizing energy is

$$E_{demag} = \frac{1}{2} M_s^2 sin^2\theta \tag{1.26}$$

For thin magnetic films and multilayers, the demagnetizing energy reaches its minimum value at θ= 90°. This means that the shape anisotropy favors a magnetization direction parallel to the surface. It is worth noticing that in the expression for the energy due

to the demagnetizing field there is a term which does not depend on the direction of M_s. Such a term represents the magnetostatic energy associated with a magnetizated body which can be minimized by reducing N_z and/or M_s that is increasing the sample length ($N_z \rightarrow 0$for infinite length) or by performing the macroscopic demagnetization of the sample (M_s=0) obtained through the distribution of the magnetic moments into magnetic domains. Shape anisotropy constant for Fe is K_{shape}=1.41×10^{-4} eV/atom (≈10^7 erg/cm^3)

Surface and Interface Anisotropies-

The first order term of the anisotropy energy density in a thin film is given by $E_{ani} = (K_u + K_{shape})sin^2\theta$. The competition between K_u and K_{shape} is important in thin films and mulitlayers and can change with temperature. If $(K_u + K_{shape}) > 0$, the thin film prefers to be magnetized perpendicular to its plane, for $(K_u + K_{shape}) < 0$, the easy direction will be in plane. Moreover, in low-dimensional systems have to be taken into account the anisotropy which is related to interfaces. Due to the broken symmetry at interfaces the anisotropy energy contains terms, with lower order, which are neglected for three-dimensional systems. Regarding the effective anisotropy constant K_{eff} is written as:

$$K_{eff} = 2K_{shape}/d + K_u \tag{1.27}$$

where K_u is the volume dependent anisotropy constant and K_{shape} the surface dependent anisotropy constant. The factor of two is due to the presence of two surfaces and the second term exhibits an inverse dependence on the thickness d of the system, important for thin films. It is possible to obtain K_u as the slope of the line and $2K_{shape}$ as the zero-crossing, as in case of Co film (Fig. 1.5). This leads to a critical thickness $d_c = -\frac{2K_{shape}}{K_u}$ and then with $d_{film} < d_c$ perpendicular magnetization, when $d_{film} > d_c$ parallel magnetization. The relative amount of the surface contribution increases with decreasing thickness followed by a spin reorientation transition towards the surface normal below critical thickness. For a FePt film with K_u=1.7×10^7erg/cm^3 and M_s=800 emu/cm^3 the critical thickness at which magnetization vector is easy plane is roughly 350μm, thus magnetization in thin film stays along c-axis perpendicular to the film plane.

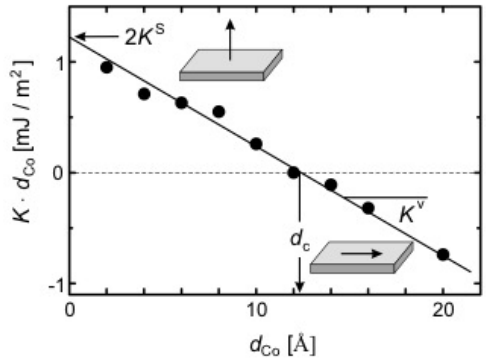

Figure 1.5: - $d \cdot K_{eff}$ of a Co thin film layer as a function of the Co thickness d_Co

1.2 Magnetic Domains

Ferromagnetic material, when homogeneously magnetized, generate a magnetic stray field whose field line spread outside the sample. The stray field of a flat sample magnetized perpendicular to the surface can be viewed as arising from magnetic poles according to $\mu_0 \bigtriangledown \cdot H = - \bigtriangledown \cdot M$. But the generation of a magnetic field costs energy according to

$$E_d = \frac{\mu_0}{2} \int_{space} H^2 dV = -\frac{1}{2} \int_V \vec{M} \cdot \vec{H} dV \tag{1.28}$$

To reduce this energy, ferromagnet breaks up into magnetic domains, each of them with the saturation magnetization M_S. The magnetization directions of the single domains, each along the easy axis, are not necessarily parallel. In fact, magnetization lies in multiple directions in order to minimize the stray magnetic field, making closed packet distribution of field lines. An elementary distribution of domains is shown in figure 1.6. The transitions regions from one direction of the spontaneous magnetization into another are called *domain walls*, and their formation costs energy as well. When the wall energy is larger than the stray field energy, ferromagnet has to be single domain, and such particles do not exhibit a magnetic microstructure at all. Two common types of domain walls are (Fig. 1.7): the Bloch wall, in which a continuous π-degree transition of the magnetization occurs with the moments in the wall oriented parallel to the plane of the wall, and the Néel wall, characterized by moments aligned perpendicular to the plane of the wall. Bloch walls are more common in bulk-like thick films, while Néel walls occur in thin films. In a 3D magnetic crystal we find magnetic domains and Bloch walls that exhibits no stray fields.

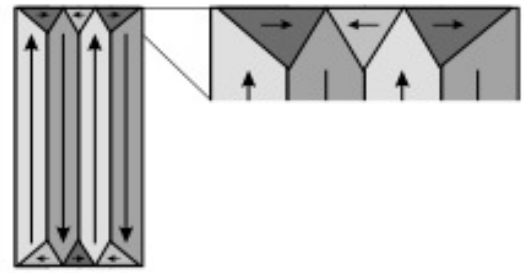

Figure 1.6: - Closure domains which exhibit a magnetization that is not parallel to an easy magnetization axis in order to reduce stray field energy.

The essential idea of the Bloch wall is that the entire change in spin direction between

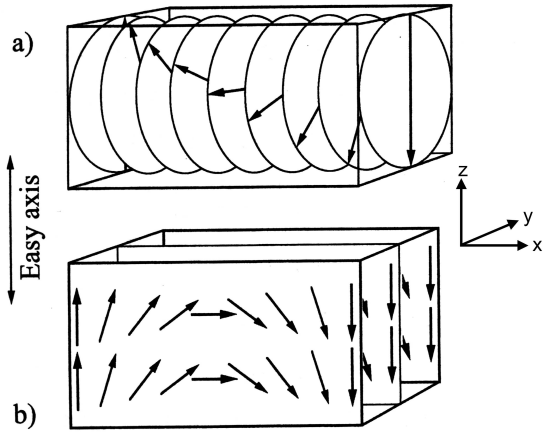

Figure 1.7: - Illustration of two types of π domain walls. In the Bloch wall a), common in thick films, the magnetization rotates in the wall plane. In the Néel wall b), common in thin films, the magnetization rotates in a plane perpendicular to the wall.

domains magnetized in different directions does not occur in one discontinuous jump across a single atomic plane. Rather, the change in direction will take place in a gradual way over many atomic planes. A wall separates two domains of opposite magnetization, thus the magnetization will cover an angle $0 < \theta < \pi$ with the easy direction over a distance d. The competition between the exchange and anisotropy energies will determine the wall thickness and the wall energy.

For a two parallel spins the exchange energy is given by 1.2, but when they exhibit an angle of $\theta \neq 0$ with respect to each other, the energy amounts to:

$$E_{ex} = -2JS_1 \cdot S_2 = -2JS^2 cos(\theta) \tag{1.29}$$

that for small angle can be approximated to:

$$E_{ex} = -2JS^2 + JS^2\theta^2 \tag{1.30}$$

In a Bloch wall a complete π spins rotation occurs in N steps, that means rotation angle is $\theta = \frac{\pi}{N}$. Thus, the total energy of every spin rotation is given by:

$$E_{ex}^{BW} = NJS^2\theta^2 = \pi 2J\frac{S^2}{N} = JS^2\frac{\pi^2}{Na^2} \tag{1.31}$$

where a is a single step length. Now introducing crystalline anisotropy over a N-plane $E_{cry}^{BW} = aNK_u$, the total energy of the Bloch wall is given by:

$$E_{tot}^{BW} = JS^2\frac{\pi^2}{Na^2} + aNK_u \tag{1.32}$$

Thus the domain wall width δ is defined as:

$$\delta = Na = \pi\sqrt{\frac{A}{K_u}} \text{ and } E_{wall} = 2\pi\sqrt{A\,K_u}, \tag{1.33}$$

where $A = \frac{JS}{a^2}$ represents a measure of the stiffness of the magnetization against rotation as consequences of the exchange forces which favor a parallel alignment. The exchange stiffness A decreases with temperature and its value can be estimated from $A(T) \approx \frac{k_B T}{a}$. In making the compromise between all the energies it is necessary to pay attention to the fact that the creation of domain walls does not lead to an increase in the local dipolar energy. This means that no "magnetic poles" must appear on the surface of the walls or inside it, (i. e. $\mathrm{div}M_S = 0$ or $\vec{M}(1)\cdot\hat{n} = \vec{M}(2)\cdot\hat{n}$, where n is a unit vector normal to the flat wall and M(1) and M(2) are the spontaneous magnetization of adjacent domains). This is equivalent to saying that the normal component of the magnetization does not change for the entire thickness of the wall i.e. along the z axis perpendicular to the plane of the domain wall.

Néel walls:

When the condition div M_s=0 is violated, for example in ferromagnetic films, instead of a Bloch wall, we have a Néel wall in which the vector M_s rotates in a plane perpendicular to the domain-wall plane rather than in a parallel plane. The Néel wall is the dominating wall type in very thin films. The magnetization in thin films lies in the plane of the film, because a huge demagnetizing field would act normal to the plane of the film if M_s were turned in that direction. When the film thickness (t) is small compared to

the magnetic domain wall thickness (d) ($t \ll d$), a Néel wall would achieve the smallest magnetostatic energy with the magnetization rotated by 180° in the surface plane. For $\frac{t}{\delta} \leq 1$, the wall thickness and energy density are:

$$\delta \approx \pi \sqrt{\frac{2A}{K_u}} \text{ and } E_{Neel} \approx \pi t\, M_s^2 \tag{1.34}$$

If a Bloch or Néel wall is formed in the film depends on the value of the magnetostatics energy that in the case of a Bloch wall is $E_{ms}^2 \approx 2\pi d M_S^2$. There is a critical film thickness (t_c) below which there is a transition from Bloch to Néel configuration, that can be roughly evaluated [10] by:

$$t_c = 1.8 \sqrt{\frac{A}{M_s}} \tag{1.35}$$

The energy of the Bloch wall increases with decreasing film thickness due to the in-

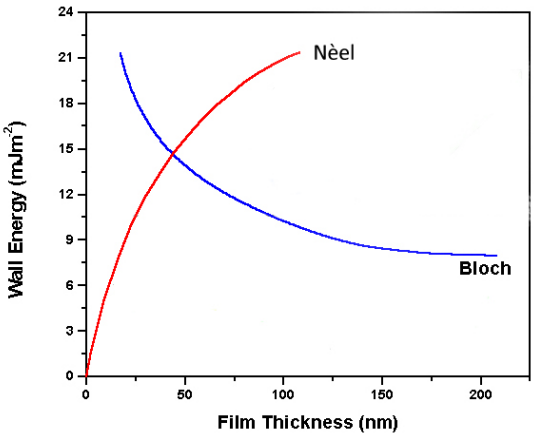

Figure 1.8: - Comparison of domain wall energies for a Bloch and Néel wall for a permalloy film as function of film thickness.

creased magnetostatics energy due to "surface charges" above and below the wall. The energy of the Néel wall decreases with decreasing film thickness because it is proportional to the "surface charge" within the film. It is observed that the Néel walls are stable in many magnetic films for thicknesses up to 50-60 nm. For Fe thin film this critical thickness is 43 nm.

Domain walls in films with perpendicular anisotropy:

When a magnetic film have a uniaxial magnetic anisotropy, with easy axis perpendicular to the film plane, the wall structure is completely different from Bloch or Néel cases.

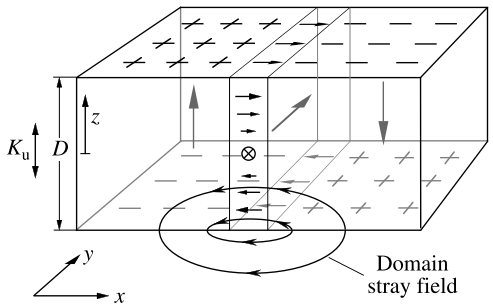

Figure 1.9: - Schematics of the stray field and the wall structure in a perpendicular-anisotropy film. After *Magnetic Domains*, Hubert A. and Schafer R., Springer (2000).

For example, in thin films with a low uniaxial magnetic anisotropy magnetic domains have the form of closely packed stripes, called *stripe domains*.

This difference is mainly due to the coupling between the perpendicular anisotropy, exchange energy and the dipolar interaction within the domain wall. The problem of magnetic domains shape was reduced from a nonlocal and two-dimensional problem to local and one-dimensional problem by Slonczewski [12], for thin film with a quality factor Q=$K_u/K_{shape} > 1$. The basic features of domain walls in systems with perpendicular anisotropy are like regular Bloch walls in the centre of the film. Towards the surfaces the stray field from the neighboring domains acts on the wall twisting the magnetization, which does a spiral rotation along the sample thickness by π angle (Fig. 1.9). It is calculated that the domains wall energy in magnetic material with uniaxial anisotropy is defined as $l\sqrt{K_u A}$, where A is the exchange stiffness and l=4, and the domains evolution has been described by model. In the case of high uniaxial perpendicular anisotropy such as in FePt, the application of this model is not strictly appropriate since it was developed to describe more regular stripe-shaped domains, whereas FePt thin films show perpendicular intergrain domains with an irregular pattern. Casoli et al. [13] has studied this problem and they found a much lower energy wall than $4\sqrt{(K_u A)}$ with a multiplicative factor between l=1-1.5. Moreover, the values of the dipolar length (D_0) has found to be between 8 and 20 nm, which, in the frame of the Kooy-Enz theory, was interpreted as the smallest domain size supported by thin film, which is close to the values of 22.5 nm found by Okamoto et al. [14].

1.3 Magnetization processes

The magnetization curve (MC) is the response of a magnetic material to the application of a magnetic eld. The MC depend on the magnetic history of the sample. The variation of M with the field depends on the material, but the curves have the appearance shown in figure 1.10. Starting from the thermally achieved demagnetized state, the magnetization increases until the magnetic saturation (M_S) is reached at the saturation field (Hs), the field at which the domain structure is totally removed and the magnetization lies in the direction parallel to the applied field. The mechanism of wall displacement and magnetization rotation are involved in this process of magnetization. When the magnetic field is reversed continuously, the magnetization M is also reversed reaching the magnetic remanence (M_r) which is the magnetization that remains if the applied eld is reduced to zero. The question is: what is the mechanism of magnetization reversal? Starting from saturated ferromagnetic system, the applied

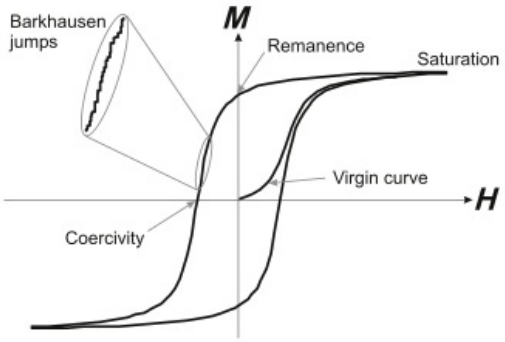

Figure 1.10: - Hysteresis loop schematically. The discontinuous changes near the coercive field (Barkhausen jumps, see also [15]) are not observed with all magnetic samples.

magnetic field is reduced to zero and then increased in the opposite direction. At some state during this process, the magnetic configuration of the starting saturated state becomes unstable and magnetic domains start to grow. The field at which this happens is called nucleation field (H_N). When the applied field is lower then nucleation field, magnetic domains with lower potential energy (defined as $HM_scos\theta$, where θ is the angle between the applied field and the magnetization direction) grow at the expense of neighboring domains with higher potential energy by displacement of the domains wall. With increasing field, magnetic domains disappear gradually until the material is completely saturated in the opposite direction. The origination of magnetic domains

and walls are problems related to the micromagnetism. The nucleation process is studied given by the linearization of the Brown equation [16]. The nucleation field follows from the smallest energy eigenvalue of a system of linear, partial differential equations and the mode of nucleation is the associated eigenvector. The two common modes are the coherent rotation and curling. In the first, magnetization turns homogeneously in the space i. e. all spins stay parallel to each others during rotation. This process increases the magnetocrystalline energy and the magnetostatic energy while the exchange energy remains constant. This modes are described by the Stoner-Wohlfarth model, which will be described later. The second mode is an incoherent mode, called curling mode, where the exchange energy and the magnetocrystalline energy are both increased. while the magnetostatic energy remains constant.The magnetization reversal mechanism is strongly influenced by the film thickness or particle radius. There is a critical radius (R_C) at which reversal mechanism pass from coherent dominated reversal mode to curling. In the case of sphere material, i.e. nanoparticles, this radius is given by

$$R_c = 1.44\frac{\sqrt{A}}{M_s} \tag{1.36}$$

If there is no other way, the reversal of magnetization in a sphere should be started by coherent rotation if $R < R_C$ and by curling if $R > R_C$. In case of nanowires material transaction occurs when the thickness to width ratio exceeds 0.5 [17]. In a real magnetic system, crystal defects results in a domain wall potential. In particular imperfection, e.g., crystallographic defects or inclusions, act as point of pinning or trapping for domain wall. Then the coercivity depends on pinning site and it is related to how the domain wall is driven into it by the magnetizing field in the forward direction. Pinning sites must correspond to potential energy walls between single domain and multidomains status, and they are characterized by an arrangement of closure domains near an imperfection. A ferromagnetic material can have a number of pinning sites, each characterized by the field H_n necessary to nucleate or unpin a domain wall, and that the particular site that operates depends on the value of the previously applied field. If the domain walls are present and free to move, the hysteresis loop will have a low coercivity. If the interior defect concentration is so low that there is negligible resistance to wall motion, then the loop will have a negligible width and an starting slope of $1/N_d$, where N_d is the demagnetizing factor. That important role of defects

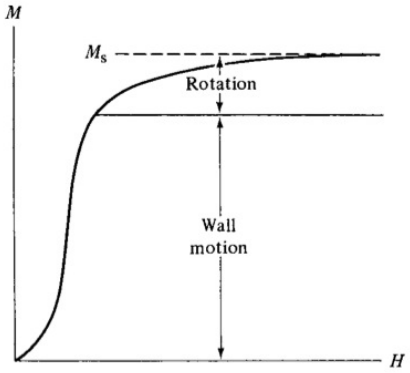

Figure 1.11: - Magnetization processes of a virgin ferromagnetic material

is due to the different anisotropy constant in the environment of defect. It is worth to note that as big as defects then easier come out magnetic domains with different magnetization direction.

1.3.1 Stoner-Wohlfarth Model

Stoner-Wohlfarth's model is shown to be a particular solution of the micromagnetic equation, as such it describes a minimum of energy. In real physical system, it will be used only in those cases in which the nucleation field is the lowest negative as compared to the nucleation field of the other possible modes of magnetization reversal. Now we will discuss briefly the coherent rotation process of single domain particle. This problem was examined in detail in a classic paper [18], where it is assumed a ellipsoidal particle with uniform magnetization. The main assumption of Stoner and Wohlfarth is that the material is made up of rather small particles, which are sufficiently separated from each other so that interactions between them are negligible. If the magnetic field, H_{appl}, is applied at an angle γ respects the easy uniaxial anisotropy of the particle the magnetization vector will rotate to an angle θ from the easy direction, which means that the magnetization will be at an angle $(\gamma - \theta)$ with the magnetic field direction (Fig. 1.12). The energy of this system is given by:

$$E = Ksin^2(\theta) - \vec{H} \cdot \vec{M} = Ksin^2(\theta) - HM_scos(\gamma - \theta) \tag{1.37}$$

where K is the sum of magnetocrystalline and shape anisotropy constant. Thus, the energy becomes minimum at a specific angle θ which can be determined by setting the first derivative to zero:

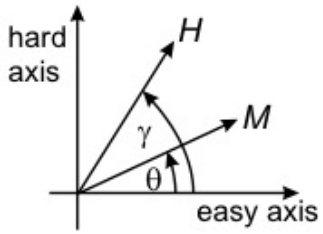

Figure 1.12: - Magnetization M of a single domain particle with a uniaxial anisotropy along x-axis in an external magnetic field H

$$\frac{dE}{d\theta} = 2Ksin\theta cos\theta - \mu_0 HM_s sin(\gamma - \theta) = 0 \tag{1.38}$$

$$sin\theta cos\theta - hsin(\gamma - \theta) = 0 \tag{1.39}$$

$$m = cos(\gamma - \theta) \tag{1.40}$$

where $h = \frac{H_{appl}M_s}{2K}$ and $m = \frac{M}{M_s}$ If $\gamma = \pi/2$, the applied field is normal to the easy axis, thus from 1.39 and 1.40 we have

$$sin\theta cos\theta = hcos\theta \tag{1.41}$$

with $sin\theta = h$ and $m = sin\theta$, 1.41 is written as

$$m = h = \frac{H_{appl}M_s}{2K} \rightarrow M = \frac{H_{appl}M_s^2}{2K} \tag{1.42}$$

This shows that the magnetization is a linear function of H_{appl}, with no hysteresis and the saturation is reached when $H_{appl} = H_A = \frac{2K}{M_s}$. Suppose now that the field is applied along the easy direction $\gamma = 0$ and and that both H_{appl} and M_S are directed along the positive direction of this axis. Then H_{appl} is reduced to zero and $\gamma = \pi$. The field does not exert any torque on M_s, the magnetization becomes unstable at $\theta = 0$ and will rotate by π when the field reaches a sufficiently high value in the negative direction (critical value called the switching eld, H_s). We note that a solution

$$sin\theta cos\theta - hsin(\gamma - \theta) = 0 \tag{1.43}$$

does not necessarily correspond to a minimum of energy (stable equilibrium). A solution may also correspond to a maximum energy (unstable equilibrium). We must determine the sign of the second derivative in the zeros of the first derivative.

$$d^2E/d\theta^2 = cos^2(\theta) - sin^2(\theta) + hcos(\gamma - \theta) = 0 \tag{1.44}$$

It is found that the configuration with the magnetization antiparallel to the field is a metastable state of minimum energy. The magnetization can align with the applied field and reversed only when the applied field reaches the critical value $H_S = 2K_u/M_s = H_{appl}$, above which the configuration at $\theta = 0$ is no longer defined as a minimum of the energy. In general case when $\gamma = \pi/2$, the solution of the equation 1.41 and 1.44 lead to the equation in which the critical field H_C and the critical angle θ_C at which the magnetization flips are defined using $h = H_s/H_{ani}$ (see equation 1.42 with $\gamma = 0$). H_s, called *switching field*, is the field where the magnetization switches abruptly and irreversibly, it is not greater than the anisotropy field ($H_s \ll H_a$) and occurs at the field for which 1.38 is satisfied and also $d^2E/d\theta^2 > 0$, then the system is in a energy minimum:

$$d^2E/d\theta^2 = cos^2(\theta) - sin^2(\theta) + hcos(\gamma - \theta) = 0 \tag{1.45}$$

Simultaneous solution of equations 1.38 and 1.45 leads to the solution of the critical field h_c and the critical angle θ_c at which the magnetization will flip. This field lower than the anisotropy field. figure 1.13 shows hysteresis loops calculated for various values of γ. In general, these loops consist of reversible and irreversible portions. The portion

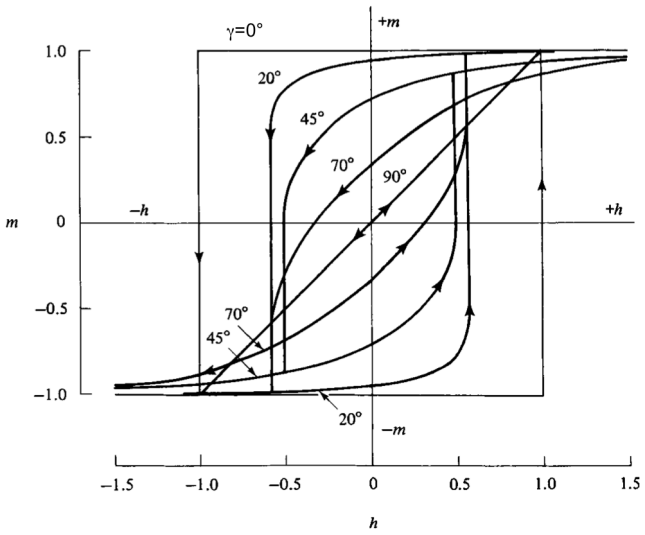

Figure 1.13: - Hysteresis loops for single domain particles with uniaxial anisotropy; γ is the angle between the field and the easy axis.

of the total change in m due to irreversible jumps varies from a maximum at a $\gamma = 0°$ to zero at a $\gamma = 90°$. The critical value of reduced field h_c, at which the M_s vector

flips from one orientation to another, decreases from 1 at a $\gamma = 0°$ to a minimum of 0.5 at a $\gamma = 45°$ and then increases to 1 again as a approaches $\gamma = 90°$. These solutions represent the lowest energy point at fixed angle γ at which the system is stable. This dependence of the energy E on the angle θ between the easy magnetization axis and the direction of the magnetization is represent in the figure below 1.14.

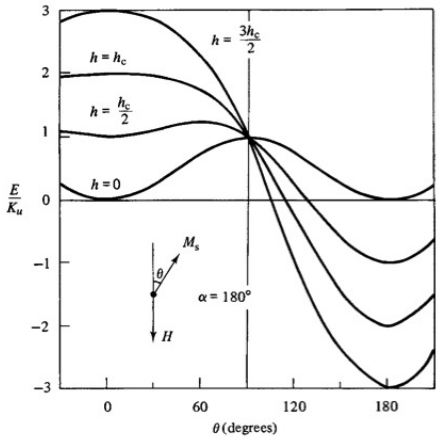

Figure 1.14: - Rotation of magnetization by a field applied to a single-domain ellipsoid.

We have considered so far a particle isolated. Experimentally we study sets of nonin-

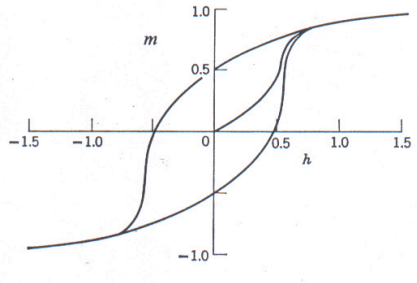

Figure 1.15: - Rotation of magnetization by a field applied to group of single-domain particles.

teracting particles (e.g. ellipsoids prolate) whose polar axes are distributed randomly (Stoner-Wohlfarth model). Since the coercive force of the individual particles varies from 0 to 1 would be a reasonable assumption to suppose that the average coercive force of the whole system can be $H_C = 0.5$ and M_R=0.5. In this hypothesis the magnetic field of each single particle is negligible, thus the hysteresis loop is similar to that

of bulk material (Fig. 1.15).

1.4 Magnetism in Thin Films and Multilayers

The magnetism at low dimensions is affected by physics phenomena that in a bulk or an extended system can be negligible. Besides the change in magnetic domains pattern, the film thickness reduction affects the magnetic behavior of the whole material. The presence of broken symmetry point, such as interfaces, represents a *hot point* where deviations from homogeneity occur. At the interface, i.e. between substrate and thin film, the magnetic moments are reduced due to hybridization between the electronic states of the atoms in the ferromagnetic thin film and at the interface of the substrate. The surface exhibits an increased magnetization because of the reduced coordination number, i.e. a more atomic-like behavior is present [19]-[20]. An important parameter represents the thickness of a thin film. The behavior of the anisotropy for different film thicknesses was already taken into account in equation 1.27. The anisotropy constant changes, opening up the possibility of a spin reorientation transition from in-plane to a perpendicular magnetization by change film thickness (d). In thin film, also the Curie temperature is often decreased compared to the bulk following a power law proportional to the number of atomic layers, as shown for Ni(111) layers in [21]. This reduction is due to the absence of magnetic neighboring atoms.
Another important aspect, in particular in heterogeneous multilayers, is the decreasing intensity of electrons moving through a ferromagnetic thin film barrier. This function is independent of the material and represents therefore a universal curve. Considering the inelastic mean free path λ, I is given by [22]:

$$I(d) = I_0 e^{-d\backslash\lambda} \tag{1.46}$$

Moreover, the intensity depends on the magnetization of the magnetic thin film which is due to a spin dependence of the inelastic mean free path characterized by $+\lambda$ and $-\lambda$ for spin up and spin down electrons, respectively. Magnetic film acts as a spin filter due to the spin band dependence of the conductivity.
The influence on the magnetic properties of the interface morphology is illustrated figure 1.16. A real interface is not smooth. Its roughness leads to the formation of

terraces with opposite spin direction thus preventing a ferromagnetic coupling over the whole area. In order to reduce the number of uncompensated spins (here from six to two) frustration (marked by circles) or domain walls (white box) occur. An important

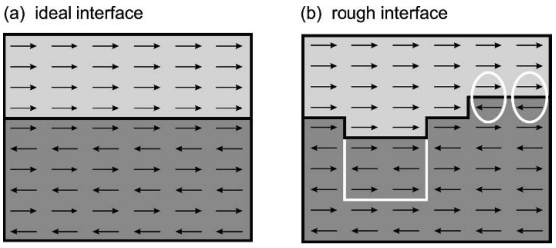

Figure 1.16: - (a) Ideal smooth interface. Assuming a ferromagnetic coupling across the interface between antiferromagnetic results in six uncompensated spins. (b) real rough interfaces exhibit steps which separate different terraces. After [22]

feature of magnetic multilayers is given by the coupling over the interface, the so-called interlayer exchange coupling (IEC).The most important effects of the interlayer roughness on the interlayer exchange coupling are the reduction of the amplitude, so-called orange peel effect, and frustration effects.

Recently results on interlayer exchange coupling show that different coupling regimes can be obtained by changing the interface morphology in Fe/FePt exchange-coupled bilayers [23]. For homogeneous and pseudo-continuous FePt layers covered by epitaxial Fe layer, a strong coupling between Fe and FePt that results in Rigid Magnet behavior has been obtained. In the case of an island-like morphology, where Fe shows a more disordered structure and a considerable fraction of Fe grows on directly MgO, the exchange interaction between the two phases is decreased and an Exchange-Spring regime is obtained.

IEC is also tuned using a non-magnetic spacer layer between two magnetic layers. This result is great used in some spintronic devices, as will be explained later. The presence of a non magnetic material can be described by a change of the RKKY exchange interaction. Assuming z as interlayer thickness the exchange coupling constant is:

$$J_{RKKY}(z) \propto \frac{1}{z^2} \tag{1.47}$$

RKKY interaction is pronounced in thin film and acts over long distances. Positive or negative value of J_{RKKY} results in ferromagnetic or antiferromagnetic behavior, respectively. The thickness of the spacer layer determines the type of coupling. In

presence of a roughness spacer, the coupling strength is reduced because roughness suppress the coupling among the neighbor magnetic moments. An additional difference is given by anisotropy effects which is realized in the presence of different values of the anisotropy constant in the layers. In that case the shape of hysteresis loop changes as the value and sing of the anisotropy constant.

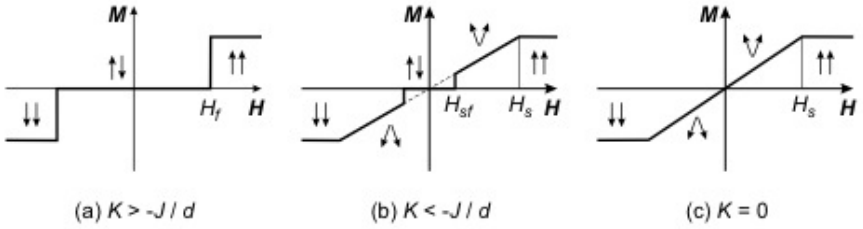

Figure 1.17: - Theoretical magnetization curves for two identical antiferromagnetically coupled ferromagnetic layers with a uniaxial magnetic anisotropy which is (a) larger than the coupling strength and (b) smaller than the coupling strength and the situation of zero anisotropy (c). The arrows schematically indicate the orientation of the magnetization directions relative to the vertical easy axis which the field is applied along. After [24]

The curves in figure 1.17 are necessarily modified in real system when magnetization rotation does not occurs by coherent rotation, but by domain nucleation or domain wall propagation. In that case a hysteric behavior is present. Finally, at the interface the magnetization is pinned in a direction different from the easy direction inside the film. The *exchange length* (l_{ex}) is related to the energy stiffness (A). In the specific case of spin orientation at the interface with a perpendicular component, considering the anisotropy of the material as $K_u + 2\pi M_\perp^2$, l_{ex} is given by:

$$l_{ex}^{\perp} = \sqrt{\frac{A}{K_u + 2\pi M_\perp^2}} \tag{1.48}$$

One important consequence of these results is that the exchange interaction changes the magnetization direction in one region over a distances of l_{ex} to another region.

1.5 Ions implantation

The physical and mechanical properties of any material are usually changed when it is bombarded with neutrons, ions, electrons or gamma rays. These property changes are

due to the atomic rearrangements, called radiation damage, brought about by the radiation, and the kind of rearrangement depends on the kind of radiation, i.e., neutrons, being uncharged particles, are highly penetrating.
When incident on a solid, a particle can travel relatively large distances, in the solid, before a collisions with atoms. Each collision, however, causes displacement of one or more atoms into interstitial positions, leaving vacancies behind. Interstitials and vacancies are collectively called point defects to distinguish them from a line imperfection like a dislocation. Similarly, ion implantation and focused ion-beam processing, which are widely used in the semiconductor industry, are steadily gaining ground in magnetic thin film materials processing. A useful aspect of irradiation is that can make some materials magnetically softer [25] or harder [26].

1.5.1 Physics of ion irradiation

Radiation damage arises from the interactions of energetic particles with a target material as they are slowed down and transfer their energy by a series of collisions. At the beginning, the ion kinetic energy is reduced mainly by the electronic stopping processes, and ion trajectory is relatively unchanged. When the ion has slowed down sufficiently, the collisions with nuclei (the nuclear stopping) become more probable and finally dominant. When atoms of the solid receive significant energies by the ion, they will be removed from their lattice positions, and produce a cascade of further collisions in the material. This series of nuclear collisions results in atomic displacements and generates defects that alter microstructure and mechanical properties.
Nuclear stopping results from the elastic collisions between the ion and atoms in the sample and increases when the mass of the ion increases, dominating the stopping process at low energy. The stopping power is a function of the repulsive potential V(r) between two atoms. For very light ions slowing down in heavy materials, the nuclear stopping is weaker than the electronic stopping at all energies. Electronic stopping refers to a process by which the ion is slowed and its energy is transferred to the target material through inelastic collisions between bound electrons in the medium and the ion moving through it. The collisions may result both in excitations of bound electrons of the medium and in excitations of the electron cloud of the ion. In most materials, these electronic excitations have little effect on damage production, and energy dissipation effects are neglected in most cases, such as in ion implantation of metallic systems.

However, electronic stopping may play an important role in the displacement process. Electronic stopping increases linearly with the square root of the ion energy, while at lower ion energies ($<10^{-1}$ MeV) the nuclear stopping becomes more relevant. In particular, the nuclear collisions create a sequence of atomic displacements (cascades) that produce a localized high concentration of defects. The atomic displacement sequence creates a primary knock-on atom (PKA), which is the atom struck by a bombarding irradiation particle. One part of the losses energy is given to the neighboring atoms, producing secondary displacement events. Then the distance between successive collisions becomes progressively shorter. When the energies decrease below a few hundred eV, the mean free path between collisions is of the order of a couple of atomic distances. Thus, a large amount of energy is deposited in a small volume, generating a high concentration of defects in a localized region.
An important parameter, useful for theoretical and experimental model, is the *displacement energy*. This is the energy needed to overcome the lattice force inside the material and to move the atoms one atomic spacing away from its original site. If the atom comes back into its original site, the energy will be given up into phonons. For metal *displacement energy* is 25 eV and for semiconductor is 15 eV [27].
Since implantation doses are common higher than 10^{12} $ions/cm^2$, ion trajectories can be predicted employing statistical means (i.e., Monte Carlo simulation). The average depth of the implanted ions is called the projected range R_p, and the distribution of the implanted ions respect to the depth can be approximated as Gaussian with a standard deviation σ_p. The ion concentration at depth x, can be written as:

$$n(x) = n_0 exp\{-\frac{(x - R_p)^2}{2\sigma_p^2}\} \tag{1.49}$$

where $n_0 \approx \frac{0.4\phi}{\sigma_p}$ is the peak concentration (ϕ is the implantation dose), R_p is the projected range, and σ_p is the standard deviation.

The ion and dislodged target atoms can cause further damage spreading their energy over many moving particles during loss energy process. Hence, after many ions have been implanted, the crystalline target will have changed toward a highly disordered state. If the target temperature is sufficiently high, the competing process of self-annealing can occur to repair some or all of the damage as it is generated. There is an

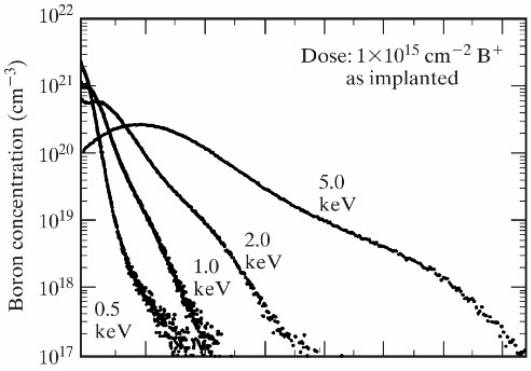

Figure 1.18: - Profile of Boron ions implantation in Si. Shallow implantation are present below surface.

implantation critical dose, defined as a minimum necessary to amorphize the target, at which surface target is eroded or damaged. Damage can affect the results of subsequent processing steps. For example, point defects are known to influence diffusion in silicon. Damaged oxide layer etch faster than continuous oxide one because some of the bonds are already broken. Considering the sputtering yield (Y), it is possible to understand if these phenomenas are negligible or not. The thickness decreasing due to damage is given by:

$$\Delta t = \frac{Y\phi A}{N_a \rho} \tag{1.50}$$

where A is molecular weight, N_a is Avogrado's number and ρ is the density, ϕ implantation dose.

1.5.2 Effect on magnetic material

The consequences of ion irradiation on magnetic material have been found mainly on magnetic properties. The displace of atoms generated by ion collisions involves two different aspects: the purely collisional atom mixing on one hand, and the chemical heat of mixing on the other. At low mixing rate, the mixing rate is linear (for He irradiation) or almost quadratic (for Ga irradiation) with the dose. The modification of the profile concentration at the interfaces due to collision may be characterized by an interdiffusion length $l_{dif.}$ [27]. At high ions dose, $l_{dif.}$ reaches several monolayers so that the alloying of atoms is strong.

$$l_{diff.}^2 = (N_{dis}\phi/N_s)a^2 \tag{1.51}$$

where N_{dis} is the average number of displacement generated by each ion, N_s is the atomic surface density of the material, ϕ is the ion dose and a lattice parameter. For example, Ga ion implantation, by focused ion beam, leads to the reduction of exchange coupling between magnetic grains and the formation of extended domain wall pinning defects in Co film. These effects lead to a square hysteresis loops and a dramatic increase in coercivity (as shown in [28]). On the other hand, a Ga^+ dose of 10^{14} ions / cm^2 induces a complete transition from the ordered $L1_0$ to the disordered A1 phase in FePt thin film, leading to a drastic decrease of the magnetic anisotropy and coercivity, and to a spin reorientation transition from out-of-plane to in-plane [25].
Ion irradiation is revealed to be a very flexible tool to tailor the main magnetic properties (e.g., anisotropy, coercive field, exchange interaction, Curie temperature) of thin films and multilayers, giving rise to several effects, depending on the chosen parameters, like intermixing, modification of morphology, interface quality and strain, modification of crystallinity and chemical composition, production of vacancies and pinning centers [29, 30, 31, 32].

1.6 The exchange-spring system

In 1991 E. Kneller and R. Hawig [33] proposed a new type of permanent magnets, called exchange-spring magnet, in which the spaces between the high-coercivity particles (hard grains) in a granular permanent magnet could be filled with a high-magnetization and low-coercivity material such as iron or a cobalt-iron alloy (soft grains). The hard-magnetic grains provide the high anisotropy and coercive fields while the soft-magnetic grains enhance the magnetic moment with the additional benefit of reducing the rare-earth content since the soft phase can be rare-earth free. The soft grains are pinned to the hard-magnet grains at the interfaces by the exchange interaction while the center of the soft-magnet grains can rotate in a reversed magnetic field. Such magnets are characterized by enhanced remanent magnetization and reversible demagnetization curves (hence the name exchange-spring). The first attempts to prepare exchange-spring magnets started from $Nd_2Fe_{14}B$ compound prepared by melt-spinning and mechanical alloying. The goal was to achieve the mutual dispersion of the hard and soft phases, while maintaining a crystallographic coherence among them, but different problems

were highlighted, regarding both the crystallographic alignment and the control of sufficiently small soft regions, to avoid the easy nucleation of reversed domains.
A similar material has been also suitably structured at the nanometer scale, such as coupled bilayer films, providing convenient model systems for studying the magnetic properties of the exchange system because the relative length scales (i.e., thicknesses of the hard- and soft-magnet layers) can be controlled during the deposition process. The hard/soft multilayer becames a model system to study and understand the properties of exchange-spring systems, but on the other hand also promising candidate for the design of thin-film permanent magnets. Nowadays, it could found possible applications as micro-electro-mechanical devices (MEMS) where thin-film permanent magnets can be employed in high-quality and performance integrated micro-actuators, micro-motors or micro-pumps and in recent years they are proposed as perpendicular recording media [34].
Many theoretical approaches have been considered in order to explain the magnetization reversal process in exchange coupled bilayers. In particular, they can be classified as:

- Model base on micromagnetic calculations with continuum as well as discrete approach leading to analytic expressions of the relevant parameters [35, 36, 37, 38, 39, 40]
- Computational approaches by solving the dynamic equation of motion [41]
- First principle calculation of the band-energy structure [42]

These models assume the in-plane orientation of the magnetization and a common result was the definition of the soft phase thickness (d_s) as an important parameter in determining the magnetization reversal process and thus the shape of the hysteresis loop, besides the exchange length of the hard phase ($l_{w,h} = \sqrt{A_h/K_h}$). Asti et al. [38] developed a model based on a multilayer composed of hard and soft layers of finite thickness. By studying the sign of χ_c, calculated at the critical field corresponding to the start of flux reversal, as a function of the half-thickness of the hard (t_h) and soft (t_s) layers, a magnetic phase diagram for the planar hard/soft multilayer was obtained (Fig. 1.19 (b)).
Increasing the thickness of the hard or soft layers three regimes have been obtained:

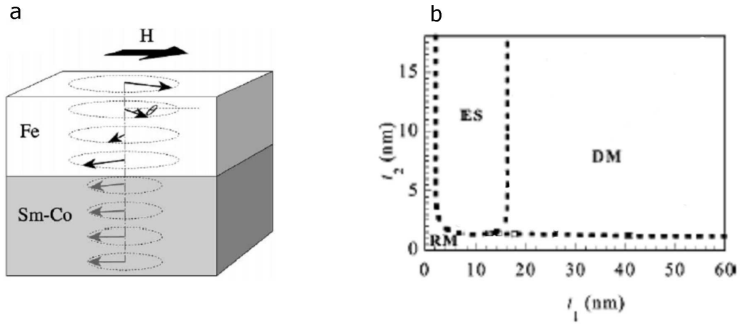

Figure 1.19: - a) reversible rotation of the magnetic moments in the soft layer. b) Magnetic phase diagram for a Fe/NdFeB bilayer, in terms of soft (t1) and hard (t2) layer thicknesses

the rigid composite magnet (RM), the exchange-spring magnet (ES) and the decoupled magnet (DM). Each with similar characteristics compared to the results of the previous model. The position of critical curves between the regimes is determined by intrinsic (K, M_S and A) and extrinsic parameters of the multilayer (t_h, t_s). In the rigid magnet regime the highest maximum energy product is achieved, with values of 75 MGOe for Fe(8 nm)/SmCo(3 nm) and 100 MGOe for Fe(4.4 nm)/NdFeB(1.8 nm) bilayers, due to a square hysteresis loop with a unique value of the critical field. The existence of the exchange-spring regime also depends on the ratio between the anisotropy constants of the two phases: for soft/SmCo the ES region disappears when $K_s/K_h \leq 0.06$. Thus to have a ES regime, the anisotropy of the soft phase has to be less than few percent of the hard phase anisotropy. A further increase in K_s/K_h leads to the disappearance of the decoupled regime. The two phases begin too similar to give an independent contribution and only the RM regime remains.

The results of this model have been compared with previous theoretical approaches and experimental works founding a good agreement.

Finally, Asti et al. suggest a possible extension of their model to a system with perpendicular orientation of the magnetic moments by adding to the total magnetic free energy a shape-anisotropy term of the form $-2\pi M_S^2$, obtaining the magnetic phase diagram in figure 1.20. In this model different assumptions have been made:

- The infinite exchange-spring multilayer is supposed to be made of alternate soft and hard layers perpendicular to the x-axis.

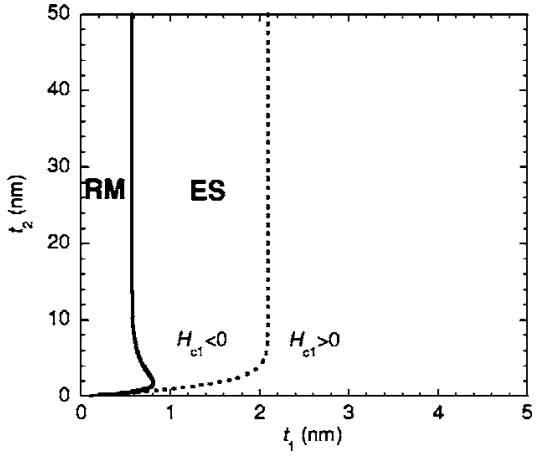

Figure 1.20: - Magnetic phase diagram in the plane of layer thickness t_1 soft and t_2 hard for a Fe/FePt bilayer with perpendicular anisotropy. After [38].

- The two component layers are assumed to have uniaxial anisotropy with symmetry axes both perpendicular to the film plane.
- Only periodical solutions are considered.
- No magnetic domains are present in the film plane.
- The problem has a one-dimensional character.
- A strong interlayer exchange coupling is considered.

An analytical solution for free energy density has been given:

$$G = \sum_{1,2}(-1)^i \int_{x_0}^{x_i} F_i dx F_i = A_i[(\frac{\delta\vartheta}{\delta x})^2 + sin^2\vartheta(\frac{\delta\phi}{\delta x})^2] + \mu_0 M_i H cos\vartheta + L_i sin^2\vartheta \quad (1.52)$$

where ϕ represents the angle between the projection of magnetization in the y-z plane and the z axis, L is the total anisotropy constants and i=1,2.
One open issue for all theoretical model remain to estimate the thermal stability and energy barrier of the exchange system respect with other system. A simple analytical model for the optimization of a single phase data layer is given when assuming that the film is composed of weakly coupled single domain grains [34]. In this case the energy barrier for a single domain particle is given by

$$\Delta E = KV(1 - \frac{H}{H_{SW}})^2 \quad (1.53)$$

where V is the volume of the grain and H is the effective field acting on the grain parallel to the easy axis. K is the effective anisotropy, which is the sum of the uniaxial anisotropy K_1 and the shape anisotropy. The exchange field among the neighboring grains stabilizes the grain, opposing the demagnetizing field. The effective field can be written, in MKS international units system, as:

$$H = \frac{J_s}{\mu_0} - \frac{B_{ex}}{\mu_0} \tag{1.54}$$

Assuming all grains except one to be reversed, the switching field of the last grain, called saturation field or closer field, can be expressed as

$$H_{SW} = \frac{2K}{J_s} - B_{ex}\mu_0 + \frac{J_s}{\mu_0} \tag{1.55}$$

By setting the first derivative of Eq. 1.53 with respect to K at zero, the values for K and J_s that maximize the energy barrier for a given field can be obtained [34].

$$K = \frac{1}{32\mu_0}(3B_h + 3B_{ex} - \gamma)(B_h + B_{ex} + \gamma) \tag{1.56}$$

with $\gamma = \sqrt{5B_h^2 + 6B_hB_{ex} + B_e^2x}$. Considering $J_s = 1/4(3B_h + 3B_{ex} - \gamma)$ the energy barrier can be expressed as

$$\delta E(B_h, B_{ex}) = V\frac{(3B_h + 3B_{ex} - \gamma)(-B_h + B_{ex} + \gamma)^2}{8\mu_0(B_h + B_{ex} + \gamma)} \tag{1.57}$$

figure 1.21 shows the calculated energy barrier as a function of J_s Exchange coupled

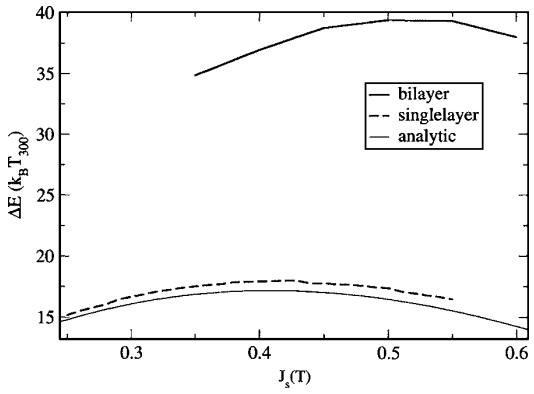

Figure 1.21: - Energy barrier as a function of J_s for the single layer and the bilayer. In the bilayer, the same value of J_s is taken in the hard and soft part.

composite (ECC) media, based on exchange-spring system, has been shown to possess

several major advantages relative to conventional perpendicular media, including a reduction in the switching field of approximately a factor two for the same thermal stability and stronger magnetic anisotropy energy. In particular, there is a ratio between the thermal barrier of the media and its switching field, which can be defined as [43]

$$\xi = \frac{2\Delta E}{H_s M_s V} \tag{1.58}$$

where H_s, M_s, V are the switching field, the saturation magnetization and magnetic volume, respectively. For this ECC media, this ratio ξ approach two, making ECC media quite promising for ultra high-density recording (see paragraph 1.7.1). A related advantage is that ECC media allowing a much higher track density for a given writer than a conventional media [44].

1.6.1 Graded exchange spring system

The idea of exchange spring media with varying anisotropies in each layer was further extended by changing the anisotropy gradually from two to N layers, approaching towards a graded media system. Following the results obtained by Suess [45] in this system, the coercive field of the multilayer structure was found to decrease with 1/N while the energy barrier was only determined by the magnetic properties of the hardest layer (Fig. 1.22). A drastic reduction of $H_{pinning}$, the field at which completely magnetization reverse occurs, can be realized if the anisotropy constant depends quadratically with the thickness (x), such as $K(x) = \alpha x^2 = x^2 K_{hard}/t_G^2$ with t_G is the total thickness of the grain. The media has its maximum anisotropy constant corresponding to the top of the grain (K_{hard}) and the pinning field follows

$$H_{pinning} = (2/J_s)\sqrt{AK_{hard}}/t_G. \tag{1.59}$$

Suess shown that the energy barrier in graded media linearly decreases with the magnetic field [46]. This result demonstrates that the energy barrier of graded media is further enhanced relative to the single phase barrier because of this unexpected linear field dependence, resulting in even higher thermal stability. The field dependence of the energy barrier $E_b(H)$ is determined and found to be linear [47]. A simple explanation is provided for this linear dependence on the basis of the magnetization reversal

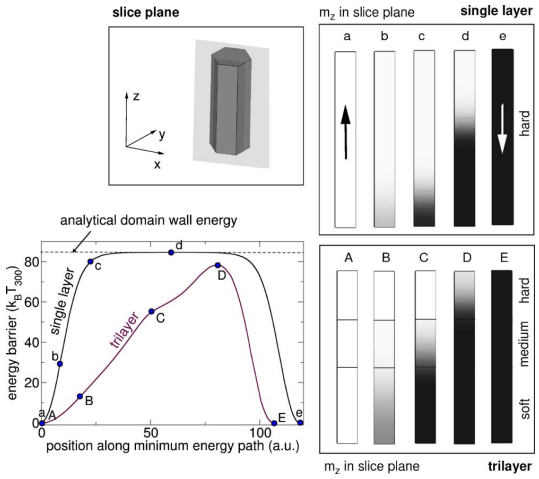

Figure 1.22: - Energy barrier and thermally activated switching process for different exchange systems calculated by Suess [45].

mechanism of graded media, which is not a rigid rotation, but proceeds via domain walls motion. Energy barrier dependance can be calculated as

$$E_b(H) = 4\sqrt{AK} - (2t_G - \sqrt{A/K})JH. \tag{1.60}$$

taking into account two energy terms such as the energy of the domain wall formation and the difference of the Zeeman energies between the up and the down spin regions. In general in graded media, the reversal pathways of magnetization reversal proceeds via a partial domain wall that gradually pass through the whole thickness, instead of an avalanche-like runaway reversal, which is theorize for homogeneous phase media. This makes graded media more suitable for magneto recording application than other multilayer system.

1.7 Magnetic recording

The magnetic materials are well known to be the first framework for information storage and recording. Tape recording equipment rapidly came into use by radio studios and networks in the 1950s. Magnetic recording as a consumer product only became popular with the introduction of the audio tape cassette in 1963. Starting about 1980, the digital audio compact disk, or CD, began to replace the cassette tape as a medium

for prerecorded music, and recordable CDs are now the most marketed media. Magnetic material have been used not only as in media but also in electronic device, i.e., tape reader or hard disk head driver. Furthermore, the increasing miniaturization of computer components means that the magnetic materials in computer and recording devices are commonly made and used in the form of thin films. Moreover, a new challenge was emerged from discoveries, in the 1980s, concerning the spin-dependent electron transport phenomena in solid-state devices. Spin-polarized electron injection from a ferromagnetic metal to a normal metal [48] and the discovery of giant magnetoresistance (GMR) in 1988 [49][50] open the era of spintronics.

1.7.1 Magnetic media

The trend in area density growth of HDDs was subject an big increasing in the late 1990s, reaching 100% per years, due to the introduction of GMR technologies not just for a simple scaling down enhancing.

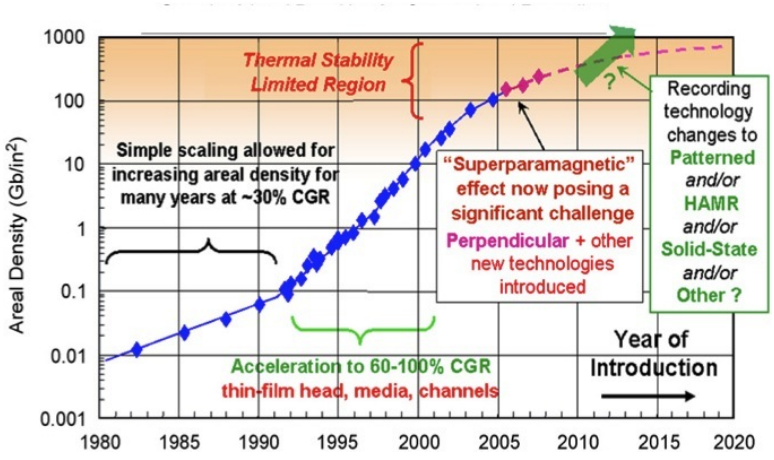

Figure 1.23: - Growth of area density for commercial recording hard drives. After [51].

Moreover, between 2000 and 2003 the areal density increased eight times and the price per bit dropped eight times. Although semiconductor memories (i.e., flash memory, DRAM) have replaced magnetic media in some devices, the latter are the only solution for big storage requirements. Until 2008, technologies approach to the magnetic recording was the longitudinal geometry (LMR). The magnetic layers in the hard disk media, in general, are in the polycrystalline state. Therefore, all medium has random orientations with respect the film plane and the track direction. This causes group of grains to

begin bit of information. One important technological aspect, from which depends the quality of storage information, is the signal-to-noise ratio (SNR). SNR depends on the number of grains in a bit, to increase its value smaller and more homogenous grains are necessary. Thus, underlayer or seedlayer (i.e., Cr) have been used. But this is where lies the problem, in fact, as the areal density increases the grains volume get reduced. In a magnetic material, the energy barrier that allows to overcomes the magnetization inversion is proportional to anisotropy energy K_uV, where K_u is the uniaxial anisotropy constant and V is the volume of the grain. If the volume is reduced, but K_u is kept constant, the thermal energy (k_BT) competes with magnetic anisotropy energy and causes a spontaneous magnetization reversal (i.e. in superparamagnetism). That can be solved by increasing K_u, but that leads to another problem: writability. In fact, there is a writing field limit related to the write-head material, the maximum write head field in the medium has to be approximately twice the coercivity (in LMR mode it is 1.2 T [52]) . Obtain an high SNR, writability and thermal stability constitute what is called the *trilemma* of recording, the improvement of one leads to deterioration of the other.

The perpendicular recording technology (PMR) has been introduced in order to get an higher density area storage in HDDs. The first article on the fundamentals of PMR was published in 1970s by Iwasaki et al. [53], but the first commercial application was introduced more than thirty years after. Nowadays, perpendicular media based on CoCr alloy have been introduced [54] on double layers disks in presence of a soft underlayer (SUL) such as NiFe. The SUL helps in the writing process by concentrating the magnetic flux from the head writing pole to the head of the trailing pole (see figure 1.24).

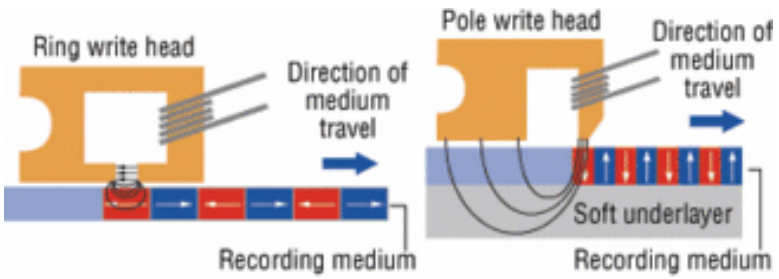

Figure 1.24: - Schematic illustration of longitudinal magnetic recording and perpendicular recording during the writing process.

The recording media is placed in the gap between SUL and recording head whit the aim to gain more magnetic flux than in LMR case. Since 1980s, SUL was found to introduce noise in the PMR process, but only during last years a antiferromagnetic layer (such as IrMn) has been introduced to pin the SUL magnetization. Moreover, the presence on the SUL of a seedlayer favors the epitaxial growth of recording layer (RL). Actually CoCrPt-oxide is the RL material on which recording media are based with an expected density approaches 1 Tbit/in^2. That alloy satisfies an high SNR, thermal stability and writability all at the same time. In order to increase area density the grains size has to be reduced, while a high thermal and high perpendicular uniaxial anisotropy constant K_u are desirable. One type of different material for recording media, with the potential to be used in high density PMR, it is $L1_0$-FePt alloy that is thermally stable even for grain sizes of 3 nm [55] with higher perpendicular uniaxial anisotropy constant, but a higher coercive field.

To overcome the limits of actual magnetic material, Victoria [43] and similarly Suess [56] have proposed exchange-coupled composite (ECC) media for realizing ultrahigh recording densities of several $Tbit/in^2$. In a ECC media, a hard magnetic layer and a soft magnetic layer are coupled by exchange interaction. In an exchange spring media (see paragraph 1.6), the hard magnetic layer provides thermal stability and the soft magnetic layer reduces the switching field to a value that can be easily reach by writing hard disk head. Furthermore, Suess [45] extended this concept from bilayer structures to multilayer structures and demonstrated that coercive field reduction is proportional to 1 over the number of layers and thermal stability of the media remains the same. In an ECC, with individual layer thicknesses larger than the width of a full domain wall, reversal of magnetization takes place in two steps [57]:

- A nucleation process in the soft layer results in the formation of a domain wall which is pinned at the phase boundary between the soft and the hard magnetic layer.
- A depinning process for the displacement of the domain wall into the hard magnetic layer induces full switching of the ECC particle.

Extensive theoretical work has been carried out to investigate the reversal mechanism in ECC films [40, 57, 58, 59], switching characteristics and thermal stability [60]. Experimental works have been realized hard/soft bilayers, e.g., epitaxial SmCo/ (Fe,Co)

with in-plane anisotropy [40], granular $CoCrPt - SiO_2$, granular $L1_0 - CoPt/Co$ [61] and epitaxial $L1_0 - FePt/Fe$ [62] with perpendicular anisotropy. Thus, multilayers ECC media and then graded media have been proposed as a way to increase area density to 2.5 Tb/in^2 [63]. Moreover, an optimized performance is expected for graded media where the pinning and nucleation fields are of comparable magnitude. By using long pillars, the write field can be made arbitrarily small, but there is trade-off between achievable areal density and write field, even in the absence of interactions. The reason is that small write fields must push the domain wall deep into the pillars, where the write field is relatively weak and also quite diffuse, deeply reaching into neighboring pillars and inhibiting single-bit writing [64]. FePt $L1_0$-phase based ECC and graded media have been suggested to achieve the areal density beyond $1 Tb/in^2$ with still high thermal stability [34, 43].

In order to move beyond the PMR, many solutions have been proposed for further increases in areal recording density, but two of the most promising are heat-assisted magnetic recording (HAMR) and the use of bit patterned media (BPM). In bit-patterned media (BPM) recording, well defined bit boundaries, made of non magnetic material, are created by lithography, co-polymers process, guided self-assembly or nanoimprint fabrication process [65]. By these ways each single patterned group of magnetic grains act as a single domain. In conventional magnetic recording media, the exchange interaction coupled among grains can lead to wide magnetic domain boundaries, instead in bit-patterned media this coupling does not affect the bit boundary since it is defined by the lithography process. Patterned media is expected to reach 8 Tb/in^2 [66], but to overcome this threshold the bit size should be smaller than 5 nm. Moreover, the shape of patterned bit is fundamental in the placement of HDD head. For example, rectangular bits with an aspect-ratio of 2 nm or higher are preferred than square bit area.

The signal in a BPM is proportional to the area of the magnetic bit, that is related to the resolution of the pattern technique used. Thus, the smallest feature size of non magnetic region is desirable in order to achieve high areal density. The most promising approach is to use electron beam lithography to make small bit in a master mold and then replicate this pattern on the media substrate using the nanoimprinting fabrication [67]. By this way, these patterning concepts will surpass the costs which is one of the main problems of this technologies. However, nanoimprint replication is a potentially

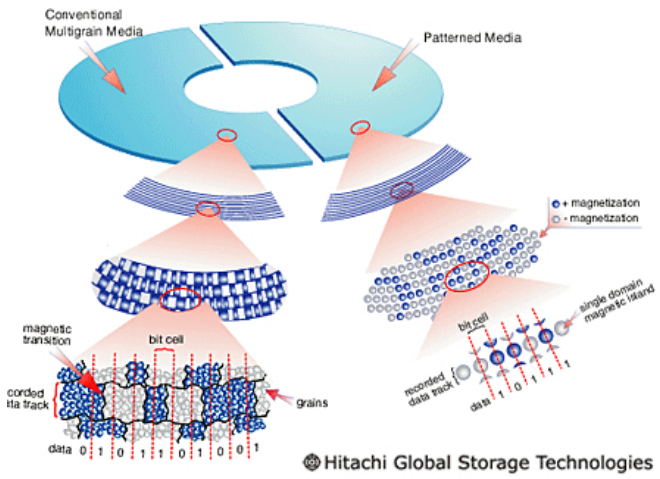

Figure 1.25: - Comparison between conventional magnetic recording and bit patterned recording

low-cost method of stamping a nano scale resist pattern on disks for subsequent etching steps. Di-blocks co-polymer approach combined with nano imprinting help to fabricate 40nm dots [68, 69]. In addition to the cost, the other problems in BPM are the different size in the same array of nanobits which are source of noise and a not perfect planar surface that allowing conventional air-bearing to operate.

The other proposal (HAMR) (schematically depicted in figure 1.26) could be used with the actual granular media, but with much smaller grains and higher anisotropy constant. Thermally-assisted recording uses a laser to heat up the media while the magnetic head is writing the smaller bits of data. This enables the use of media that is magnetically stable at room temperature with the very small magnetic grains required for high-density storage. The energy assist source can come from a tiny spin torque oscillator, as proposed by Li et al. [70], or from a near field optical head [71].

Seagate researcher [72] uses surface plasmons to allow focusing of a light beam below the diffraction limit. Surface plasmons are collective oscillations of electrons that are coupled to light and propagate along an interface between a dielectric and a metal. They are strongly localized to the surface interface and exponentially decay in amplitude away from it. An attraction of surface plasmons is that they can have wavenumbers much larger than those of conventional electromagnetic waves. This means that optical energy can be delivered to a size below the diffraction limit. Surface plasmons can produce field intensities in the near field that are orders of magnitude higher than in

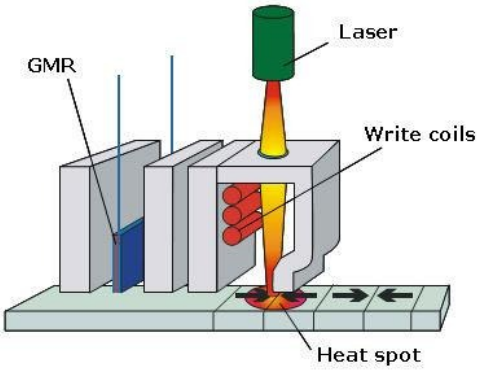

Figure 1.26: - Thermal assisted recording process.

the incident light. To take advantage of this fact for application in devices, precise control of gaps is often required because this higher field decays exponentially with distance from the metal surface. Fortunately, the gap between the transducers and recording medium in hard disk drives is very small and well regulated using advanced air-bearing surface designs, which makes surface plasmon structures offering enhanced and sub-diffraction-limit fields a perfect match for HAMR. Despite the exciting potential of this techniques, many practical issues still need to be explored before it is ready for commercial deployment. The HAMR process requires local temperature rises in the magnetic medium of 300 K or even higher, so thermal dissipation is an important issue that needs to be solved. On the recording head side, a lot of the energy is lost to heating the local structure and could result in head deformation and component failure after repeated heating cycles. Regarding the recording medium, its deformation due to momentary heating cycles and thermal damage or depletion of the disk lubricant could cause serious drive failures.

A new frontier of magnetic recording is the microwave-assisted magnetic reversal (MAMR), that significantly reduces the reversal field when the microwave field frequency matches the media ferromagnetic resonance (FMR) frequency [73]. However, for ultrahigh densities the required reversal fields as well as microwave fields and frequencies can still be too high for media with homogeneous elements. The employ of ECC and much more graded media in MAMR system is shown to allow significantly reduced reversal bias fields, microwave fields, microwave frequencies, and reversal times [74].

In summary, bringing together new recording technology and new recording media will

make possible to push away the superparamagnetic limit and satisfy the trilemma problem obtaining a remarkable increasing of the area density storage in the next generation of HDDs.

1.7.2 Spintronic devices

Since the discovery of the giant magnetoresistence (GMR) in 1988 the spin-based electronics began to offer new opportunities for the next generation of devices that combining standard microelectronics with spin-dependent effects. Devices operations are subjected to a new degree of freedom (i.e., spins alignment) respect to conventional semiconductor charge-based electronics. The advantages are many: nonvolatility, increased data processing speed, decreased electric power consumption and increased integration density compared with conventional semiconductor devices. The research in the last decade has been focused on emerging challenges by a theoretical or experimental approach as optimization of electron spin lifetimes, detection of spin coherence in nanoscale structures, transport of spin polarized carriers, heterointerfaces, manipulation of spin and spin-torque effect.
The GMR is a significant increasing of the ordinary magnetoresistance effect (MR), first discovered by William Thomsom (Lord Kelvin) in 1857, where magnetoresistance ratio is defined as the ratio of the resistivity change to the resistivity in the parallel configuration:

$$MR(\%) = \frac{\sigma_{AP} - \sigma_P}{\sigma_P} \cdot 100 \tag{1.61}$$

The origin of GMR is found in the "two current model" proposed by Mott in 1936 [75]. The MR and similarly GMR are quantum mechanical effects observed in thin film structures in presence of ferromagnetic and nonmagnetic layers. When the magnetic moments of the ferromagnetic layers are parallel, the spin-dependent scattering of the carriers is minimized, and the material has its lowest resistance. When the ferromagnetic layers are antialigned, the spin-dependent scattering of the carriers is maximized, and the material has its highest resistance. The directions of the magnetic moments are changed by external small magnetic field. An interesting example of how scientific discovery can rapidly open a new innovative trade, comes from the GMR as applied to magnetic information storage.The first commercial product using GMR (such as magnetic field sensor) was available in 1994, just eight years after the discovery of GMR, and the first products to have a major economic impact are read-heads for HDDs, which

were announced by IBM in November 1997 (Fig. 1.27).

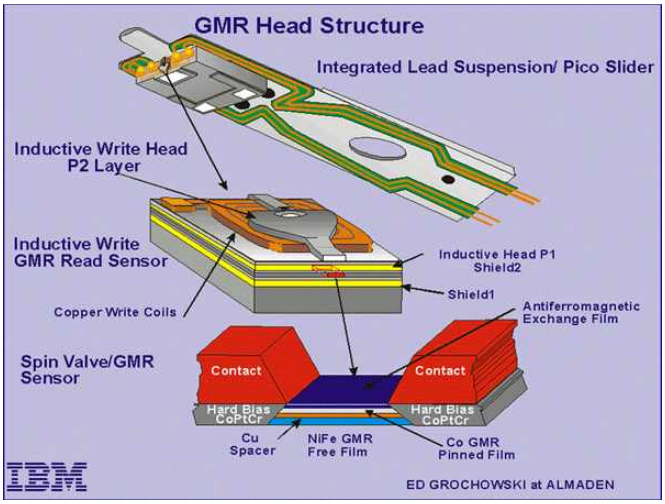

Figure 1.27: - Detailed structure diagram of a GMR head assembly.

The simplest GMR-based devices is the spin valve. A spin valve has two ferromagnetic electrodes (alloy of magnetic element) separated by a thin non magnetic metallic layer (usually copper). One electrode is pinned, i.e., the magnetization is locked along one direction using a ferromagnetic underlayer, the other is called free layer and its magnetization can be changed by application of a magnetic field. In 1995 Moodera et al. [76] bring into the scene the magnetic tunnel junction (MTJ), a device in which a pinned layer and a free layer are separated by a very thin insulating layer. The tunneling magnetoresistance (TMR) is modulated by magnetic field in the same way as spin valve, but the change in magnetoresistance is ten times higher with applied magnetic field less than in spin valve. TMR is defined as:

$$TMR = \frac{R_{AP} - R_P}{R_P} = \frac{2P_1P_2}{1 - P_1P_2} \tag{1.62}$$

where $P_{1(2)}$ is the spin polarization of first (second) electrode. TMR is due to the spin asymmetry of density of state (DOS) in a ferromagnetic conductor, both the conduction and the tunneling probability through a potential barrier are spin-dependent properties, leading to a different resistance of the MTJ for the parallel and antiparallel magnetic configurations of their electrodes.

Spin-polarized transport occurs in any material for which there is an imbalance of the spin populations at the Fermi level. This imbalance commonly occurs in ferromagnetic

metals because the density of states available to spin-up and spin-down electrons is often nearly identical, but the states are shifted in energy with respect to each other (Fig. 1.28). This shift results in an unequal filling of the bands, which is the source of the net magnetic moment for the materials (equation 1.9), but it can also cause the spin-up and spin-down carriers at the Fermi level to be unequal in number, character, and mobility. This produces a net spin polarization, but the nature of the specific spin-polarized carriers and the electronic energy states associated with each material must be identified in each case.

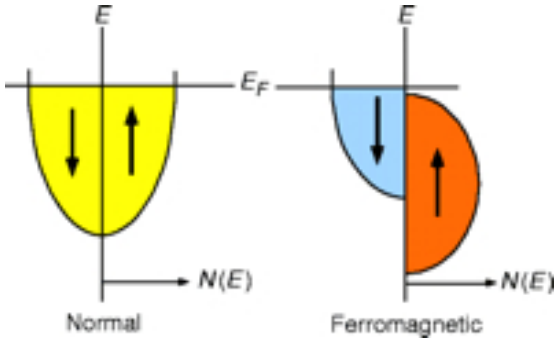

Figure 1.28: - The density of electronic states available in a normal metal and in a ferromagnetic metal

Such material as Fe, Co or Ni, are only partially polarized. They have a spin-polarization (P) varying from 40 to 50%. P is defined in terms of the number of carriers that have spin up ($n_\uparrow$) or spin down ($n_\downarrow$), as:

$$P = \frac{(n_\uparrow - n_\downarrow)}{(n_\uparrow + n_\downarrow)} \tag{1.63}$$

To increase the TMR in solid state devices the simplest way is to introduce electrodes with high spin polarization at the Fermi level. Half-metals are materials with 100% spin polarization (i.e, P=1), where the only states that are available to the carriers are those for which the spins of the carriers are parallel to the spin direction of those states at the Fermi level. Thus, depending on the direction of magnetization of a material relative to the spin polarization of the current, a material can function as either a conductor or an insulator for electrons of a specific spin polarization. An analogy can be made with polarized light passing through an analyzer. The family of half-metallic ferromagnets is constituted by half-Heusler alloys, i.e., NiMnSb and PtMnSb, but these materials are not suitable for spintronics applications because of difficulties in crystal

growth. Useful hal metallic ferromagnet (HFM) materials are oxides such as CrO_2, (double) perovskites and Fe_3O_4. The latter will be described later.
A simple working representation of a spin-polarized device is shown in figure 1.29. The electrons travel from a ferromagnetic metal electrode, through a normal metal, and into a second ferromagnetic metal electrode. When the magnetizations of the two electrodes are in an aligned state, the resistance is low, whereas the resistance is high in the antialigned state.

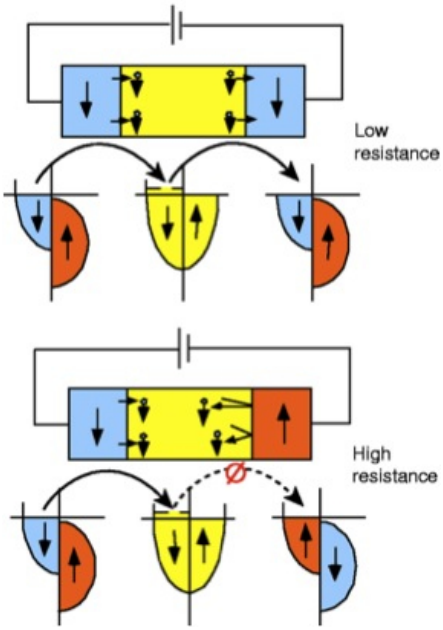

Figure 1.29: - Schematic representations of spin-polarized transport from a ferromagnetic metal, through a normal metal, and into a second ferromagnetic metal.

The development of FM-insulator-FM tunnel junctions with high magnetoresistance has demonstrated that tunnel barriers can result in the conservation of the spin polarization during tunneling, suggesting that tunneling may be a much more effective than diffusive transport as in case of spin valve devices. Theoretical work [77] has quantitatively developed the understanding of the potential effectiveness of tunnel injection. If the impedance of a barrier at an interface is sufficiently high, then the transport across that interface will be determined by the (spin-dependent) density of the electronic states of the two electrodes that are involved in the tunneling process. The current through the barrier is then sufficiently small that the electrodes remain in equilibrium

and the relative (spin-dependent) conductivities of the electrodes play no substantial role in defining or limiting the spin-dependent transport across the interface.
TMR and GMR based devices are dominating application in HDDs in particular for read heads. Other application can be found in non volatility devices such as magnetoresistive random access memories (MRAM). MRAM uses magnetic hysteresis to store data and magnetoresistance to read data. MTJ or pseudospin valve memory cells [78] are integrated in chip and work like a static semiconductor RAM chip with the added feature that the data are retained with power off. Potential advantages of the MRAM compared with silicon electrically erasable programmable read-only memory (EEPROM) and flash memory are 1000 times faster write times, no wearout with write cycling (EEPROM and flash wear out with about 1 million write cycles), and lower energy for writing. MRAM data access times are about 1/10,000 that of hard disk drives. MRAMs are actually commercialized.
Another new phenomena related to a spin-polarized current was reported when a current of polarized electrons enters a ferromagnet and a transfer of angular momentum between the propagating electrons and the magnetization of the film occurs. This concept of spin transfer was proposed independently by Slonczewski [79] and Berger [80] in 1996. They predicted that current flowing perpendicular to the plane in a metallic multilayer can generate a spin transfer torque strong enough to reorient the magnetization in one of the layers. Slonczewski predicted that the spin transfer torque from a direct current could excite two qualitatively different types of magnetic behaviors depending on the device design and the magnitude of an applied magnetic field: either simple switching from one static magnetic orientation to another or a dynamical state in which the magnetization undergoes steady-state precession. Subsequently, spin transfer has been implicated to explain the observation of spin precession for high-energy, spin-polarized electrons that traverse a magnetic thin film [81] and enhanced Gilbert damping in magnetic multilayers compared to one-component magnetic films. The phenomenon did not attract a great deal of attention at the time, largely because very large currents (up to 45 A) were required, given that the samples were quite wide-on the scale of mm. However, with advances in nanofabrication techniques, thin ferromagnetic films can now be made readily and these exhibit domain wall motion at currents of a few mA and below. Research on spin-transfer-induced domain wall motion has been pursued vigorously by many groups since the early days of the 21st century [82].

Nowadays, many work is underway to investigate spin-torque-driven precession in tunnel barriers. One reason for the interest in spin-torque effects in tunnel junctions is that tunnel junctions are better-suited than metallic magnetic multilayers for many types of applications. MTJs have higher resistances that can often be better impedance-matched to silicon-based electronics, and TMR values can now be made larger than the GMR values in metallic devices. Moreover, deposition techniques have now been developed to make both aluminum oxide and MgO tunnel barriers sufficiently thin to support the current densities needed to produce magnetic switching with spin transfer torques. Applications of spin transfer torques are envisioned using both types of magnetic dynamics that spin torques can excite. Magnetic switching driven by the spin transfer effect can be much more efficient than switching driven by current-induced magnetic fields (the mechanism used in the existing magnetic random access memory). This may enable the production of magnetic memory devices with much lower switching currents and hence greater energy efficiency and also greater device density than field-switched devices. The steady-state magnetic precession mode that can be excited by spin transfer is under investigation for a number of high-frequency applications, for example nanometer-scale frequency-tunable microwave sources [83], detectors, mixers, and phase shifters. One potential area of use is for short- range chip-to-chip or even within-chip communications. Spin-torque-driven domain wall motion is also under investigation for memory applications.

Organic spintronics is a promising research field where organic materials are applied to mediate or control the spin-polarized signal in conventional spintronic devices. Organic material open the way to cheap, low-weight, mechanical flexible, chemically interactive electronics. In an organic spintronic device, the non magnetic layer (NM) is an organic material, so it is possible to talk of *hybrid* devices, since inorganic layers are combined with organic one. Organic spintronics not only combines the above mentioned advantages with one of spintronic, but their strong point is the potentially long spin relaxation times (τ_s) [84] due to a combination of low atomic weight, delocalized π bond and hopping mechanism of charges transportation between localized molecular states. A spin relaxation times in the range of 10^{-7} - 10^{-5}s have been found in organic NM barrier [85], instead of metal where the value is $\sim 10^{-10}$s times [86]. In *hybrid* spintronic device, the distance between the two FM electrodes should be smaller than the spin relaxation length to work properly.

An important issue in organic spintronics is contacting the organic material. Organic materials are usually fragile and the standard microfabrication techniques used in conventional inorganic materials often introduce considerable damage, making the contacts poorly defined, considering that the quality of the inorganic/organic interfaces is of crucial importance.

In this context, a natural evolution of organic spintronics is toward molecular electronics using magnetic molecules, as well as molecule-based magnetic materials, as component of new spintronics systems. These materials can be designed with desired electronic properties and the conductivity can be changed by more than fifteen orders of magnitude [87]. Also τ_s can be exceptionally long and moreover ferromagnetic ordering near room temperature in such molecules is shown [88]. By this way spin could be manipulated one by one and new magnetic phenomena may be discovered.

Very recently a new scenario has been opened by the work of Ron Naaman and coworkers who report that a layer of double- stranded DNA deposited on a gold surface acts as a filter for electron spins [89]. Depending on the thickness of the DNA layer, they show that it is possible to achieve up to about 60% spin polarization. Their results indicate that the spin may play an important role in electron-DNA interactions in biological systems and open new possibilities scenario for spintronic devices. Based on this phenomena, for example, it is possible to apply self-assembled monolayers of chiral molecules as very efficient spin filters at room temperature for spintronic applications.

2

Experimental techniques

2.1 Growth Techniques

With the term *physical vapor deposition* (PVD) are denoted those vacuum deposition process, such as evaporation, sputtering and laser ablation, where the coated material is passed into vapor phase by physical mechanism. These methods are the most universal for depositing thin films.

2.1.1 Sputtering

This thesis is devoted to the study of films and heterostructures partially or completely grown by Radio Frequency (RF) Sputtering, thus, this technique represents an essential tool for the work. Sputtering is particularly effective for providing controlled deposition of materials in thin films. In the sputtering growth the material from a source called target, placed into a vacuum chamber, is dislodged and ejected from the surface due to the moment exchange associated with surface bombardment by energetic particles. The bombarding species are generally ions of noble and inert gas such as Argon. The chamber is evacuated to an pressure typically in the range of 10^{-8}mbar and, during deposition, filled with the working gas (i.e., Ar) in the $10^{-2} - 10^{-3}$mbar pressure range. Then an electric discharge is ignited between target, serving as cathode or negative electrode, and substrate, serving as anode. The bombarding particles transfer kinetic energy to the target atoms and provide the subsequent ejection through the target surface of those atoms which acquire sufficient kinetic energy to overcome the local binding forces. The binding energy of a surface atom is typically in the range from 5 to 10eV. The fundamental event in sputtering is the atomic collision between atoms

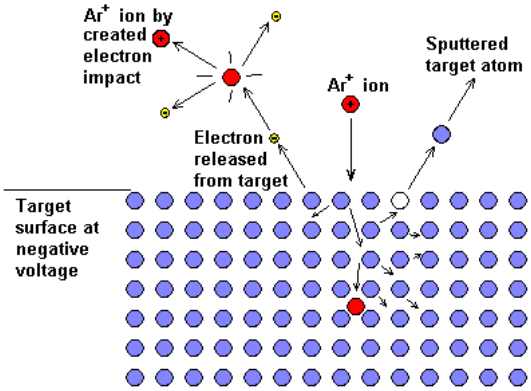

Figure 2.1: - Sputtering process events.

(Fig. 2.1), on which three aspects can be highlighted:

- the target particle is driven deeper into the target by the moment exchange
- the momentum passed to the target particle is greatest when two particles have identical mass
- bombarding particles will be reflected if their mass is less than that of the target particles.

The first observation listed above suggest that a single binary collision will not, in general, produce sputtering. The ejection requires a sequence of collisions, called collision cascade, which is initiated by the incident energy particle. The second observation concerning momentum exchange. The sputtering rate will be highest when there is a good match between the masses of bombarding particles and target atoms. Accordingly, Argon is generally used as a sputtering working gas. The third observation is related to the possible backward reflection in a single collision if the bombarding particle mass is less than of the target atom.
The sputtering species are primarily atoms. However, atomic clusters and molecular fractions have been observed as well as positive and negative ions [90]. One important parameter considered in sputtering process is the *sputtering yield*. This is defined as the average number of target atoms ejected per incident particle, in multi-element targets the *partial sputtering yield* is defined. The yield depends on the target species, its surface condition and temperature [90], as well as on the energy, angle and type of

bombarding species.
Direct current (DC) sputtering is rarely used today, instead radio frequency techniques are usually employed, such as: RF sputtering and magnetron sputtering. In the RF technique the problem of charge accumulation on target surface [91] is overcome by using a radio frequency of 13.56 MHz, allowing to sputter nonconducting targets. Consequently, RF sputtering has found wide application in the industry. In a DC apparatus an insulating target surface will accumulate a negative charge, which causes a floating potential negative with respect to the plasma and extinguish the latter. Applying a radio frequency to the electrodes, they reverse their cathode-anode polarities each half-cycle. The discharge operates at a frequency that is sufficiently high so that ions charge accumulation during each cycle is not large enough to significantly influence the voltage. To provide that, a matching network is used to match the capacitive impedance of the load and the power supply. An asymmetry must be built into the system RF voltage apparatus to avoid continually sputtering on both target and substrate. This is done by making the substrate electrode much larger than the target one.
In the magnetron sputtering magnetic field of few hundred gauss is used on the target to form an electron traps and confines electrons but not the ions. This allows higher deposition rate on larger deposition area than other sputtering techniques and a low substrate heating.
The sputtering system used in this work is constituted by a load-lock and a main chamber, the latter is outfitted with three different targets that can be activated simultaneously. Each target has its own power generator and a matching network used to minimize power losses. The targets, surrounded by lateral shields, are located into the chamber and a rotating carousel coaxial to the chamber holds the substrate in front of the targets. Deposition from one target at time is possible during the carousel rotation. The substrate is introduced in the sputtering chamber through the load-lock. In the load-lock a vacuum of 7.5×10^{-6} mbar is made by a turbomolecular pump, whereas a vacuum around 2- 3×10^{-8} mbar can be reached in the main chamber through a cryopump. The main chamber is separated from the cryopump by a throttle valve that can be partially closed allowing to operate in clean conditions during the sputtering process, but also avoiding the saturation of the cryopump by the sputtering gas. The heater located on the back side of the substrate-holder can reach temperatures up to 600 °C, that are measured by a thermocouple. The effective substrate temperature

is calibrated with the heater temperature before the deposition, by means of another thermocouple which can be located at the substrate surface. After heating, the substrate can be cooled down to room temperature by a flux of compressed air on its back side.

2.1.2 Pulsed Laser Deposition (PLD)

The technique of PLD has been used to deposit high quality films of materials using high power laser pulses (typically $\sim 10^8$ Wcm^{-2}) by melt, evaporate and ionize material from the surface of a target, as shown schematically on figure 2.2. This "ablation" event produces highly brilliant plasma plume that expands rapidly away from the target surface. Applications of the technique range from the production of superconducting and insulating circuit components to improved wear and biocompatibility for medical applications.

The vaporized material, containing neutrals, ions, electrons etc., expands rapidly away

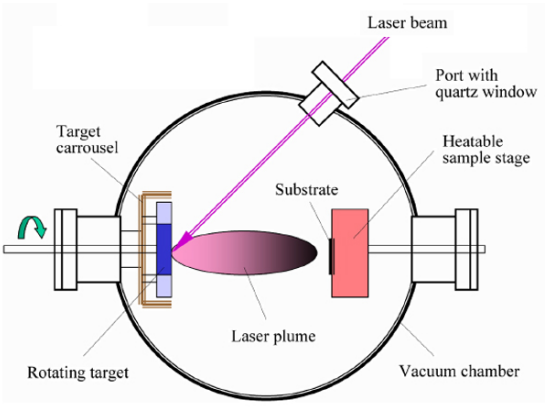

Figure 2.2: - Pulsed laser deposition apparatus

from the target surface (velocities typically $\sim 10^6$ cm/s in vacuum). Film growth occurs on a substrate upon which some of the plume material is deposited. However, the situation is not so simple, with a large number of variables affecting the properties of the film, such as laser fluence, background gas pressure and substrate temperature. These variables allow the film properties to be manipulated, but the optimization can require a considerable amount of time and effort.

The technique of PLD has significant benefits including:

- The capability for stoichiometric transfer of material from target to substrate,

- Relatively high deposition rates, typically $\sim$ 100 $\mathring{A}/min$, can be achieved at moderate laser power, with film thickness controlled in real time by simply turning the laser on and off.

- The fact that a laser is used as an external energy source results in an extremely clean process without filaments.

In spite of these advantages, PLD has also disadvantage which can be resumed in three main:

- The plasma plume created during the laser ablation process is highly forward directed, therefore the thickness of material collected on a substrate is highly non-uniform and the composition can vary across the film.

- The area of deposited material is also quite small in comparison to that required for many industrial applications.

- The ablated material contains macroscopic globules of molten material, up to $\sim$ 10 μm diameter. The arrival of these particulates at the substrate is obviously detrimental to the properties of the film being deposited.

To a large extent the first two problems have been solved. Films of uniform thickness and composition can be produced by rastering the laser spot across the target surface and / or moving the substrate during deposition. Line-focus laser spots have also been used to obtain large area coverage. The particulate material was initially removed from the plume using a mechanical velocity filter, although recently more elaborate techniques, involving collisions between two plasma plumes or off-axis deposition, have been used to successfully grow particulate-free films. The third problem will be resolved by the development of computer simulations to describe PLD, and will further our understanding of the fundamental physics and chemistry involved in the deposition process. However, a large amount of experimental data, obtained under accurately controlled and defined conditions, is required to assist the verification of such models.

2.1.3 Focused Ion Beam (FIB)

Focused Ion Beam (FIB) or general speaking ion gun techniques are not strictly a growth techniques, but in a general meaning that techniques can create a new struc-

tures from an existent one. The modern FIB systems can grow using a heated capillary inserted close to the surface and injecting a precursor gas (Pt-based metalorganic molecule) nearby the beam. Beam particles (either electrons or ions) hitting the surface deposit energy onto the precursor molecules which decompose. The volatile species leave the surface while the metal atoms are bound to it, growing very thin films.
In general, FIB system uses ion beam, i.e. Ga^+ ions, to raster over the surface of a sample (Fig. 2.3). FIB systems operate in a similar fashion to a scanning electron microscope (SEM) except FIB systems use a finely focused beam of ions that can be operated at low beam currents for imaging or high beam currents for site specific sputtering or milling. The primary ions (gallium ions in the figure) beam hits the sample

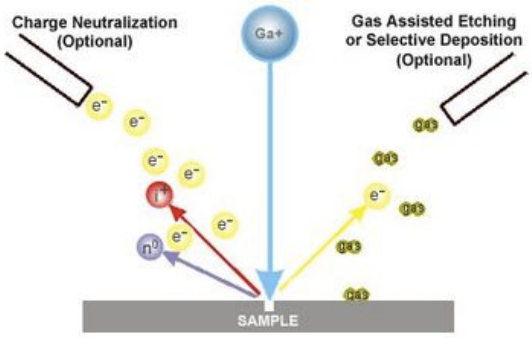

Figure 2.3: - Schematic illustration of the FIB principle

surface and sputters a small amount of material, which leaves the surface as either secondary ions (i^+ or i^-) or neutral atoms (n^0). The primary beam also produces secondary electrons (e^-). At low primary beam currents, very little material is sputtered and modern FIB systems can easily achieve 5 nm imaging resolution (imaging resolution with Ga ions is limited to 5 nm by sputtering and detector efficiency). At higher primary currents, a great deal of material can be removed by sputtering, allowing precision milling of the specimen down to a sub micrometer or even a nano scale. If the sample is non-conductive, a low energy electron flood gun can be used to provide charge neutralization. In this manner, by imaging with positive secondary ions using the positive primary ion beam, even highly insulating samples may be imaged and milled without a conducting surface coating, as would be required in a SEM. Due to the coincidence of FIB and SEM beams the Dual Beam system offers the unique capability

of sculpting, patterning and fabricating structures at the nano- or micro-scale with the FIB and to analyze them simultaneously with the high resolution, non-destructive, SEM probe. Unlike an electron microscope, FIB is inherently destructive to the specimen. When the high-energy gallium ions strike the sample, they will sputter atoms from the surface. Gallium atoms will also be implanted into the top few nanometers of the surface, and the surface, in general, change its crystalline structure. Because of the sputtering capability, the FIB is used as a micro- and nano-machining tool, to modify or materials at the micro- and nanoscale. Also FIB micro machining becomes a broad field of its own, but this is a field still developing. Commonly the smallest beam size for imaging is 2.56 nm. The smallest milled features are somewhat larger (1015 nm) as this is dependent on the total beam size and interactions with the sample being milled.

2.2 Structural analysis

Crystal structure of thin films and multilayers have been analyzed by means of X-Ray Diffraction (XRD) and High Resolution Transmission Electron Microscopy (HRTEM), in particular in the latter case by means of selected area electron diffraction (SAD). When coupling and comparing the information obtained by the two techniques, we obtain an accurate analysis of the samples characteristics on the atomic scale and determinate the epitaxial order.

2.2.1 X-Ray Diffraction

X-ray diffraction has been a well-established technique in the field of structural investigations for decades, applied not only by physicists. It represents an important tool for chemists and biologists, too, and played a decisive role in the discovery of the structure of the DNA in 1953.

X-rays are electromagnetic radiation with typical photon energies in the range of 100 eV - 100 keV. For diffraction applications, only short wavelength x-rays (hard x-rays) in the range of a few angstroms to 0.1 angstrom (1 keV - 120 keV) are used. Because the wavelength of x-rays is comparable to the size of atoms, they are ideally suited for probing the structural arrangement of atoms and molecules in a wide range of materials. The energetic x-rays can penetrate deep into the materials and provide information about the bulk structure. Common targets used in x-ray tubes include Cu and Mo,

which emit 8 keV and 14 keV x-rays with corresponding wavelengths of 1.54 and 0.8 , respectively. (The energy E of a x-ray photon and its wavelength is related by the equation $E = hc/l$, where h is Planck's constant and c the speed of light). In recent years synchrotron facilities have become widely used as preferred sources for x-ray diffraction measurements. Synchrotron radiation is emitted by electrons or positrons traveling at near light speed in a circular storage ring. When x-ray photons collide with electrons, some photons from the incident beam will be deflected away from the direction where they originally travel. If the wavelength of these scattered x-rays did not change (meaning that x-ray photons did not lose any energy), the process is called elastic scattering (Thompson Scattering) in that only momentum has been transferred in the scattering process. These are the x-rays that we measure in diffraction experiments, as the scattered x-rays carry information about the electron distribution in materials. On the other hand, in the inelastic scattering process (Compton Scattering), x-rays transfer some of their energy to the electrons and the scattered x-rays will have different wavelength than the incident x-rays. Diffracted waves from different atoms can interfere with each other and the resultant intensity distribution is strongly modulated by this interaction. If the atoms are arranged in a periodic lattice, as in crystals, the diffracted waves will consist of sharp interference maxima peaks with the same symmetry as in the distribution of atoms. Measuring the diffraction pattern therefore allows us to deduce the distribution of atoms in a material. The peaks in a x-ray diffraction pattern are directly related to the atomic distances. Let us consider an incident x-ray beam interacting with the atoms arranged in a periodic manner as shown in 2 dimensions in the following illustrations (see figure 2.4). The atoms, represented as green spheres in the graph, can be viewed as forming different sets of planes in the crystal. For a given set of lattice planes with an inter-plane distance of d, the condition for a diffraction (peak) to occur can be simply written as

$$n\lambda = 2d\dot{s}in(\theta) \tag{2.1}$$

which is known as the Bragg's law, after W.L. Bragg, who first proposed it. In the equation,λ is the wavelength of the x-ray, θ the scattering angle, and n an integer representing the order of the diffraction peak. The Bragg's Law is one of most important laws used for interpreting x-ray diffraction data. It is important to point out that the law holds true if the atoms are replaced by molecules or collections of molecules, such

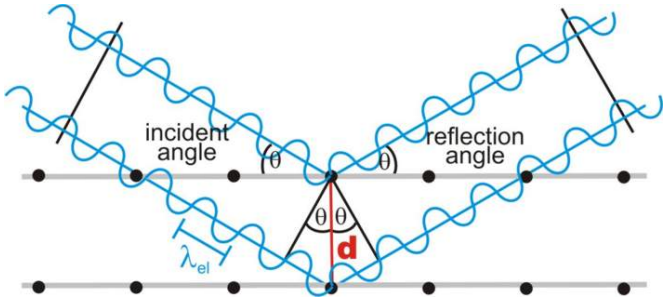

Figure 2.4: - Bragg Law representation

as colloids, polymers, proteins and virus particles. There are different XRD techniques that can be applied to the studies of thin film samples grown on substrates. Nowadays, thin films have important technological applications in microelectronic and optoelectronic devices, where high quality epitaxial films are critical for device performance. Thin film diffraction methods are used as important process development and control tools, as hard x-rays can penetrate through the epitaxial layers and measure the properties of both the film and the substrate. There are several special considerations for using XRD to characterize thin film samples. First, the film substrates are generally enough thick to avoid transmission and allow to define a specific crystallographic direction along which film grows making easier XRD measurement. Second, high angular resolution is required because the peaks from similar thin film materials are very sharp. Consequently, carefully measures and data analysis have been done. During this work X-ray diffraction (XRD) in $\theta - 2\theta$ configuration, using a Brucker AXS D8 and Phillips XPert high resolution X-ray diffractometers, have been used to characterized samples. Basic XRD measurements made on thin film samples include:

- Precise lattice constants measurements derived from $\theta - 2\theta$ scans, which provide information about lattice mismatch between the film and the substrate and therefore is indicative of strain and stress

- Rocking curve measurements made by doing a θ scan at a fixed 2θ angle, the width of which is inversely proportionally to the dislocation density in the film and is therefore used as a gauge of the quality of the film.

- Superlattice measurements in multilayered heteroepitaxial structures, which manifest as satellite peaks surrounding the main diffraction peak from the film. Film

thickness and quality can be deduced from the data.

- Glancing incidence x-ray reflectivity measurements, which can determine the thickness, roughness, and density of the film. This technique does not require crystalline film and works even with amorphous materials.

Also structural and residual stress in materials can be determined from precision lattice constants measurements.

2.2.2 Selected Area Electron Diffraction (SAED)

The traditional method for orientation determination in transmission electron microscopy (TEM) (see section 2.3.1 on TEM technique) is the use of selected area electron diffraction (SAED). This tool is used like common XRD techniques, but allows also determining the orientation relationship between two different crystalline structures and the epitaxial relationship of a specific region of the sample at the nanoscale. The SAED method selects the diffracting are of the specimen by placing a diaphragm in the first image plane below the objective lens, so only the part of the image selected by the aperture contributes to the diffraction pattern. Diffraction from single-crystal volumes yields characteristic patterns that are composed of a regular arrangement of individual diffraction spots, as shown in figure 2.5 , which can be evaluated for orientation determination. The diffraction spots are formed by coherent elastic scatter of the electrons at the crystal lattice. Because of the very short wavelength of the electron radiation,

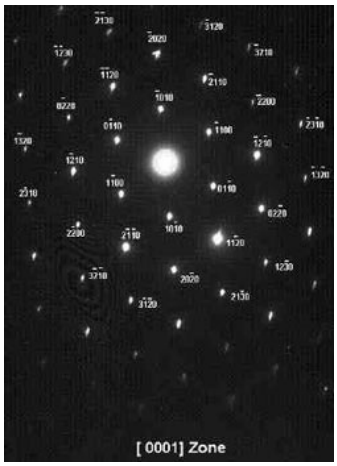

Figure 2.5: - SAD pattern of ZnO nanorod grown on Si

the diffraction angles between the reflecting lattice planes and the primary beam are very small, thus the Braggs law (2.1) can be written as

$$n\lambda = 2dsin(\theta) \approx 2d\theta = \frac{2dR_{hkl}}{2L} \tag{2.2}$$

where L is the distance between sample and camera length and R_{hkl} is the distance between primary beam and diffraction spot hkl. For a general description of the diffraction effects during SAD, the construction of the reciprocal lattice is used. Briefly, the distance between a diffraction spot in the diffraction pattern and the primary beam, that is the length of the vector R_{hkl}, is inversely proportional to the lattice spacing d (2.2) and is perpendicular to the reflecting lattice planes, the position of which can be assumed to lie in the origin of the diffraction pattern. These two conditions correspond to the definition of a point in the reciprocal lattice. It follows that each diffraction spot represents the reciprocal lattice point of the corresponding set of lattice planes hkl. Thus, the diffraction patterns can be interpreted as intersections between the points in the reciprocal lattice and the reflection sphere or Ewald sphere. As samples that are transparent to electrons must be very thin, the points in the reciprocal lattice are elongated parallel to the foil normal and get an ellipsoidal shape in reciprocal space (Fig. **??**), the so-called relrods. Furthermore, the radius of the reflection sphere, $1/\lambda$, is approximately two orders of magnitude larger than the inverse lattice constant $1/d$. Thus, the relrods can intersect with the reflection sphere even when the Bragg condition for diffraction is not exactly met. Therefore, several planes that belong to a given zone axis can contribute simultaneously to the diffraction pattern, whereas under the strict application of Braggs law only one individual diffraction spot would be expected. In modern microscopes, lens aberrations and defocusing errors are small, particulary at the high accelerating voltages (typically 200 kV) so sufficiently small apertures (5-10 μm) the spatial resolution of SAED is approximately 0.1-0.5 μm.

2.3 Morphological analysis

2.3.1 Transmission Electron Microscopy (TEM)

The Transmission Electron Microscope (TEM) has been used in all areas of scientific investigations because of its ability to view from finest cell structures to the atomic sites. For the crystallographer, metallurgist or semiconductor research scientist, current high

voltage/high resolution TEMs, utilizing 200 keV to 1 MeV, have permitted the routine imaging of crystal structures with atomic resolution, allowing materials researchers to monitor and design materials with custom-tailored properties. With the addition of energy dispersive X-ray analysis (EDX) or electron energy loss spectroscopy (EELS), the TEM can also be used as an elemental analysis tool, capable of identifying the elements at the nanoscale. The parts of a TEM are depicted in figure 2.6 and the most important are: (1) two or three condenser lenses to form the electron wave that illuminates the specimen, (2) an objective lens to form the diffraction pattern in the back focal plane and the image of the sample in the image plane, (3) several post-specimen lenses to magnify the image or the diffraction pattern on the screen. If the sample is thin ($\leq$ 200 nm) and constituted of light chemical elements, the image presents a very low contrast when it is focused. To obtain images in diffraction contrast, a small

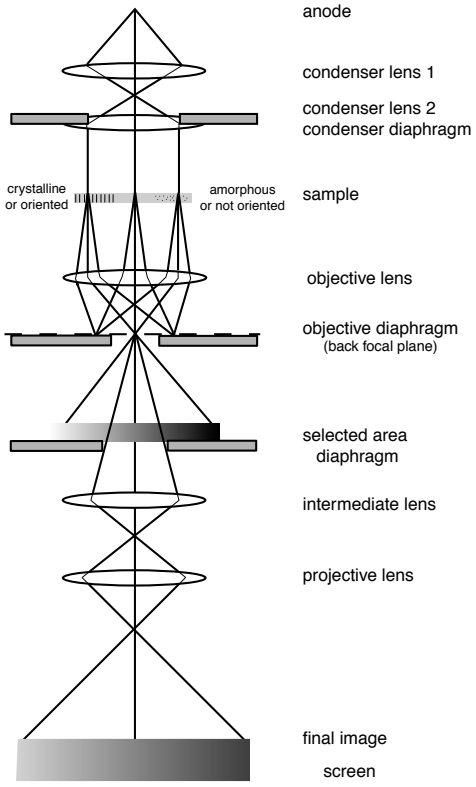

Figure 2.6: - Schematic diagram for a transmission electron microscope in image mode. In diffraction mode, the back focal plane (diffraction pattern) is projected on the screen.

objective aperture is inserted into the back focal plane of the objective lens allowing

either the transmitted beam or a diffracted beam to contribute to the image formation. These imaging modes are called BF and DF, respectively, and correspond to magnified maps of the intensity distribution of the transmitted selected beam on the exit surface of the thin crystalline sample. The complementary information obtained by BF and DF modes allows compositional analysis, crystal defect investigation and is also used to map different crystal phases at the nanoscale.

Scanning Transmission Electron Microscopy (STEM).

The basic principle of image formation in the STEM is fundamentally different from static beam TEM. An STEM machine is equipped with a scanning coil that moves the beam on the sample and a series of detector at different positions. For each beam position the signal of each detector is collected, and the final image is obtained assigning to each position the corresponding intensity.The standard detectors attached to an STEM are mainly distinguished in the BF and DF detectors with a terminology that reminds single beam diffraction contrast. Indeed a BF detector includes the transmitted beam while DF (usually anular shaped) does not. The best resolution in STEM is obtained using an annular DF detector with a large inner aperture angle being the state-of-the-art resolution 0.7 $\mathring{A}$. This technique can be referred to as HAADF (high-angle annular dark field) or simply Z contrast since it shows a high sensitivity to the atomic number Z.

High Resolution Transmission Microscopy (HRTEM).

Conventional TEM uses only the transmitted or one diffracted beam to form a diffraction contrast image. HRTEM uses the transmitted and several diffracted beams to create an interference image. The understanding of the image formation must take into account the two following steps: (1) the propagation of the incident wave through the object, which depends on the specimen, (2) the (degrading) influence of the optical system in the scattered wave (which depends on the coherence of the electron source, the stability of the microscope and the aberrations introduced by the objective lens). Therefore, HRTEM imaging requires a high performance microscope (low spherical aberration, high stability of the accelerating high tension and of the lens currents, and high mechanical stability of the column).

2.3.2 Scanning probe microscopes (SPM)

Scanning probe microscopes (SPM) define a broad group of instruments used to image and measure properties of material, chemical, and biological surfaces. SPM images are obtained by scanning a sharp probe across a surface while monitoring and compiling the tip-sample interactions to provide an image. The two primary forms of SPM are scanning tunneling microscopy (STM) and atomic force microscopy (AFM). STM was first developed in 1982 at IBM in Zurich by Binnig (Nobel Prize in Physics in 1986) [92]. Although the ability of the STM to image and measure material surface morphology with atomic resolution has been well documented, only good electrical conductors are candidates for this technique. This significantly limits the materials that can be studied using STM. In 1986, the Atomic Force Microscope was developed to overcome the basic drawback with STM [93]. The AFM, however, has the advantage of imaging almost any type of surface, including polymers, ceramics, composites, glass, and biological samples.

AFM provides a number of advantages over conventional microscopy techniques. AFMs probe the sample and make measurements in three dimensions, x, y, and z (normal to the sample surface), thus enabling the presentation of three-dimensional images of a sample surface. This provides a great advantage over any microscope available previously. With good samples (clean, with no excessively large surface features), resolution in the x-y plane ranges from 0.1 to 1.0 nm and in the z direction is 0.01 nm (atomic resolution). AFMs require neither a vacuum environment nor any special sample preparation, and they can be used in either an ambient or liquid environment. With these advantages AFM has significantly impacted the fields of materials science, chemistry, biology, physics, and the specialized field of semiconductors. Today, most AFMs use a laser beam deflection system (Fig. 2.7), introduced by Meyer and Amer, where a laser is reflected from the back of the reflective AFM lever and onto a position-sensitive detector. AFM tips and cantilevers are microfabricated from Si or Si_3N_4. Typical tip radius is a few of nm. Because the atomic force microscope relies on the forces between the tip and sample, knowing these forces is important for proper imaging. The force is not measured directly, but calculated by measuring the deflection of the lever, and knowing the stiffness of the cantilever. Hooks law gives $F = -kz$, where F is the force, k is the stiffness of the lever, and z is the distance the lever is bent.

Because of AFMs versatility, it has been applied to a large number of research topics.

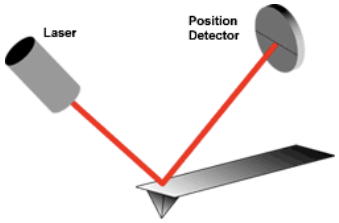

Figure 2.7: - Beam deflection system, using a laser and photodetector to measure the beam position.

The Atomic Force Microscope has also gone through many modifications for specific application requirements. Contact mode AFM is one of the more widely used scanning probe modes, and operates by rastering a sharp tip, attached to a low spring constant cantilever, across the sample. An extremely low force ($\approx 10^{-9}$ N) is maintained on the cantilever, thereby pushing the tip against the sample as it rasters. Either the repulsive force between the tip and sample or the actual tip deflection is recorded relative to spatial variation and then converted into an analogue image of the sample surface. Although operating in the contact mode has proven successful, it suffers from a number of drawbacks that limit its use on a number of sample types. First, the constant downward force on the tip often damages (and thus changes) many softer surfaces (polymers and biological samples) and even some hard surfaces such as silicon. Also, many samples, such as small particles or biological samples like DNA and cells, must be placed on a substrate for imaging purposes. In contact mode, the sample is often destroyed or even pushed out of the field of view by the rastering tip. These complications have been addressed through the development of Tapping Mode AFM. In the Tapping Mode, the AFM tip-cantilever assembly oscillates at the sample surface while the tip is scanned; thus, the tip lightly taps the sample surface while rastering and only touches the sample at the bottom of each oscillation. This prevents damage to soft specimens and avoids the pushing of specimens around on the substrate. By using a constant oscillation amplitude, a constant tipsample distance is maintained until the scan is complete. Tapping Mode AFM can be performed on both wet and dry sample surfaces. Lift Mode AFM provides the operator with a tool to record dual information about a sample surface at one location, such as topography and magnetic gradients (obtained in the magnetic force microscopy (MFM), thereby allowing the

useful association of the two images. Lift Mode AFM operates by first scanning a line on the sample surface in Tapping Mode to obtain the topographical information. Then, the tip is lifted to a distance above the sample set by the operator and the same line retraced in a non-contact mode to obtain (for example) near surface magnetic field information. The process is repeated until the scan is complete and both images are saved. To perform MFM, a ferromagnetic tip and a ferromagnetic or paramagnetic sample are required. In the standard MFM experiment, the phase shift (ϕ), of the cantilever oscillation is related to the force (F) experienced by the tip due to the magnetic stray field (H) generated by the sample according to the expression:

$$\phi = -\frac{Q}{K}\frac{\partial F_z}{\partial z} = -\frac{Q}{K}\frac{\partial^2 H_z}{\partial z^2} \tag{2.3}$$

where Q is the quality factor of the oscillation, K is the force constant of the cantilever and z the distance between the tip and the sample. Bright and dark regions in the MFM images correspond to the opposite out-of-plane components of the magnetization vector.

Lift Mode AFM can also be used to record topography and electric fields or phase imaging data.

In this work sample surface morphology has been investigated by a Dimension 3100 Atomic Force Microscope (AFM) equipped with a Nanoscope IVa controller (Veeco Instruments) and to obtain magnetic information MFM mode has been used. The AFM technology provides scientists with a powerful tool to characterize a variety of sample surfaces. Minimal sample preparation, use in ambient conditions, and the ability to image nonconducting specimens at the atomic scale (in some cases) makes AFM an extremely versatile and useful form of microscopy.

2.4 Magnetic analysis

The magnetic properties of the samples have been investigated by two magnetometers: Alternating Gradient Force Magnetometry (AGFM) and SQuID. Moreover, Magnetic Force Microscopy (MFM), described above 2.3.2, technique has been used to obtain magnetic pattern of the sample surface. In this section only magnetometer technique will be described.

2.4.1 Alternating Gradient Force Magnetometry

An AGFM is a highly sensitive measurement system, capable of measuring hysteresis properties on a wide range of sample types and strengths, in particular allows good sensitive (10^{-8} emu) magnetic measurements on thin film samples. The principle is based on the detection of the oscillation amplitude of a sample fixed on a quartz probe which vibrates in a small alternative gradient field. In an AGFM an alternating gradient field is utilized to exert a periodic force on a sample placed in an AC field. The force is proportional to the magnitude of the gradient field and the magnetic moment of the sample. The force deflects the sample and this deflection is measured by a piezoelectric sensing element mounted on the probe arm. The output signal from the piezoelectric element is synchronously detected at the operating frequency of the gradient field. Operating near the mechanical resonant frequency of the assembly enhances the signal from the piezoelectric element. This device allowing magnetic measurements up to 20 kOe good sensitivity and can measure samples with a total magnetization as small as 10^{-6} emu. Due to the high resonance frequency (typically some hundred Hz) the acquisition time is short (some minutes). The measurements can be done with a field parallel or perpendicular to the film plane.

2.4.2 SQuID

A SQuID (Superconducting Quantum Interference Device) is the most sensitive available device for measuring magnetic fields, these magnetometers are used to characterize materials when the highest detection sensitivity over a broad temperature range and using applied magnetic fields up to several Tesla is needed. Nowadays, this instrument is widely used worldwide in research laboratories. The system is designed to measure the magnetic moment of a sample, from which the magnetization and magnetic susceptibility can be obtained. Therefore, SQUID magnetometers are versatile instruments that perform both, DC and AC magnetic moment measurement. The core of instrument consists of two superconductors separated by thin insulating layers to form two parallel Josephson junctions (Fig. 2.8). The device may be configured as a magnetometer to detect small magnetic fields. The great sensitivity of the SQUID devices is associated with measuring changes in magnetic field associated with one flux quantum. One of the discoveries associated with Josephson junctions was that flux is quantized

in units

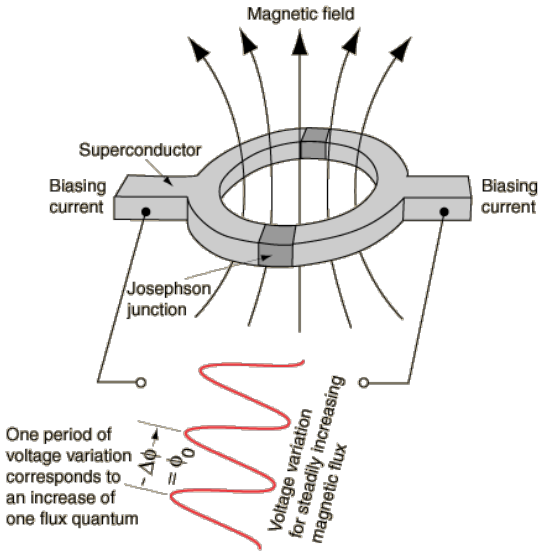

Figure 2.8: - Schematic representation of a SQuID circuit working

$$\Phi_0 = \frac{h}{2e} = 2.07 \cdot 10^{-15} Tm^2 \tag{2.4}$$

If a constant biasing current is maintained in the SQUID device, the measured voltage oscillates with the changes in phase at the two junctions, which depends upon the change in the magnetic flux. Counting the oscillations allows you to evaluate the flux change which has occurred. The main components of a SQUID magnetometer are: (a) superconducting magnet; (b) superconducting detection coil which is coupled inductively to the sample; (c) a SQUID connected to the detection coil.

2.4.2.1 Anomalous Hall Effect (AHE).

The stronger effect that Hall discovered in ferromagnetic conductors came to be known as the anomalous Hall effect (AHE). Considering a magnetic film, when a magnetic field is applied perpendicularly to the film plane and a current is injected in the x direction, in addition to the transversal voltage proportional to the applied magnetic field that corresponds to the ordinary Hall effect (OHE), appears a term derived from the spontaneous magnetization of the material. This additional contribution is the

AHE. Hall voltage for the configuration illustrated in figure 2.9 is given by:

$$V_H = \frac{R_0 I}{t} B cos\alpha + \frac{\mu_0 R_S I}{t} M cos\theta + \frac{KI}{t} M^2 sin^2\theta sin2\phi \tag{2.5}$$

where $Mcos\theta$ is the perpendicular component (normal to the film-plane) of the magnetization (M_z), $Msin\theta$ is the in-plane component (M_{xy}), I is the applied current, and t is the film thickness. $Bcos\alpha$ is the component of the applied magnetic flux density in the direction perpendicular to the current (i.e., along the film normal). When the applied magnetic field is perpendicular to the film plane, the Hall resistivity can be written as a sum of the OHE contribution, proportional to the applied magnetic field, and the AHE contribution proportional to the magnetization of the material, which is in general larger than the first term in ferromagnets:

$$\rho_H = \rho_{xy} = \mu_0(R_0 H_z + R_a M_z) \tag{2.6}$$

where only component along the perpendicular z-axis are considered.
Based on the large collections of experimental results and indications from some theoretical calculations, it is now becoming accepted that there are at least three different regimes for the behavior of AHE. The origin of the AHE has been explained by the

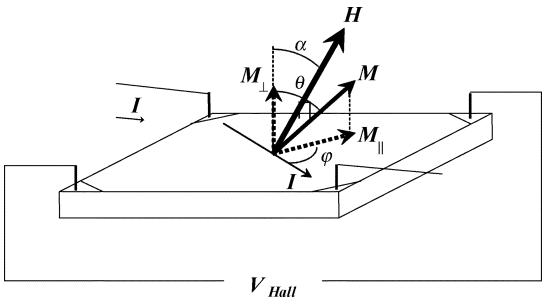

Figure 2.9: - Schematic of the configuration for the measurement of Hall voltage (V_{Hall}) in a thin film. After [94].

most recent theory by S. Onoda *et al.* [95], which distinguished these three regimes as a function of the longitudinal conductivity (σ_{xx}). A regime with extremely high conductivity ($\sigma_{xx} > 10^6 \Omega^{-1} cm^{-1}$ in which $\sigma_{xy}^{AH} \sim \sigma_{xx}$, skew scattering dominates over σ^{AH}, and the anomalous Hall angle σ^H/σ_{xx} is constant; an intrinsic or scattering-independent regime, in which σ_{xy}^{AH} is roughly independent of σ_{xx}. At lower conductivities ($10^4 \Omega^{-1} cm^{-1} < \sigma_{xx} < 10^6 \Omega^{-1} cm^{-1}$) and bad-metal regime in which σ_{xy}^{AH} decreases

with decreasing σ_{xx} at a rate faster than linear ($\sigma_{xx} < 10^4 \Omega^{-1} cm^{-1}$). In this last regime a scaling $\sigma^H \propto \sigma_{xx}^n$ with $1.6 < n < 1.8$ has been reported experimentally. For metallic thin films exhibiting this approximate scaling, it is natural that σ^H is suppressed by the strong disorder (excluding weak localization corrections).
An AHE measurement facility has been implemented in the SQuID magnetometer at the IMEM institute. Since $V_{Hall} \propto M_Z$, hysteresis loops with applied magnetic field perpendicular to the film plane are measured after capping the samples with Au thin film, in order to allow electrical conduction. The Hall voltage is measured on square (3 mm× 3 mm) samples at right angles to the applied current in the film plane, following van der Pauw method. The applied current is 1 mA and the perpendicular magnetic field up to 5.5 T. Measurements are repeated exchanging the contacts, thus the resulting measurement is a mean on four different contacts configurations.

2.5 Microfabrication

In this section will be explained all the necessary steps, made at the INESC-MN institute in Lisbon, to obtain MTJ devices with a specific pattern useful for our purpose. Discussion can be generalized, with necessary changing, to every microfabrication processes.
In magnetic tunnel junction sensors the current flows perpendicularly to the plane (CPP), therefore it is necessary to establish electrical contact to both bottom and top electrodes in order to test the electrical properties of these devices. This requires that, after all the MTJs layers are deposited into a substrate, the final device is patterned using micro-lithographic processing techniques. The fabrication of a MTJ requires a more complex process that can be divided into three steps: definition of the bottom electrode, junction area and metallic electrical contacts. To realize these steps it is necessary to perform several pattern transfer steps. Therefore, before describing the magnetic tunnel junction fabrication process, it is important to review the pattern transfer process with greater detail.
Pattern transfer There are two possible ways of transferring a pattern to a thin film during micro-fabrication: by etching (Fig. 2.10) or lift-off (Fig. 2.11). Both processes require a lithographic step in order to imprint the photosensitive polymer (photoresist - PR) with a certain pattern (mask), this imprinting allows to selectively deposit or

remove material from a substrate. During this work all the masks were created using a direct write laser (DWL) optical lithography system.

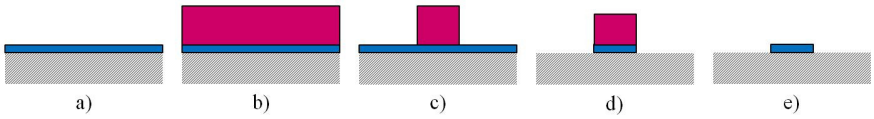

Figure 2.10: - Etching micro-fabrication process: a) Thin film deposition, b) Photoresist coating, c) Photoresist exposed and developed, d) Etching of thin film, and e) Photoresist leftovers removed by wet etching.

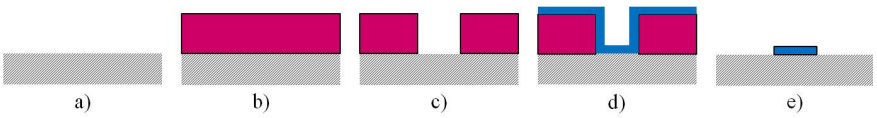

Figure 2.11: - Lift-off micro-fabrication process: a) Process starts without the thin film being deposited, b) Photoresist coating, c) Photoresist exposed and developed, d) Thin film deposition, e) Patterned thin film.

Direct write laser optical lithography The samples are coated with photoresist in a Silicon Valley Group (SVG) system. When they are exposed in a laser lithography system (i.e., DWL2.0 system from Heidelberg), the chemical bonds of the polymer are broken due to the laser wavelength (440nm NeAr). After exposure the samples are subjected to a developer in the same SVG system and the exposed photoresist is removed. The maximum feature resolution of 0.8 μm (laser spot size) and an alignment precision of 0.1 μm (related to the stage resolution) are possible.

Microfabrication steps The majority of the tunnel junctions processed during this work was microfabricated using a standard process with three lithographic steps defining: bottom electrode, junction area and metallic contacts. The standard MTJ microfabrication process will now be described:

- **Bottom electrode definition** After depositing the sample in one of the deposition system already described, the first step consists in defining the bottom electrode area by etching (Fig. 2.12).

  The sample is coated with PR in one line of the SVG, then a lithography is performed defining the bottom electrode area in the PR, the sample is developed in the second line of the SVG system removing the exposed PR, afterwards the

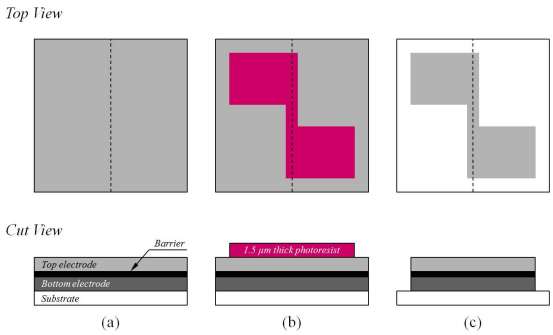

Figure 2.12: - Schematic top and cut view of the bottom electrode definition. The bulk sample deposited in a substrate (a) is patterned defining the final bottom electrode area (b), the sample is etched by ion beam milling and the photoresist leftovers are removed by wet etch (c).

sample is etched by ion beam milling removing all the unprotected material, and finally placed in a heated (at 90°C) solution with a solvent called Microstrip. The latter wet etching process is called resist strip, it can also include ultrasounds in order to facilitate the removal of all residues. The end of this first step is determined by optical inspection with a microscope.

- **Junction area definition** This second step is also done by etch, with the purpose of defining the junction area (Fig. 2.13).

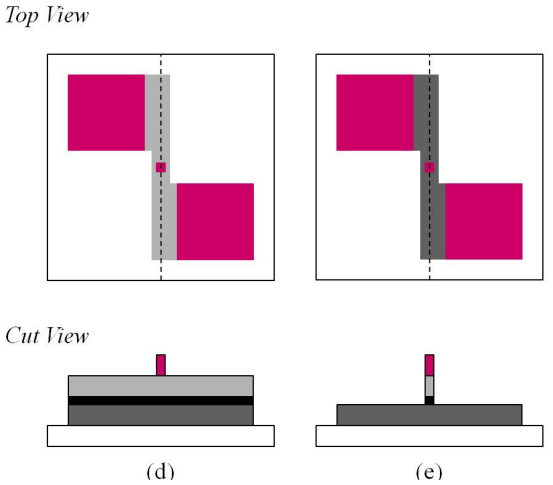

Figure 2.13: - Schematic top and cut view of the junction area definition. The sample is patterned defining the junction area and the contact pads (c), and then it is etched by ion beam milling until the bottom electrode is reached (d).

The PR is patterned defining the junction area and covering the two bottom contact pads. The latter are protected to allow a self-aligned via by lift-off of the insulator deposited in the following step. After the patterning, the unprotected material is etched by ion beam milling. In order to stop the etching right after the barrier, both timing and a calibration sample (deposited with exactly the same layers to be removed) are used to control the ending point. The etching is stopped several times and the calibration sample analyzed, both optically and electrically (with a multimeter), to determine if all the material has already been removed. This second etch is the most critical step of the MTJ micro-fabrication process. If the etch is stopped before reaching the barrier, the junction will have the full bottom electrode area and the electrons will surely flow through pin-holes in such a large area, resulting in no TMR. If the milling is not stopped before completely etching the metal layers underneath the barrier, there will be no electrical contact to the bottom electrode and therefore no TMR will be measured. Even the etching conditions themselves must be carefully choose in order to avoid material redeposition in the junction sidewalls, which can have serious repercussions in the electrical properties of the device.

- **Insulating layer deposition** At this point the junction pillar is already defined

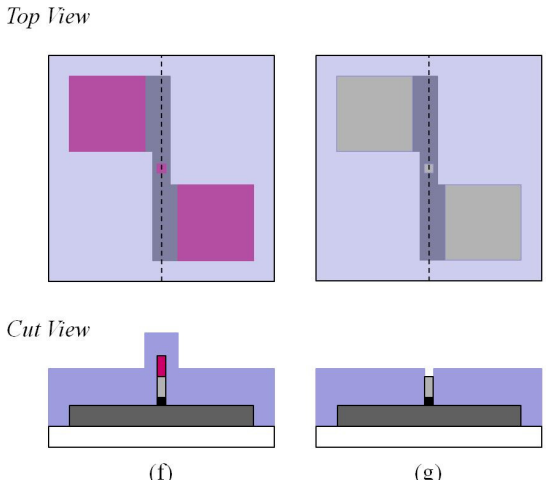

Figure 2.14: - Schematic top and cut view of the bottom electrode insulation. An insulating layer is deposited (f), and then a via is opened, through lift-off, to both the junction area and the bottom contact pads (g).

and, without removing the PR leftovers, a thick layer of insulator is deposited (typically 40 nm of Al_2O_3) with a multi-targets sputtering system. This insulating layer prevents the electrical current from flowing between bottom and top electrodes through anywhere else but the junction area. After the deposition, the remaining PR from the previous step works as a lift-off mask for the insulator (self-aligned process), as illustrated in figure 2.14. The insulator lift-off duration increases with the junction area decrease and increasing insulator thickness. For junctions with few μm and 40 nm thick Al_2O_3, the lift-off can take several days (typically more than three days).

- **Metallization** After the insulator lift-off is complete, the via to the junction area and bottom contact pads are open. In this process step, both the top lead and contact pads are defined by lift-off as illustrated in figure 2.15. After the patterning is complete, the metallization sequence is performed in a evaporation chamber. After the final lift-off step, the metal remains only on the contact pads

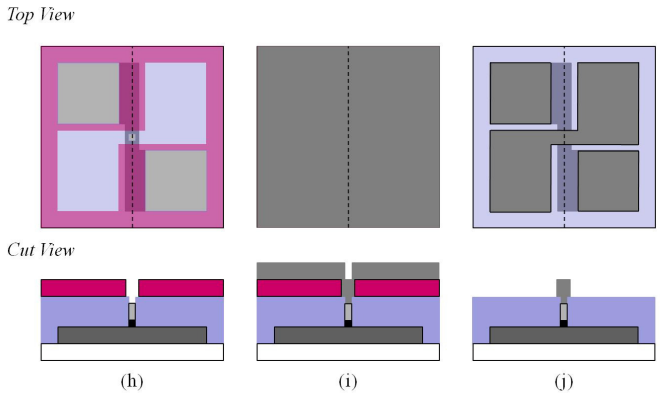

Figure 2.15: - Schematic top and cut view of the metallization process that defines the final contact leads. The sample is patterned defining the top lead and contacts, and also the bottom pads (h). Through a sputter-etch step and two metal layers deposition the entire sample is covered with metal (i).

and the top lead. The final lift-off completion is determined by optical inspection with a microscope. The standard micro-fabrication process is complete when all the metal leftovers are removed. The finalized tunnel junctions present four contact pads which allow a precise electrical characterization of the devices. In

some case, after the microfabrication, the MTJs still require magnetic thermal annealing in order to achieve their optimum properties.

3

Epitaxial thin films

3.1 Introduction

Magnetic recording (1.7) and spintronics (1.7.2) are applied fields in which the role of materials is fundamental to reach the best device performance. In particular, the growth conditions are found to have important and sometimes crucial consequences for the structural and magnetic properties of the films. In this chapter, the optimization work made to found the best growth conditions for the material studied in this thesis will be described. The growth parameters, such as growth temperature, growth rate and application of thermal treatments, are discussed as possible tools to modify the film properties. A general introduction will be done for each material deposited, such as: FePt-$L1_0$, Fe_3O_4 and MgO.

3.2 The FePt alloy

In order to increase the areal density of recording media to the order of 10 Tb/in^2, the size of a recording bit must be smaller than 10 nm. However, such a small dimension of magnetically decoupled ferromagnetic particles would make the media thermally unstable. In order to overcome this problem, FePt alloy thin films have received significant attention as magnetic recording media with the possibility to exploit the growth on different substrates to obtain the ordered $L1_0$-phase. Because of their large magnetocrystalline anisotropy energies due to the large coupling between 5*d*-element and 3*d*-element states, $L1_0$ magnetic alloys (i.e., FePt, CoPt, FePd) could play an important role in future ultra-high density magnetic recording media and spintronic devices. $L1_0$ is a crystallographic derivative structure of the fcc structure and has two of the

faces occupied by one type of atom and the other faces occupied with the second type of atoms. In particular, Fe and Pt atoms in the $L1_0$ phase occupy alternating layers along [001] axis (see figure 3.1). An important crystallographic feature of the $L1_0$-phase FePt is its c/a ratio, which is 0.963 considering a =b= 3.85 $\AA$, c=3.71 $\AA$.
According to the phase diagram Fig. 3.2), equiatomic Fe-Pt alloy exhibit a typical

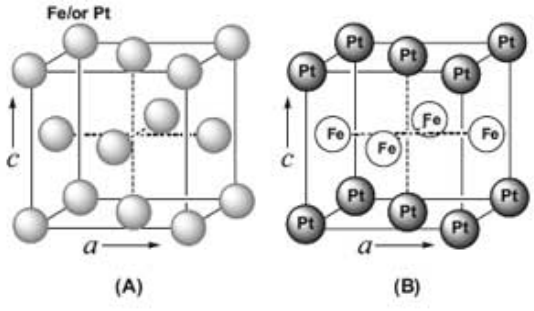

Figure 3.1: - Schematic illustration of the unit cell of A) chemically disordered fcc and B) chemically ordered fct FePt.

disorder-order transformation from the disordered cubic phase A_1-type structure, in which elements are randomly distributed across the layers, to the $L1_0$-type superstructure above the temperature of 1300° C.This phase, which is stable at low temperatures when obtained in fct-phase by melting at 1300°, is characterized by an high uniaxial magnetocrystalline anisotropy, with a first order anisotropy constant K_1 of 7×10^7 erg/cm^3, and a saturation magnetization (M_S) of 1140 emu/cm^3 for bulk [96]. The c-axis of the tetragonal structure is the easy magnetization axis. Another crystallographic phase is A_1 that is characterized by a low magnetocrystalline anisotropy energy and a spontaneous magnetization 15% higher than the hard-$L1_0$ phase [97]. Moreover, in alloy deviating from the $35\leq x\leq 55$ stochiometry, where x is the atomic content of platinum, formation of the stable cubic superstructure $FePt_3$ ($L1_2$) and Fe_3Pt ($L1_2$) is expected. This transformation occurs through a first order transition [98, 99], with a reaction homogeneous and continuous when the temperature is away from equilibrium phase boundary and below the instability temperature for disordered alloy.
When deposited in thin film-form, FePt phase diagram alloy changes due to the non-equilibrium conditions of the growth process (i.e. RF sputtering, Pulsed Laser Deposition). In particular, to produce the $L1_0$ ordered the transformation from A_1 to $L1_0$ occurs usually at temperature above 773K (650°C) [101, 102]. This ordering temper-

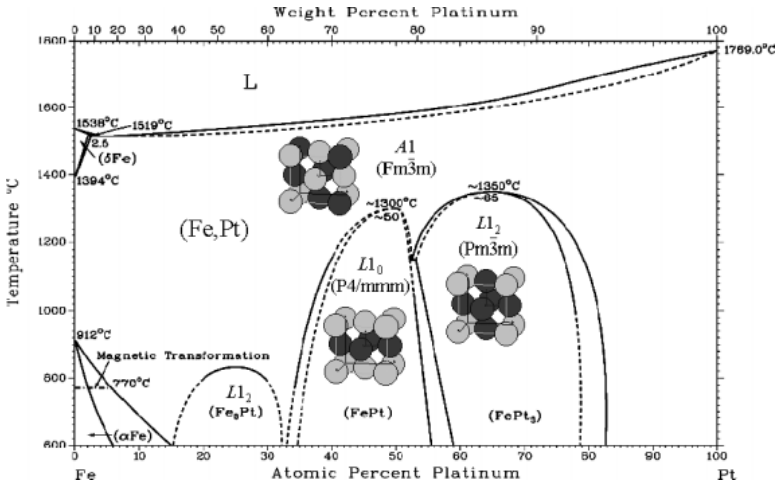

Figure 3.2: - FePt phase diagram [100]

ature is high and unfavorable for media manufacturing technologies and lead to large grains size, degrading signal-to-noise ratio. The study on possible routes to low the $L1_0$ ordering temperature of the FePt thin films are of particular interest [103, 104, 105, 106]. Epitaxial FePt (001) thin films have been obtained by co-sputtering [107], PLD [108] and molecular beam epitaxy [109] techniques, on glass or Si substrate, taking care about the Pt-silicides formation that degrade film properties [110], or on oxide as MgO or $SrTiO_3$ (section below). The nucleation process of ordered phase is governed by the adatom mobility at the growing film surface, while when a heat treatment is employed the ordering proceeds by diffusion, where the low size and high fraction of defects determine a different dynamics compared to bulk-diffusion. Since ordering process depends on film thickness, lower growth temperature can be used to grow thicker film, as shown in [101, 105]. The transformation/ordering temperature reduction has been attempted in many ways:

- Introducing third elements such as Ni, Cu [111] or Au [112].
- Employing a buffer layer such as Pt, Au, PtAu alloy [113, 114].
- Introducing stress or strain, for example from the lattice mismatch [115] or varying working pressure during deposition [116, 117].
- Ion irradiation [118].
- In situ annealing [101, 119]

In this work we have considered the effect of substrates with different lattice parameter together with the growth conditions on the formation of $L1_0$-ordered phase. By this way, the correlation among FePt thin film morphology, crystal structure, magnetism and the growth conditions has been investigated as a function of the substrate with the aim of tuning morphology and magnetism. In particular, an attractive substrate such as $SrTiO_3$ (STO) with lower misfit than on MgO, which has been employed in few published works [120, 121, 122], have been used to improve epitaxy and structural order. Exploiting the lower misfit on this substrate, we have obtained remarkable results, i.e., higher crystalline coherence and regular morphology, which is easily tunable from continuous to island-like. Another important reason in the choice of STO substrates is the deposition on the conductor Nb:STO substrates, suitable for spintronic application being a semiconductor material. Thus, the problem of the thin bottom electrode in lithography would be then avoided, since the conductive bottom electrode would be the whole substrate.
The functional characteristics of FePt thin films (i.e., morphology and magnetism) have been shown to be a function not only of the growth conditions, but also of the substrate lattice parameter. This introduces another free parameter to optimized the film growth. In particular, the study has been focused on FePt films with thicknesses of 15 nm deposited by alternated layers RF-sputtering at the IMEM. This deposition method decreases the order temperature of the FePt thin film down to the range of 400-450 $^{\circ}C$, lower than in the case of co-deposited FePt films [123].

3.2.1 FePt films growth

The increasing interest on new materials that can overcome the limits of actual data storage technologies, in particular pushing away the superparamagnetic limit, have made the systems based on FePt alloy an attractive field of research. Although the research is far from the grains size in the limit of "one-bit, one-grain", the control of grain separation is useful to study the magnetic interactions among grains in the limit of few nanometer. The single FePt thin film is not a suitable choice due to its high coercive field, but the employment in recording media such as exchange coupled system offers the opportunities to study new possible solution at the trilemma problem. There are many aspects that have to be take into account when the system complexity is increased, such as the exchange coupling among different magnetic phases and

the interface influence on the magnetic properties. Moreover, in this researching work innovative way to produce recording media are proposed and studied. These are represented by the choice of new substrate (i.e. $SrTiO_3$) and new growth method (i.e., ion implantation). Sprintronic represents a new field in which our expertise on the growth of magnetic thin films can be very helpful, in particular in the control of surface and interface quality. Thus, the ability to control the FePt growth morphology is exploited to obtain flat and continuous films, thicker than for recording purpose, grow on substrates with lower misfit.

It was reported that $L1_0$ FePt thin films can be directly formed on MgO single crystal substrates by molecular beam epitaxial (MBE) growth [124, 125]. A further processing simplification was introduced by the direct synthesis of epitaxial c-axis oriented ordered FePt by co-sputtering, with resulting properties comparable to those of the MBE growth [126]. Much attention has been paid to seek appropriate seed and buffer layers between the MgO (100) single crystalline substrate and FePt thin films [127] in order to control the crystal orientation and the degree of chemical ordering.

The efforts of this work were first focused on the deposition of high quality $L1_0$-ordered FePt films, starting from the deposition on MgO (100) and $SrTiO_3$ (STO) (100) substrates at different growth temperatures and annealing time. The starting base pressure in chamber was below 3×10^{-8}mbar and during samples deposition an Ar pressure of 1.5×10^{-2} mbar was kept constant during the growth. The process is characterized by an alternated deposition of very thin Fe and Pt layers, with nominal thickness of ~ 2 $\mathring{A}$ and target power in the range of P_{Fe}=47-52 W and P_{Pt}=32-37 W. The chosen ratio between Fe and Pt thickness corresponds to the nominal atomic composition $Fe_{57}Pt_{43}$, the effective composition of the FePt films has been estimated by energy dispersive x-ray spectroscopy (EDXS) to be $Fe_{45}Pt_{55}$. Due to the miscibility of the two metals and the high growth temperature, we have shown the the growth proceed under conditions similar to co-sputtering, which is the most commonly employed technique.

3.2.2 Epitaxial FePt films on MgO(100) substrate

The choice of MgO substrate was related to the misfit between in-plane $L1_0$-FePt lattice parameter and the MgO (100) lattice parameter (a = 4.21 $\mathring{A}$) that is about 8.55%, thus, a tensile strain along the film plane and a compressive strain in the out-of-plane direction occur. This favors the out-of-plane orientation of the c-axis, which is also the

easy magnetization axis. MgO is an oxide chemical with the lattice constant a=4.21 $\mathring{A}$ and it is extensively employed in spintronic devices as tunnel barrier, and in magneto recording media as substrate or buffer layer.

During this work, FePt films with a thickness of 15 nm have been grown on MgO(100)

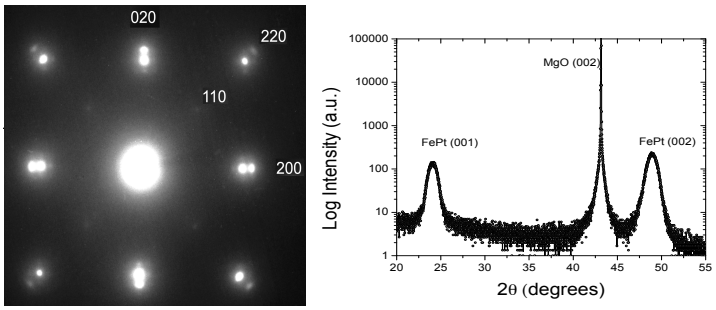

(a) (b)

Figure 3.3: a) TEM-SAED in the (001) zone axis and b) XRD pattern of FePt grown at 450° C.

substrates by RF-sputtering at 450 °C. All samples show the orientation relationship $FePt(001) < 100 > \| MgO(100) < 100 >$ at the TEM analysis. The presence of $L1_0$ ordered phase has been revealed by the appearance of the (001) superlattice spots in the SAED patterns Fig. 3.3(a)) and confirmed by the appearance in the XRD spectra of the fundamental 002 and superstructure 001 reflections Fig. 3.3(b)),no other crystallographic directions are spotted. The ordering parameter (S) has been calculated for each samples following Cebollada formula [128] and in the case of as-grown sample it has been estimated to be 0.58. HRTEM and HAADF images point out the structural quality of the films with the presence of alternating monoatomic planes along the [001] directions. Moreover, the appearance of misfit dislocations (MDs) at the film/substrate interface, reveled as regular arranged of extra-half planes, account for a complete relaxation of FePt in the first nanometer of thickness since the film grows under tensile stress.

Surface morphology has been analyzed by AFM technique in tapping mode and shows on the as-grown sample a maze-like pattern Fig. 3.4(a)) with a RMS roughness of 0.55 nm. In particular, coalescence at the grains base and irregular grains shape are observable and these features are confirmed by HAADF-TEM Fig. 3.4(b)) and STM

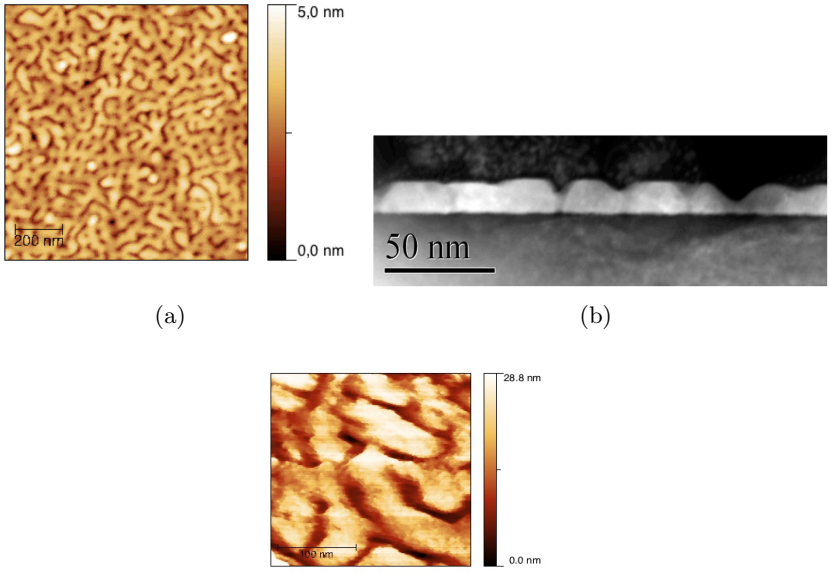

Figure 3.4: a) AFM ($1\mu m \times 1\mu m$) on as grown sample, b) HAADF-TEM images of FePt grown at 450° C and c) STM ($250nm \times 250nm$).

analysis Fig. 3.4(c)), with the latter technique used to improve lateral resolution compared to AFM analysis. These result are coherent with those obtained by our group at the IMEM on 10 nm-tick films [13].

In figure 3.5(a) are reported the hysteresis loops measured along perpendicular and parallel directions to the film plane at room temperature are reported. The loop along the easy-magnetization direction, perpendicular to the film plane, has a well-defined square shape and high remanence ratio ($(Mr/Ms)^{\perp}$=0.93) with a large coercivity ($Hc^{\perp}$=3.9 kOe). Parallel remanence is close to zero, which indicates a low fraction of magnetic phase (i.e., A1-phase) with easy axis oriented along the film plane.

The estimate value of anisotropy field is 43 kOe with a resulting uniaxial anisotropy constant of K_1=1.5×10^7 erg/cm^3. Moreover, in figure 3.5(b) MFM image taken in the virgin magnetic state on as-grown sample is reported, and it shows multigrains metastable magnetic domains pattern characterized by irregular perpendicular domains with a average size of $< d >= 130 \pm 4$ nm.

Following previous results [13, 110], the sample grows at 450° C has been *in-situ* an-

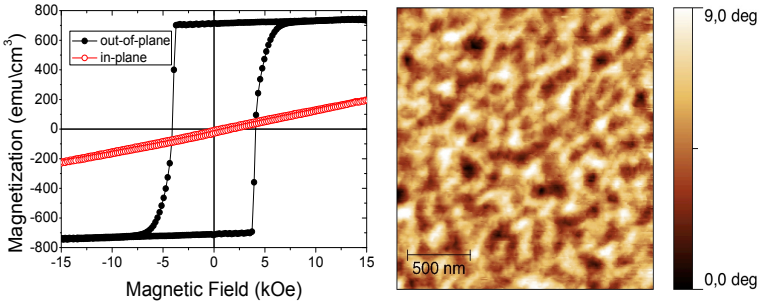

(a) (b)

Figure 3.5: Hysteresis loops measured on FePt//MgO grown at 450°C. Magnetic field is applied perpendicular (•) and parallel (∘) to the plane (left). MFM ($2\mu m \times 2\mu m$) images taken on as-grown sample.

nealed after the growth, at the same temperature as T_G, for 60, 85 and 115 minutes with the aim of improving crystalline structure quality and magnetic characteristics. The crystalline order increases following the annealing time as testified by the increase in the S value up to 0.73 after 115' of treatment, preserving the epitaxy and the orientation relationship. Ordering process is annealing-time dependent [129], but increasing annealing time above a critical values does not improve further the magnetic properties [130].

The morphology is markedly affected by annealing treatment, see figure 3.6, and it changes from maze-like into interconnected dot-like pattern with RMS value increasing up to 0.9 nm after 115 annealing. Coalescence among grains is favored by the annealing time as shown in [13].

The hysteresis loops of annealed sample, in directions perpendicular and parallel to the film plane at room temperature, are shown in figure 3.7. The annealing treatments affect magnetic parameters such as perpendicular remanence ratio, coercivity and parallel remanence (as reported in table 3.1). Calculated H_a and K_u values follows the order degree, but they are affected by an high error value that forbids to correlate with the annealing time. The remanence ratio values (M_r/M_s) follow the annealing time increasing. Moreover, annealed samples have comparable surface magnetic domains pattern, an example is shown in figure 3.8, in which perpendicular magnetic domains with a average size of $< d >= 67 \pm 10$ nm are visible.

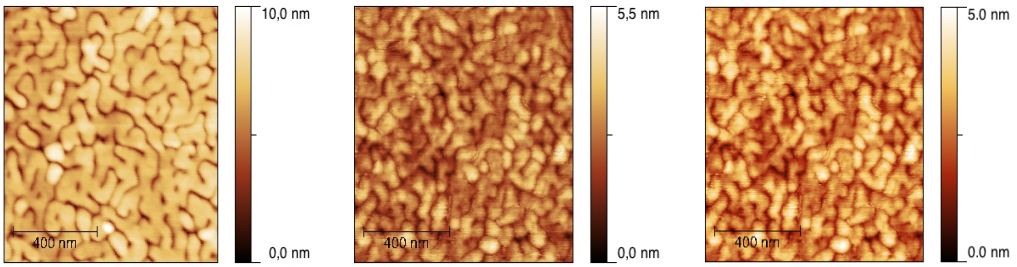

(a) (b) (c)

Figure 3.6: AFM ($1\mu m \times 1\mu m$) images taken on samples annealed for: a) 60', b) 85' and c) 115'.

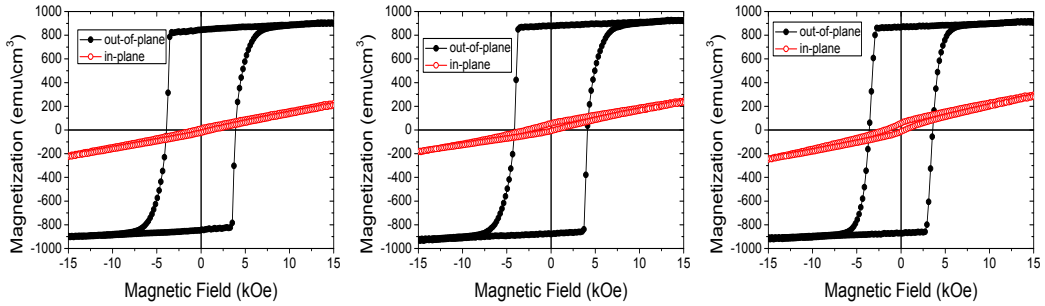

(a) (b) (c)

Figure 3.7: Hysteresis loops measured on FePt//MgO grown at 450°C anneled for: a) 60', b) 85' and c) 115'. Magnetic field is applied perpendicular (·) and parallel (○) to plane.

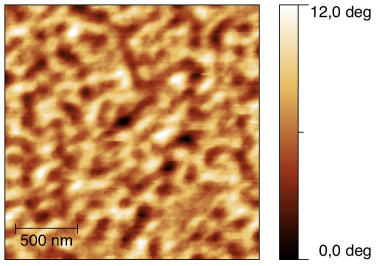

Figure 3.8: - MFM image ($2\mu m \times 2\mu m$) taken on sample grown at 450°C after 115' annealing.

Table 3.1: Coercive (H_c), anisotropy field (H_a), remanence ratio (M_r/M_s) and saturation magnetization (M_s) as a function of annealing time for FePt fim grown on MgO substrate at 450°C.

Time (minutes)	H_C(kOe)	H_A(kOe)	M_r/M_s	$M_s(emu/cm^3)$	K (erg/cm^3)
60	4.0±0.1	60±6	0.022	897±27	2.7±0.3×10^7
85	4.1±0.1	62±6	0.036	914±27	2.8±0.3×10^7
115	3.6±0.1	51±7	0.072	914±27	2.3±0.2×10^7

FePt grown on MgO substrate at lower temperature.

Takahashi *et al.* [131] found that the A1→L1$_0$ ordering starts at 300°C on MgO substrate and the degree of order increases with increasing growth temperature. Since the good results obtained at 450 °C, we decided to investigate the growth at 415°C of FePt sample with the same previous thickness to testify the possibility of film ordering at lower T$_G$. Moreover, the effects of 115' annealing at T$_G$ on this sample have been considered. As expected, the estimated order parameter is lower than in the case of T$_G$=450°C, in particular S=0.41 for as-grown sample and S=0.43 for annealed one.

AFM images show a continue and homogeneous surface morphology (see figure 3.9),

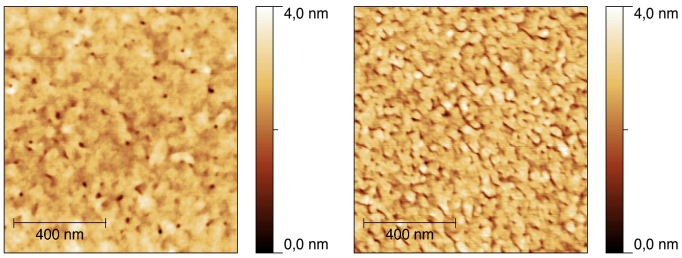

(a) (b)

Figure 3.9: AFM ($1\mu m \times 1\mu m$) images taken on samples grown at 415°C a) as-grown, b) 115' annealing .

characterized by the presence of randomly distribution holes Fig. 3.9(a)) and a RMS roughness of 0.30 nm. After annealing, the holes on surface disappear and a maze-like pattern appears Fig. 3.9(b)) with a roughness value of 0.43 nm. Annealing treatments interrupt the film homogeneity and islands are formed.

Although the low S vales, hysteresis loops Fig. 3.10) show a magnetic behavior typical

of epitaxial FePt $L1_0$ films with easy magnetization axis oriented perpendicular to the film plane and a residual magnetic phase with easy axis parallel to the film plane whose fraction is increased by annealing. The possibility to obtain $L1_0$-phase at lower growth

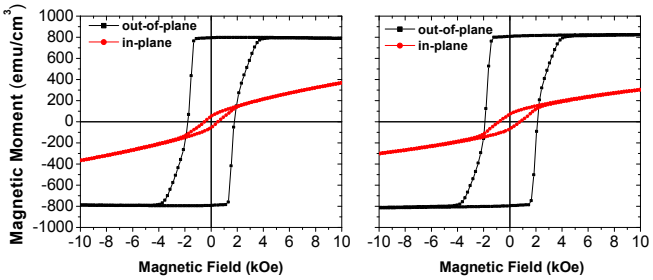

Figure 3.10: - Hysteresis loops measured on the samples grown at 415°C a) as-grown b) after 115' annealing. Magnetic field is applied perpendicular (·) and parallel (∘) to the plane

temperature has been demonstrated, showing how annealing treatment can influence magnetic parameters (see table 3.2), in particular when the growth temperature is too low for this purpose. Moreover, low growth temperature allows to obtain very flat surface.

Table 3.2: Coercive (H_c), anisotropy field (H_a), remanence ratio (M_r) and saturation magnetization (M_s) for FePt films grown on MgO substrate at 415°C.

Annealing (minutes)	H_C(kOe)	H_A(kOe)	M_r/M_s	$M_s(emu/cm^3)$	K (erg/cm^3)
0	1.8±0.1	22±3	0.067	790±40	0.8±0.1×10^7
115	2.0±0.4	38±6	0.114	820±42	1.5±0.2×10^7

In conclusion, FePt ordered perpendicular films can be grown on MgO at T_G= 450°C and 415°C. At the highest temperature the degree of order is maximum, the surface is characterized by a maze-like pattern and island coalescence is promoted by annealing, magnetic behavior is a typical of rigid magnet with easy magnetization axis perpendicular to the film plane. At the lowest T_G ordered is the lowest, film morphology is continuos and magnetization component along the film plane is present. These results suggest how the growth temperature is an important parameter to determinate sample magnetic properties. Annealing treatment can help to reach the optimal degree of order when the growth process is lacking in thermal energy and to tune morphology and magnetic properties.

3.2.3 Epitaxial FePt films on $SrTiO_3$(100) substrate

With the aim of improving FePt crystalline quality and long range order, a substrate with lower misfit has been employed. The lattice misfit between strontium titanate ($SrTiO_3$ or STO) and FePt is Δ=1.5%, therefore, the tensile strain in the film plane and compressive strain in the out of plane direction are lower than in the case of MgO substrate. $SrTiO_3$ is an oxide of strontium and titanium that is centrosymmetric with a perovskite structure at room temperature and it is characterized by a simple cubic cell with a lattice parameter a=3.91 $\mathring{A}$.
Starting from the optimized growth condition for FePt on MgO (see 3.2.1), FePt films

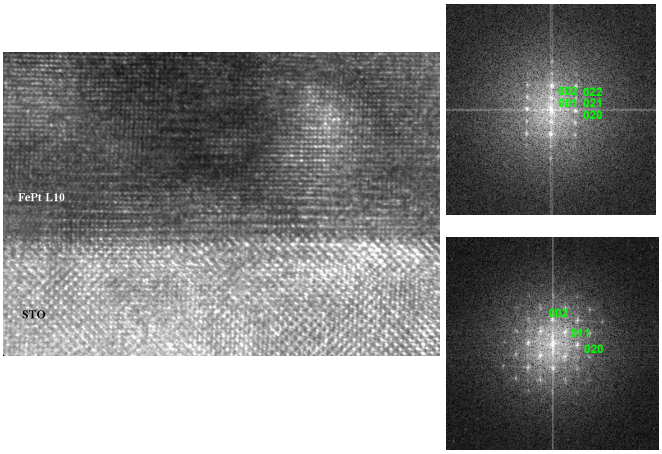

Figure 3.11: - On the left, HR-TEM on FePt film, with a thickness of 15 nm, grown on STO at 450°C. On the right, FFT images corresponding to the FePt film (top) and STO (bottom). Peaks are labeled.

with a thickness of 15 nm have been grown on STO (100) substrates at T_G=450 °C. The presence of $L1_0$ ordered phase has been pointed out by the appearance of the (001) superlattice spots in the FFT image in figure 3.11 and confirmed by the XRD spectra, as shown in figures 3.12(a) and 3.12(b), which show only the 00l reflections of the ordered $L1_0$-phase, consistently with the epitaxy shown by TEM analysis. The orientation relationship $FePt(001) < 100 > \| STO(100) < 100 >$ was found on each samples. Moreover, the appearance of $L1_0$ FePt (003) and (004) peaks confirms the orientation and the high order degree on this substrate. The order parameter for as-grown FePt film is 0.85. *Laue* oscillations are found for (001) and (002) peaks, for sample grown at 450° C on STO, indicating a high crystalline coherence along the film thickness of alter-

nating Fe and Pt atomic planes. The periodicity of the *Laue* oscillations Fig. 3.12(a)) give a coherence length equal to $\xi = 2\pi/\Delta = 9.98$ nm, remarkable compared with the film thickness of 15 nm. These oscillations are not present in the XRD spectra of film grown on MgO. HRTEM and HAADF images Fig. 3.12(c) and 3.12(d)), confirm the structural quality of the film. In particular, the cross section TEM analysis (figure

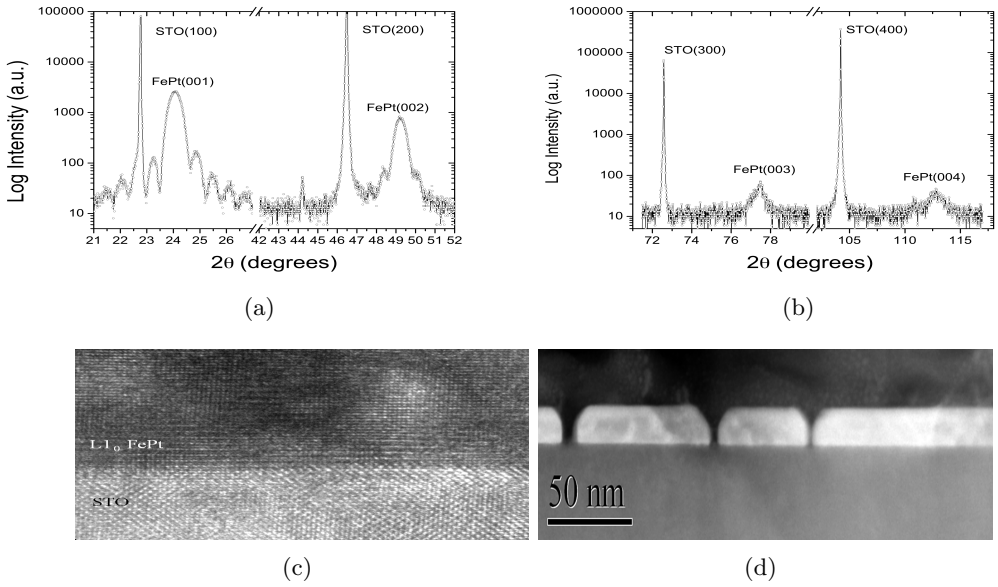

Figure 3.12: a) and b) XRD pattern of FePt grown at 450° C, c) HRTEM image of the interface between substrate and film d) HAADF-TEM images of FePt grown at 450° C.

3.12(d)), shows regular and well-separated grains shape with a gap between neighboring grains of about 2-3 nm and atomically flat top surface. The maximum grains height is 16 nm. Grains faceting is along (001),(011) and (110) directions Fig. 3.13(a)) and it is favored by the reduction of surface energy density resulting in a grain shape close to equilibrium one, which was proposed by Hong *et al.* for FePt nanoparticles systems [132].

Morphology analysis by AFM techniques has shown an island-like pattern on the as-grown sample, as shown in figure 3.13(b), with a RMS roughness value of 0.92 nm. Lower values have been obtained considering the RMS roughness limited to the surface of a single grain (0.15 to 0.3 nm), so that the contribution of inter grains gap is excluded.

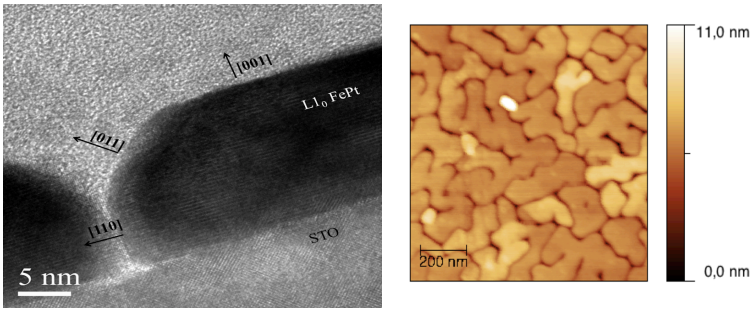

(a) (b)

Figure 3.13: a) HRTEM image showing the faceting on single FePt grain grown at 450°C on STO. Faceting directions are labeled, b)AFM ($1\mu m \times 1\mu m$) on as grown sample.

The sample has been magnetically characterized by means of SQuID at room temperature by applying the magnetic field both in the plane of the film surface and perpendicular to it, up to a maximum magnetic field of 5.5 T Fig. 3.14(a)). Hysteresis loop

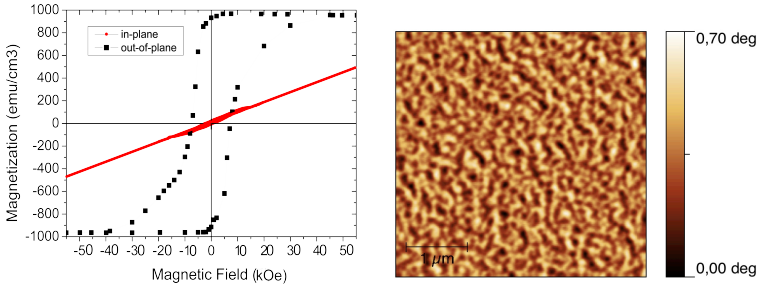

(a) (b)

Figure 3.14: a) Hysteresis loops measured on FePt as-grown on STO at 450°C. Magnetic field is applied perpendicular (·) and parallel (∘) to the plane. b) MFM ($4\mu m \times 4\mu m$) on as-grown sample.

show the easy-magnetization direction perpendicular to the film plane, a well-defined square shape and high remanence ratio ($(Mr/Ms)^{\perp}$=0.97) with a coercivity ($Hc^{\perp}$=7.5 kOe) higher than on MgO at the same growth conditions. Parallel remanence is 20 emu/cm^3, which indicates a high fraction of ordered phase with a small magnetic component lay along the film plane. The estimated value of anisotropy field is 76 kOe and the resulting K_u=3.6×10^7 erg/cm^3. The magnetocrystalline anisotropy is higher in the sample deposited on STO than on MgO.

Although in-plane strain energy is lower than on the former substrate (misfit value is 1.5%), it is sufficient to favor the formation of $L1_0$-phase and, at the same time, reduces the density of defects at the film/substrate interface, which is due to the strain relaxation process. Therefore, better crystal structure quality achieved on STO substrate allows the growth of isolated islands with low strain and with the same orientation of $L1_0$ FePt equilibrium shape [132] since not constrained by the substrate. Hence, this improvement in the magnetic anisotropy may be related to the interplay of different strain forces that promote an increasing of ordered phase obtained by the growth on STO.

The saturation magnetization (960 emu/cm^3) is higher than in the case of MgO substrate. Concurrent causes such as change in the magnetic interaction between surface atoms (depending on surface features as roughness and faceting) or the density of misfit dislocations can be involved. In particular, the magnetism of FePt surface alloy has been demonstrated to depend on the atomic environments of Fe and Pt atoms [133]. Hence, in the case of an island-like structure on STO substrate, the atomically flatness, sharp faceting can lead to a higher magnetic saturation.

Moreover, MFM images Fig. 3.14(b)) are characterized by a irregular perpendicular domains pattern with an average domains size of $< d >= 152 \pm 22$ nm. FePt samples have been annealed for 60', 85' and 115' as in the case of samples grown on MgO substrate. It has been shown that long annealing time treatments do not play a positive role on thin film properties both STO and MgO substrates. On the other hand, the effects on morphology for films grow on STO Fig. 3.15) lead to a progressive increase of grains separation from 2-3 nm (as-grown FePt) to 4-5 nm (after 115' annealing) and sharper grains faceting. This causes slight decrease in the substrate covered area, estimated by flooding algorithm on 1 $\mu m \times 1$ μm AFM images, from 91% to 89.5%. The treatment has not produced an evident influence on island-like morphology, as shown by AFM image (3.15). In fact, the top morphology of FePt on STO remains very similar after annealing (comparing figures 3.15(c) and 3.13(b)). The highest RMS roughness value of 1 nm is achieved after 115 minutes of treatment.

Regarding the annealing effects on magnetic properties, *in-situ* annealing increases H_c values from 7.5 kOe to 25 kOe, after 115 minutes of treatment Fig. 3.16(a)), but further time incremental does not lead to remarkable results, as shown in [129]. Annealing sligthy affects H_a, M_r, M_s and K values as reported in table 4.1. Moreover,

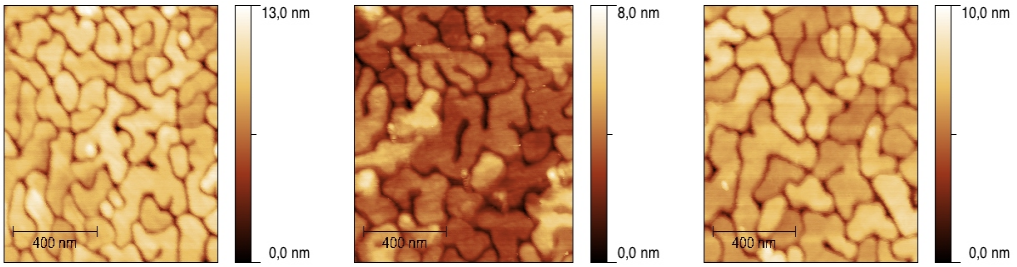

(a) (b) (c)

Figure 3.15: AFM ($1\mu m \times 1\mu m$) images taken on samples annealed for: a) 60', b) 85' and c) 115'.

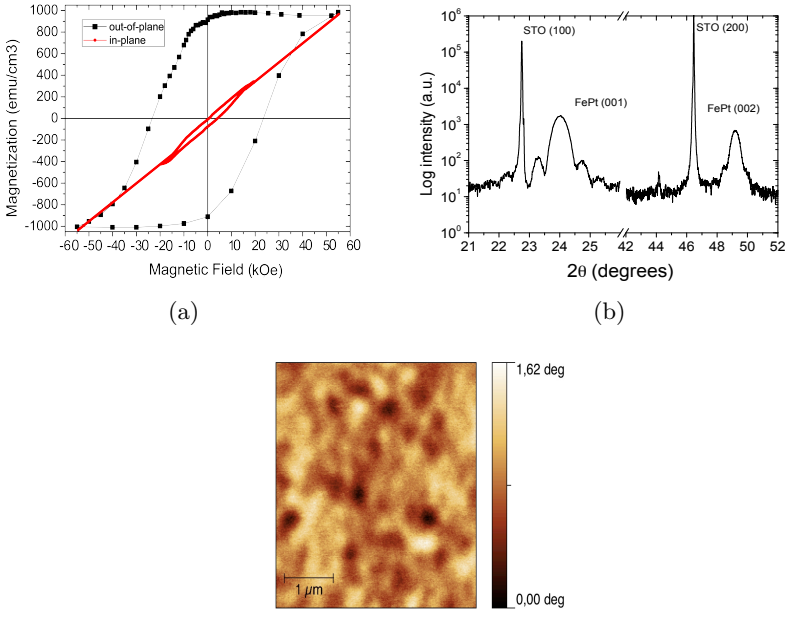

(a) (b)

(c)

Figure 3.16: a) Hysteresis loops measured on FePt//STO grown at 450°C after 115' of annealing treatment. Magnetic field is applied perpendicular (·) and parallel (○) to the plane, b) XRD pattern of FePt grown at 450 °C after 115' of annealing treatment, c) MFM ($4\mu m \times 4\mu m$) on 115' annealed sample.

Table 3.3: Coercive field (H_c), anisotropy field (H_a), remanence ratio (M_r/M_s) and saturation magnetization (M_s) as a function of annealing time for FePt fim grown on $SrTiO_3$ substrate at 450°C.

Time (minutes)	H_C(kOe)	H_A(kOe)	M_r/M_s	$M_s(emu/cm^3)$	K (erg/cm^3)
60	23.5±0.7	63±9	0.011	960±48	3±0.5×10^7
115	25±0.7	60±9	0.054	940±47	2.8±0.4×10^7

MFM images show a perpendicular magnetic domains pattern with an average domains size $< d >= 213 \pm 72$. This is explained by the increasing in the soft phase contribution as shown in 3.16(a). In figure 3.16(c) an example of MFM image is reported for the sample annealed for 115'.

FePt grown on $SrTiO_3$ substrate at lower temperature.

Taking into account the good results achieved on STO substrate and with the aim to compare the results obtained on MgO substrate, the growth temperature has been decreased to 415 °C and, in addition, the growth at the temperature of 380 °C has been considered. Despite the low T_g, the order parameter calculated was 0.51 and 0.50 at the temperature of 415 °C and 380 °C, respectively. Surprisingly , the degree of order obtained on this substrate is higher than in the case of MgO at the same growth temperature. This result points out that on STO substrate the ordering temperature can be easily reduced than on MgO, in particular for thin films. AFM images Fig.

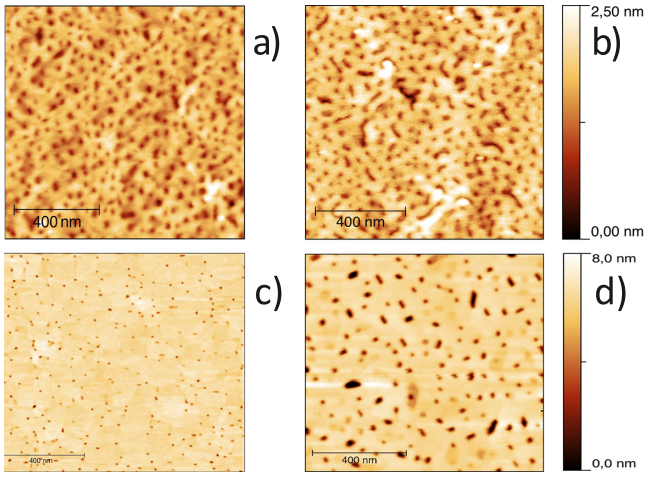

Figure 3.17: - AFM ($1\mu m \times 1\mu m$) images taken on STO samples grown at: a) 415°C, b) 380°C and c) 415°C plus 115' annealing, d) 380°C plus 11' annealing.

3.17) show a homogenous and flat surface with a RMS roughness that increases from 0.26 nm to 0.45 nm with increasing T_G. As in previous case on MgO, also on STO FePt film surface is characterized by the presence of randomly distributed holes (at 380 °C) and grooves (at 415 °C) whose density is increased by the growth temperature (see figure 3.17 (a) and (b)). Remarkable is the effect of 115' annealing on the surface morphology that reduces the density of the holes in both case (see figure 3.17 c) and d)), but increases their dimensions keeping the surface flatness. The employed growth temperatures and annealing time are under the critical threshold at which grains separation occurs.

Hysteresis loops Fig. 3.18) have been measured on as-grown samples and show a easy

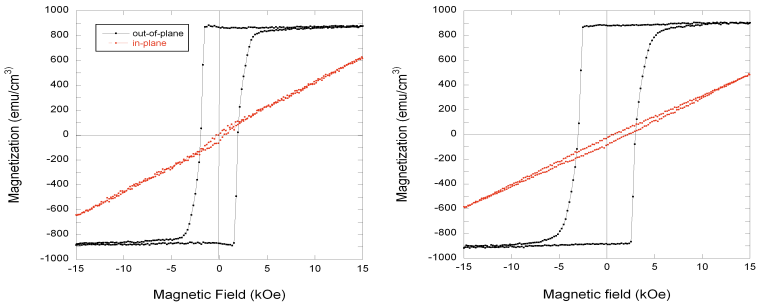

(a) (b)

Figure 3.18: Hysteresis loops measured on FePt as-grown on STO at a) 380°C and b) 415°C. Magnetic field is applied perpendicular (·) and parallel (○) to the plane.

magnetization axis oriented perpendicular to the film plane and a residual soft fraction oriented along the film plane, which decreases as T_g increases. Comparing the FePt

Table 3.4: Coercive (H_c), anisotropy field (H_a), remanence ratio (M_r/M_s) and saturation magnetization (M_s) and anisotropy constant (K) for FePt films grown on STO substrate at 380 and 415°C.

$T_g(°C)$	H_C(kOe)	H_A(kOe)	M_r/M_s	$M_s(emu/cm^3)$	K (erg/cm^3)
380	2±0.1	21±3	0.05	872±43	0.9±0.1×10^7
415	3±0.1	25±6	0.02	897±45	1.1±0.2×10^7

as-grown film on STO and MgO substrate at the same growth temperature (tables 3.4 and 3.2), it is evident that the magnetic characteristics are comparable. Thus, chemical

ordered FePt film can be grown on STO obtaining greater order degree than on MgO at the same T_G and continuous and flat surface.
In conclusion, although the lowest misfit, on STO substrate FePt $L1_0$-phase can be obtained at growth temperature as low as 380°C, without the employ of dynamic stress (e.g.,[74]) or buffer layers (e.g.,[113]). The annealing treatment allows changing in the film morphology toward grain separation and improving also the grain faceting at growth temperature of 450°C. A goal achieved by this work is the better magnetic characteristic of FePt film obtained on $SrTiO_3$ than MgO substrate.

3.2.4 Ultrathin FePt film

After the optimization of FePt growth on MgO (100) and $SrTiO_3$ (100), the following step was focused on the optimization of growth conditions of ultra thin FePt films. The attempt of ultra-thin film, with a thickness $\leq$10 nm and high uniaxial magneto anisotropy and high coercivity.
FePt film with thickness of 6, 3.5 and 2 nm have been grown on MgO and STO substrates at T_G=440 °C without annealing treatment after growth. Morphology has been analyzed by AFM for sample thickness of 6 Fig. 3.19(a) and 3.19(c)) and 3.5 nm Fig. 3.19(b) and 3.20), since the thickness of 2 nm is too thin to get a sufficient lateral resolution by the instrument. Moreover, TEM images have been taken on the sample with thickness of 3.5 nm Fig. 3.20). As found in the literature [134, 135] FePt films grow as islands on top of the MgO substrate in the Volmer-Weber three-dimensional (3D) growth mode in early stage, showing the equilibrium shapes. Also on substrate with low misfit (i.e., STO), the better crystal structure quality achieved allows the growth of isolated islands with low defects and with the same orientation of $L1_0$ FePt equilibrium shape [132], since not constrained by the substrate. At low thickness FePt film grows on MgO and $SrTiO_3$ in the same way, reaching a comparable morphology pattern characterized by small grain with an average grains size $< D >= 19 \pm 1$ nm on MgO and 21 $\pm$3 nm on STO for thickness of 3.5 nm. The grains shape is close to that also see by Dai *et al.* [136], which evolves in the grain shape see in figure 3.12(d) increasing the thickness.
The hysteresis loops have been measured by anomalous Hall effect (AHE) techniques exploiting the SQUID superconductive magnet, since coercive field was higher than the highest AGFM magnetic field and this technique is also very sensitive to thin film

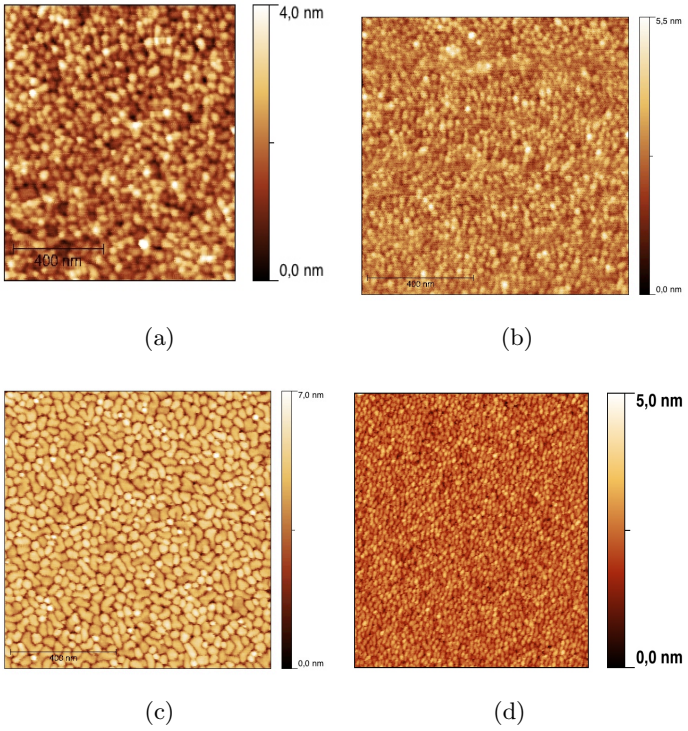

Figure 3.19: AFM ($1\mu m \times 1\mu m$) images taken on STO for thickness of a) 6 nm, b) 3.5 nm and on MgO for thickness of c) 6 nm and d) 3.5 nm.

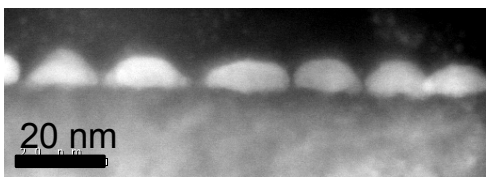

Figure 3.20: - HR-TEM image taken on 3.5-thick FePt grown on MgO substrate

magnetic moment. Hysteresis loops with field applied perpendicular to the plane are reported for film thickness of 3.5 and 6 nm Fig. 3.21). This techniques measures the

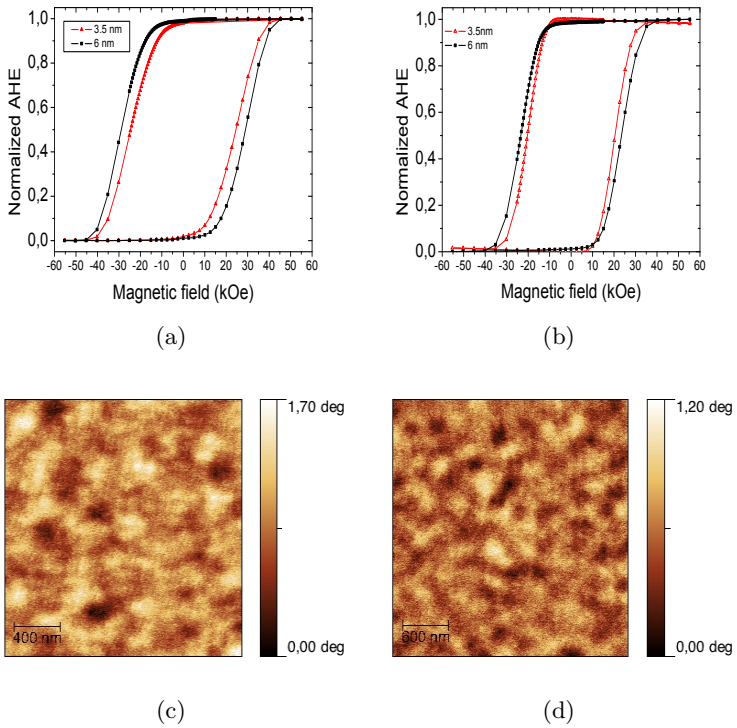

Figure 3.21: AHE loops on a) STO substrate and b) MgO substrate for 6 nm (·) and 3.5 (△) nm. Below the MFM images taken on FePt film with thickness of 6 nm at the virgin state on c) STO and d) MgO substrate.

change in AH voltage as function of applied magnetic field and is not possible to obtain M_s or $M_r^{//}$ values, because AH voltage is just proportional to perpendicular magnetization. However, $H_c^{\perp}$ value increases as function of thickness on each substrates and the highest values have been reached for the films grown on STO, as reported in table 4.3. This aspect points out that on STO substrates grains are better separated than on MgO substrate and thus. MFM images Fig. 3.21(c) and 3.21(d)) show magnetic domains extended among grains and not localized on single grain.

Comparing FePt grown on the two substrates (table 3.5), on STO coercivity field higher than on MgO has been reached, in particular values are 20% higher than on MgO at the same film thickness due to the greater grain separation and faceting achieved on

Table 3.5: Coercive field (H_c) for FePt fim grown on $SrTiO_3$ and MgO substrates as a function of thickness.

Substrate	Film thickness (nm)	H_C(kOe)
$SrTiO_3$	6	29±1
MgO	6	24±0.7
$SrTiO_3$	3.5	25±0.8
MgO	3.5	20.5±0.6

STO.

These results point out as ordered FePt ultra thin films can be obtained on both substrate characterized by homogenous and well separated grains morphology.

3.3 Magnetite epitaxial thin films

Among the four different iron oxides, magnetite (Fe_3O_4) is particularly interesting for spintronic devices such as MTJs [137], because of its high spin polarization. Theoretical calculations reveal a half-metallic behavior at room temperature with 100% negative spin polarization at the Fermi level [138]. Fe_3O_4 is also characterized by a high Curie temperature (860 K), and a characteristic metal-insulator first- order transition at 120 K (Verwey transition) [139]. The material structure is the inverse spinel structure, specified generally as AB_2O_4, two usually non equivalent metal ions, A and B, are embedded in a cubic face-centered lattice of O^{2-} ions, thus, magnetite general chemical formula can be written as $[Fe^{3+}]A[Fe^{2+},Fe^{3+}]BO_4$, where octahedral iron ions are indicated as red circles (B sites) and the tetrahedral iron ions as blue circles (A sites) (see figure 3.22). The Fe^{2+} and Fe^{3+} ions coexist at the same crystallographic site in the inverse spinel structure. The increasing interest on magnetite, as material for application in spintronics, has produced many work on the deposition of magnetite thin films using different methods such as: reactive vapor deposition, electron beam evaporation, MBE, sputtering [141] and PLD [142]. The substrates used in the growth of magnetite epitaxial films are: Si, Al_2O_3, $MgAl_2O_4$, $SrTiO_3$ and MgO. However, the most commonly chosen substrate is MgO (100), due to the small lattice mismatch with Fe_3O_4 (Δ=0.35%).

The work on the growth optimization was carried out at the Institute of Nanoscience

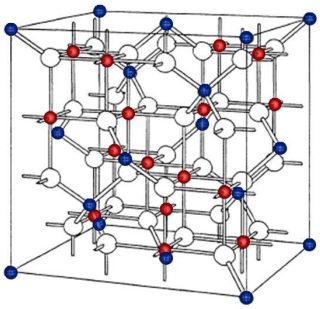

Figure 3.22: - The crystal structure of spinel Fe_3O_4. Blue atoms are tetrahedrally coordinated Fe^{3+}; red atoms are octahedrally coordinated 50% Fe^{3+} and 50% Fe^{2+}. The other are oxygen atoms. After [140]

in Aragoń (INA) by Doc. Julia Orna. Here I recall the main results reported in her Ph.D thesis [140]. During these studies, epitaxial Fe_3O_4 thin films with thickness of 45 nm have been grown on MgO (100) substrates by means of the PLD system, with a base pressure lower than 10^{-8} mbar, at the growth temperature T_G=650 °C. The PLD technique preserves the stoichiometry from the target into the deposited film for simple oxides. Therefore, the effect of the deposition rate has been studied at the first place, as it can influence both the crystalline quality of the film and its stoichiometry: too low deposition rates may produce an oxidation of the deposited material, performing an in situ reactive PLD process. After the deposition rate optimization, the influence of the growth temperature on the epitaxial growth of magnetite on MgO (100) has been studied. In order to find the optimal temperature for the epitaxial growth of magnetite on MgO (100), magnetite thin films (with thickness of 45 nm) have been grown at different temperatures from 300°C to 800°C at the optimized deposition rate (36 $\mathring{A}$/min.). The symmetrical $\theta - 2\theta$ scan around the (200) Bragg peak from the MgO substrate has shown the Fe_3O_4 (400) reflection and its Laue oscillations up to 10th order Fig. 3.23). As the Laue oscillations have its origin in the finite number of diffractive layers, from their periodicity δq, a coherence length $\epsilon = 2\pi/\delta q = 47 \pm 0.5$ nm was determined. The low-resolution TEM image in figure 3.24(a) has shown a continuous and homogeneous film. Furthermore, HRTEM images evidence the high-quality and epitaxial growth of Fe_3O_4 on MgO, showing a flat and smooth interface with MgO Fig. 3.24(b)) and the presence of structural growth defects called antiphase boundaries (APBs), which are defects originated from stress-relaxation mechanism.

From the magnetization measurements as a function of the applied magnetic field at

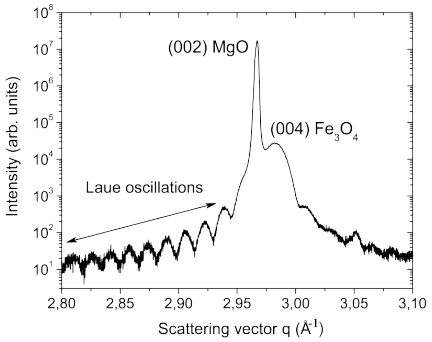

Figure 3.23: - $\theta - 2\theta$ from a 50 nm thick film grown at the optimal growth parameters. After [140].

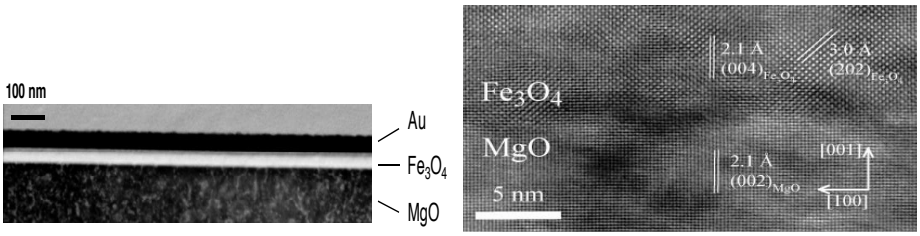

(a) (b)

Figure 3.24: $\theta - 2\theta$ from a 40 nm thick film grown at the optimal growth parameters and b) cross section HRTEM image of a MgO (100) // Fe_3O_4 film. After [140].

room temperature Fig. 2.23), a saturation magnetization value of 440 emu/cm^3 was obtained, which is about 10% less than the value reported for bulk Fe_3O_4. However, this effect has been observed before in high quality magnetite films, and is generally explained due to the presence of APBs with antiferromagnetic interactions or due to the epitaxial strain. The Verwey transition at Tv = 111 K, observed by means of

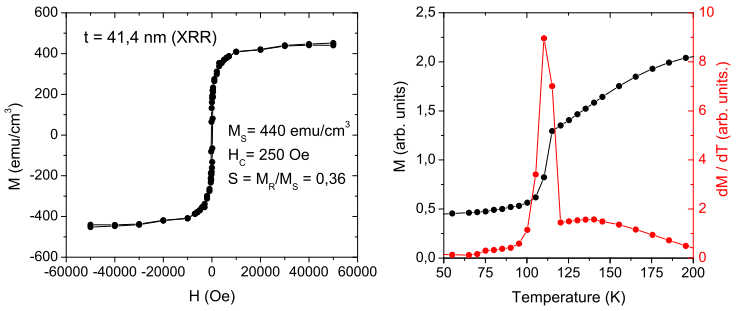

Figure 3.25: - Magnetization measurement as a function of magnetic field at room temperature (left) and FC , ZFC measurement with applied field of 500 Oe (right). After [140].

transport measurements as a function of the temperature, has been identified as a substantial increase of the resistivity at the transition temperature. Spanish collaborators

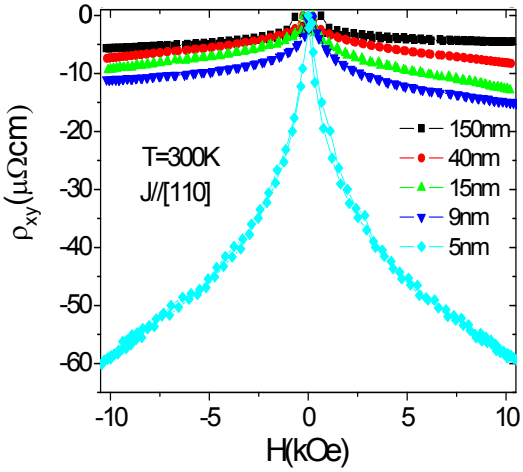

Figure 3.26: - Transversal resistivity as a function of the applied magnetic field θ=45° for several thin-film thicknesses at room temperature with current direction $J//[110]$. After [140].

have systematically characterized the magnetoresistance of magnetite films in different geometries, i.e. Hall effect and planar Hall effect, for several film thicknesses and as a

function of temperature, obtaining interesting published results [143, 144, 145]. The measurements have been done with the applied magnetic field forming a fixed angle with the current, θ=45°, since the signal will be maximum in this geometry when saturation in magnetization is reached. A value at room temperature of $\mid \rho_{xy} \mid \approx 60\mu\Omega \cdot cm$ is obtained for the film thickness of 5 nm. The peaks associated with the coercive field shift towards zero field as the sample thickness is decreased, indicating a evolution of the films towards superparamagnetic behavior.

3.4 Magnesium oxide film

Magnesium oxide (MgO) is a oxide with excellent properties such as electrical insulation, chemical stability, optical transparency, thermal conductivity and high efficiency for secondary electron emission. Moreover, it is extensively studied in spintronic devices as tunnel barrier, and in magneto recording as substrate or buffer layer. Good results have been achieved in this work (section 3.2.2) on the growth of FePt on MgO crystalline substrate, but a important goal is to obtain $L1_0$ FePt thin film on a MgO buffer layer deposited by sputtering on Si substrate, in order to lower the cost and increase the scalability of the growth process. Optimizing sputtering deposition of MgO thin film could be useful also for spintronic devices.
Several techniques have been used for deposition of MgO films, such as chemical vapor deposition [146], thermal oxidation of evaporated metal films [147], electron beam evaporation [148], laser beam evaporation [149], ion-beam assisted deposition [150] and RF-sputtering [151]. The film microstructure is a fundamental property when the film is considered for applications, thus the deposition conditions, such as temperature, pressure, target composition must be optimized to obtain an high quality crystalline structure. Magnesium oxide has a face-center-cubic (fcc) crystal structure, as NaCl-type structure, with the lattice constant a=4.21 $\mathring{A}$, and contains one formula unit per primitive cell. MgO is not a stable material, and easily reacts with moisture in the atmospheric environment, thus deposition requires high vacuum to prevent moisture reaction, as well as the formation of an amorphous oxide layer on the surface. Moreover, the MgO deposition from a bulk stoichiometric target can lead to loss of the most volatile oxygen atom, as a consequence the deposition is commonly taken in Ar and O_2

gas mixture.

In our case the presence in the sputtering chamber of pure Fe bulk target avoids the possibility to flow O_2 gas to prevent iron oxidation. Therefore, MgO films with different thickness have been deposited on Si(100) and thermal-oxide Si substrates, in the absence of an oxygen flow and at room temperature with a constant Ar pressure of 1.5×10^{-2}mbar. To found the optimal power condition, three output voltage have been tested -1200, -900 and -600 V with an output power of 154, 83 and 49 W, respectively. XRD analysis shows that at -600 V MgO grows on Si or thermal-oxide Si does not show the characteristic 200 peak, since there is not a texture. Only in the case of -900 and -1200 V voltage output the XRD analysis Fig. 3.27) has shown only (200) peak, on both substrate.

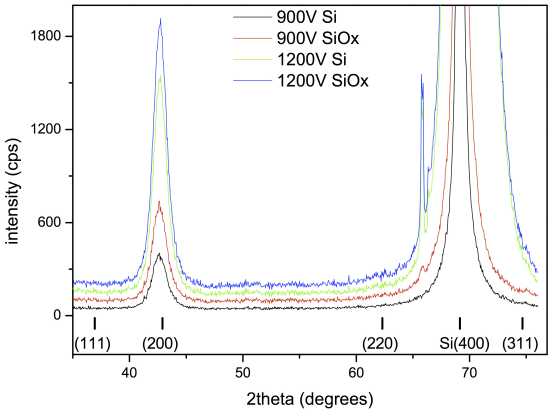

Figure 3.27: - XRD spectra of MgO film grown on Si (100) and thermal-oxide Si at -900 and -1200 V at growth temperature t_G=RT. The MgO peaks are label on the bottom, only the 200 is present.

Despite the large lattice crystalline mismatch between Si(100) and MgO ($\Delta \sim 23\%$), the MgO film grows ordered on Si substrate with cubic on cubic arrangement, and even on thermal-oxide Si. After the deposition, film thickness has been measured with a value of about 500$\mathring{A}$ at -900V and 750$\mathring{A}$ at -1200V.

After this preliminary calibration, MgO films with a thickness of 5 and 10 nm have been grown on Si and oxided-Si substrate.

Moreover, to increase the crystalline quality the growth temperature of 120 °C has been kept constant during the growth. The obtained films again have a cubic structure with 200 texture on both the substrate, shown in figure 3.28. Nevertheless, AFM image

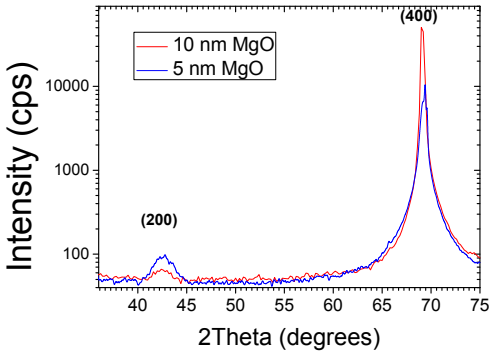

Figure 3.28: - XRD spectra of MgO film grown on thermal-oxide Si at -900 and 120°C.

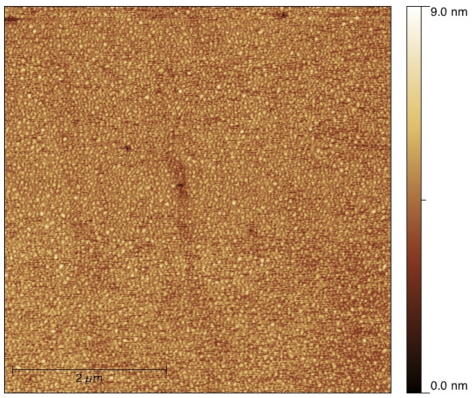

Figure 3.29: - AFM image taken on MgO film grown at RT on Si. The film thickness is 5 nm.

taken on these samples Fig. 3.29) show a surface with a high RMS roughness (∼0.85 nm) and the presence of irregular features on surface due to moisture absorption or/and sputtering growth effects.

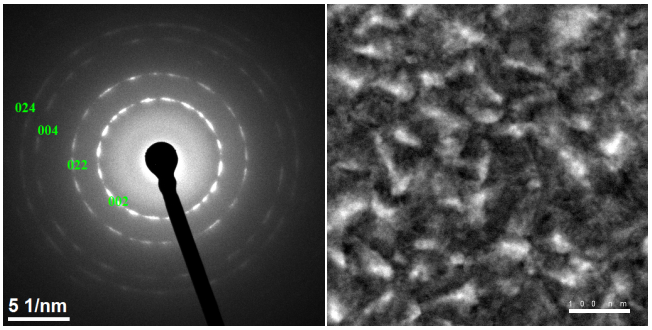

Figure 3.30: - Left: SAED pattern of MgO film grown on thermal oxided Si substrate, right: HAADF of the film surface.

TEM images, taken on MgO film grown on thermal oxides Si, show a polycrystalline film with all the grains oriented along (001) direction Fig. 3.30).The grains are rotated around the (001) axis. The orientation relationship obtained is [001]MgO‖[001]Si.
In conclusion, these results show that oriented MgO thin film on Si or Si-oxided substrates by RF sputtering without O_2 flow can be grown. Further optimization of growth conditions (i.e., T_g and deposition rate) could lead to thinner films with flatter and smoother surface. Thus, sputtered MgO layer become suitable as buffer or capping layers and as tunnel barrier in spintronic devices.

4

FePt-based recording media

Magnetic recording systems are among the most important storage data systems in information communication technology. In the early years of XXI century, the annual gain in the recording density of HDDs was eight times compared with which at the end of 1990s [3]. In 2009, recording demonstrations at density up to 519 Gb/in^2 have been reported [152]. This increase in density is due to the technology for producing materials with small size magnetic bits, keeping the number of grains/bit approximately constant and maintaining a sufficient signal/noise. Moreover, the technology for preparing magnetic heads and controlling their precision movement over the disk surface has been improved. The appearance of new technological processes in the production of write/read heads and the study of new properties of thin magnetic film made it possible to improve the recording density significantly. The recording density mainly depends on the magnetic properties of the medium, the most important of which are the value of remanent magnetization (M_R), the coercive field of the material (H_C), and the saturation magnetization (M_S). The homogeneity of magnetic domains and the anisotropy field (H_A) are also of considerable importance. Perpendicular recording provides a higher data storage density than the longitudinal mode, as discussed in section 1.7.1. Using material with high perpendicular magnetic anisotropy, such as FePt film, it is possible to increase of approximately two times the storage area density. Nevertheless, although perpendicular recording exhibits much better characteristics than the longitudinal mode, it is also susceptible to superparamagnetic effects. According to Seagate experts, the perpendicular recording, making possible to obtain a recording density up to 1 Tb/in^2 [3]. At this level, one 3.5-inch single disk platter will store 1.5 Tb of

data. Different strategies have been proposed to overcome the limits of perpendicular recording media, since the physical limits of this technology are expected to occur within 2 or 3 years and this type of recording could be replaced with patterned media or heat-assisted magnetic storage. Exchange-spring media (section 1.6), where each recording grain is composed of a hard and a soft magnetic layers, have been proposed to go beyond the limit of single layer by exploiting the hard-soft coupling to reduce the switching field and the grain size allowing to increase the storage areal density. During this thesis two different approaches to obtain FePt-based exchange-coupled systems have been studied: exchange-spring hard/soft bilayers and graded media.

4.1 ECC media: state of the art at the IMEM institute.

At the IMEM institute, the initial work on exchange-coupled bilayers was focused on the FePt/Fe system. In [119], on epitaxial FePt layers grown on MgO (100) substrate at 390 °C and 410 °C was grown a soft Fe layer obtaining a bilayers system in which a transaction between different magnetic regimes, i.e., rigid magnet (RM) to exchange-spring (ES), can be achieved increasing Fe thickness. The threshold thickness is around 2-3 nm and it is deeply influenced by both hard and soft phase anisotropy, as predicted by theoretical models [38], and extrinsic properties which influence the hard and soft coupling. Thus, the deposition of the thin Fe layer over FePt layer does not alter the structure of FePt, but deeply influences the magnetic behavior of sample that is no just a simple sum of the hard and soft contributions (Fig. 4.1). The new features is the presence of a reversible magnetization process, since the soft phase reversed by a moderate negative field promptly comes back towards the hard moment alignment when the external field is removed. As discussed in [119], this reduction of coercive field compared to the hard layer (FePt), obtained with just a Fe thickness of 2 nm, indicates that high anisotropy perpendicular media can be easily obtained with lower H_C value. By increasing the Fe thickness the FePt/Fe exchange-coupled perpendicular bilayers in both the Rigid Magnet and Exchange-Spring regimes show a drastic reduction of coercivity. The role of morphology on the hard/soft bilayers was studied in [23, 119], it was shown that when FePt film shows an island-like morphology (Figs. 4.2 (c) and (e))Fe layer follows the profile of the underlying surface, thus replicating the grain distribution, but in part grows directly on the substrate, see figure 4.2. This is favored

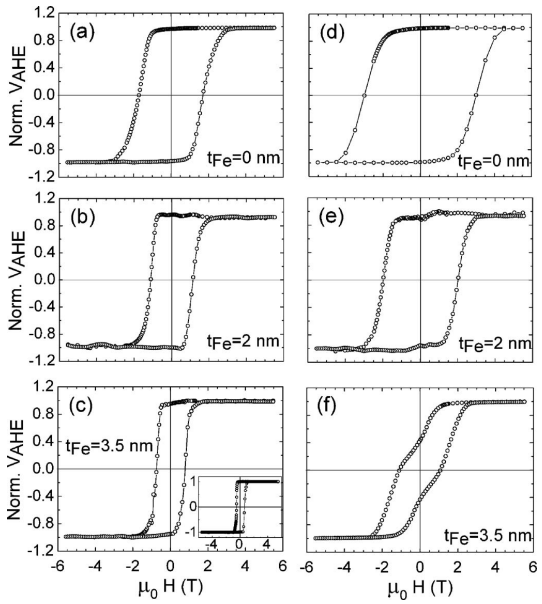

Figure 4.1: - Perpendicular hysteresis loops measured by AHE on the bilayers grown at 390°C (a-c) and 410°C. The loop of sample with tFe=3.5 nm grown at 390°C and in-situ annealed for 85' is reported in the inset in (c).Figures are taken from [119]

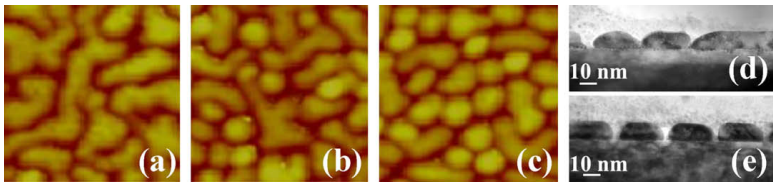

Figure 4.2: - Left: (250 nm× 250 nm) tapping mode AFM images of samples grown at (a)390 °C , (b) 390 °C plus 85' annealing and (c) 410 °C. Right: (0 1 0) cross-section TEM images of samples grown at (d) 390 °C and (e) 410 °C taken from [23]

by the growth temperature (410 °C), in fact at lower temperature (390 °C) FePt layer exhibits a semi-continuous maze-like pattern with most of the grains interconnected at the base. As a consequence, the hard/soft coupling is reduced in the samples with island-like pattern and the magnetic regime is moved to lower threshold value of soft layer thickness for the transition from RM to ES regimes.

4.2 Magnetization reversal mechanism in exchange coupled media

ECC bilayers magnetization shows a complex behaviour influenced by different factors such as microstructural features, the presence of defects and structural disorder and the interface between magnetic phases. The fundamental role played by the soft layer thickness and the film morphology was experimentally and theoretically studied in $L1_0$-FePt/Fe-based ECC bilayers by Asti et al. [38] and Casoli et al. [62]. The micromagnetic model by Asti's *et al.* described the magnetization reversal process of an ideal and infinite FePt/Fe bilayers as a function of thickness and intrinsic magnetic parameter of both hard and soft phases. Two regimes were predicted denoted as *rigid magnet* and *exchange spring* magnet, depending on the soft layer thickness. In the first regime the two layers reverse coherently, while, in the second regime the reversal of the soft phase starts at a critical field and supports the reversal of the hard phase which occurs at the irreversible field. The limit of this model was to consider as mechanism for the magnetization reversal only the rotation of magnetic moments, which does not give a full description of the reversal process in a real system. In particular, factors such as formation and evolution of magnetic domains, chemical and microstructural interface disorder as well as material microstructural features (grain boundaries, voids) were not taken into account.

To deepen the knowledge on the reversal mechanism in real system, an numerical micromagnetic model has been proposed considering the results obtained by magnetization loops at variable angle and numerical micromagnetic simulations, made at the ISM institute in Rome, and magnetic force microscopy on FePt/Fe system with variable soft layer thickness (t_{Fe} = 0, 2, 3.5 and 5 nm), grown at the IMEM institute (see in publication section [P-3]). Magnetic measurement on single FePt layer (t_{FePt}=10 nm) shows a square perpendicular hysteresis loop with a remanence ratio of 0.99 and

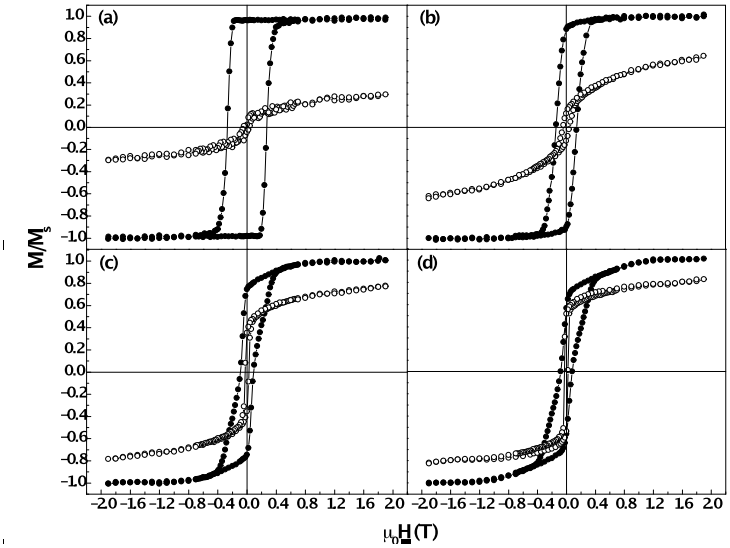

Figure 4.3: - Normalized (M/M_S) perpendicular (-●-) and in-plane (-○-) magnetization curves measured at room temperature along the field direction for soft thickness of (a) 0 nm, (b) 2 nm, (c) 3.5 nm and (d) 5 nm.

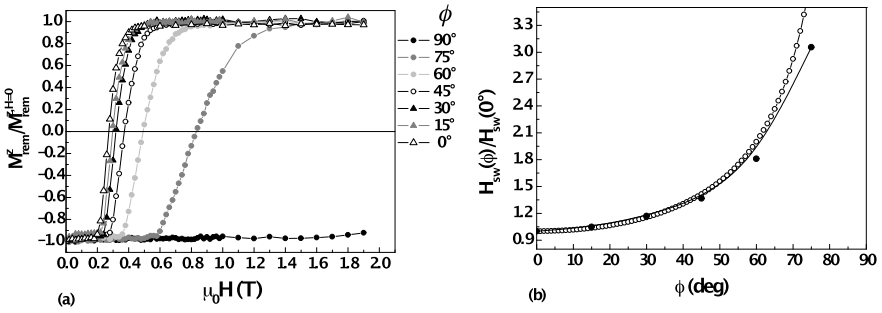

Figure 4.4: - (a) Room temperature normalized easy axis DCD curves of single FePt layer collected at different ϕ angles. (b) Comparison between the theoretical curve calculated for Kondorsky model (-○-) and the experimental angular dependence of normalized switching field ($H_{sw}(\phi)/H_{sw}0°$)) of single FePt layer (-●-).

strong effective anisotropy constant of $K_{eff} \sim 2$ erg/cm^3 (Fig. 4.3(a)). The small in-plane contribution is probably due to the presence of a residual fraction of the cubic phase or to a tilting of a small fraction of tetragonal easy axis from the ideal perpendicular direction as shown for similar sample in section 3.2.2. The relatively low value of the perpendicular coercive field ($\mu_0 H_c$= 0.27 T) is attributed to the peculiar morphology of this film, see also figure 3.4(a) in section 3.2.2. A further proof of the quasi-continuous nature of the FePt layer is given by the analysis of the reversal mechanism, which was investigated by measuring the angular dependence of the switching field (H_{sw}) as a function of angle ϕ and comparing the results with the theoretical curve calculated for the Kondorsky model (Figs. 4.4(a)-(b)), the latter describes the magnetization reversal of continuous or highly exchange coupled granular films [153]. The angular dependence of the switching field has been determined using a vectorial-VSM (vVSM) at the ISM-CNR laboratories in Rome. In particular, DCD curves have been collected at different ϕ angles along the easy magnetization axis (i.e. z-axis) by means of a non-conventional procedure, as described in [154]. The easy axis DCD curves have been used to determine the remanence coercive field (H_r) defined as the point where the remanence is equal to zero, which represents the switching field H_{sw}, as shown in [154]. The comparison between experimental and theoretical curves, reveals that the magnetic behavior of the hard FePt layer is well described by the Kondorsky model, confirming the quasi-continuous morphology of the film. Although some features of hysteresis loops are in agreement with the predictions of the micromagnetic model by Asti *et al.*, there are still some discrepancies between experimental and calculated perpendicular magnetization curves, especially in samples with thicker soft layer, where the reversal process does not proceed as a single step switching, as predicted by the model, but with a more complex mechanism, influenced by the presence of defects, interface disorder, formation and evolution of magnetic domains (Fig. 4.3(b)-(d)).
Furthermore, angular remanence curves have been done by saturating the samples at the field of 1.9 T and then measuring the remanent moment along the field direction at different ϕ angles ($m_{rem}(\phi)$), which are reported in figures 4.5(a)-(d). In the case of the single FePt layer, the polar figure shows the two-fold symmetry typical of a uniaxial system and the maximum value of the remanence has been observed at ϕ= 0° confirming the perpendicular orientation of the magnetization in the $L1_0$-FePt layer. Such symmetry is still retained at the lowest Fe layer thickness suggesting a good out-of-plane

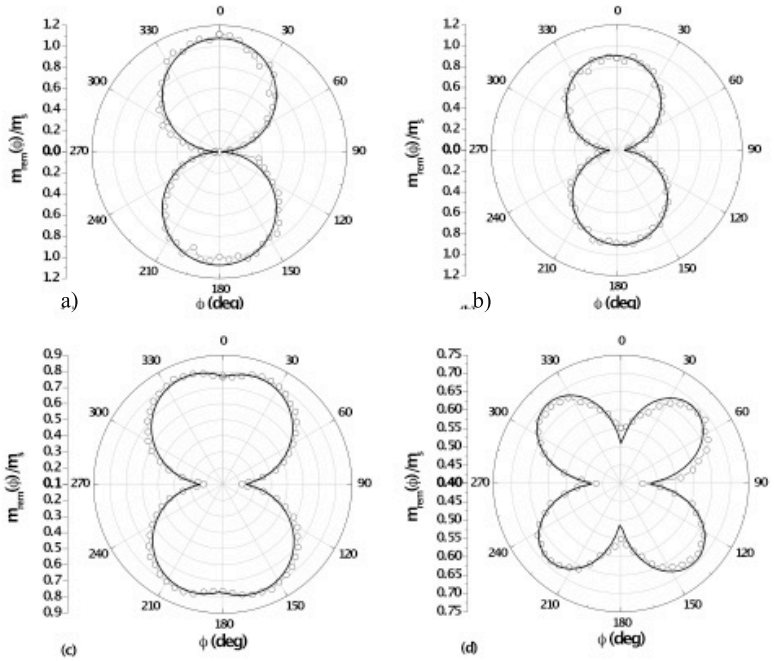

Figure 4.5: - Room temperature angular remanence curves. Experimental data (-o-) and fitting (-) for different soft layer thickness (a) 0 nm, (b) 2 nm, (c) 3.5 nm and (d) 5 nm.

alignment of hard and soft moments at remanence. For larger soft layer thickness the symmetry becomes four-fold and the maxima of remanence shift up to $\phi \sim n\pi/2$ in the sample with the highest Fe layer thickness. The change in the symmetry can be explained considering that, in samples with Fe thickness of 3.5 and 5 nm, the soft layer thickness is higher than the interlayer exchange coupling length $\lambda_{ex}=\sqrt{\frac{A}{K_{eff}}} \approx 1.19$ nm. In such a case, the magnetostatic effects become predominant with respect to the interlayer perpendicular coupling, forcing the Fe moments towards the in-plane direction. The rotation of the Fe moment towards the film plane is further proved by the analysis of the in-plane component of the magnetization (M_y) (Figs. 4.6(b)-(d)). In these measurements, taken with applied field perpendicular to the film plane, for the single FePt layer (Fig.4.6(a)) no M_y signal has been measured, whereas Fe layer is deposited the M_y/M_s signal increases on moving from the saturated to the remanent state, confirming that the Fe moments rotates toward the in-plane direction. The increment of M_y/M_s is indeed very small for t_{Fe}= 2 nm and becomes larger when $t_{Fe} > \lambda_{ex}$. The

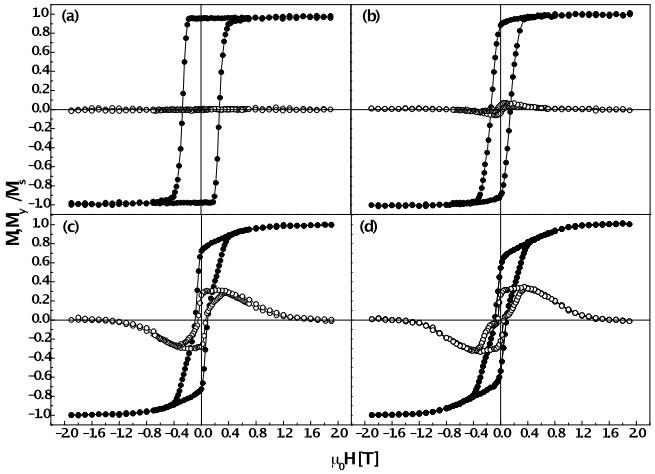

Figure 4.6: - Room temperature magnetization curves along the field direction (M_y/M_s,-○-) and the film plane (M/M_s,-●-) recorded in a hysteresis measurement cycle under a perpendicular field for soft layer thickness of (a) 0 nm, (b) 2 nm, (c) 3.5 nm and (d) 5 nm.

competition of perpendicular interlayer exchange coupling and magnetostatic effects is expected to strongly affect the magnetization reversal mechanism. For a soft layer with a thickness of 2 nm,the magnetic moments remain essentially aligned along the easy

axis of the $L1_0$-FePt layer and the bilayer exhibits a rigid magnet-like behavior. With increasing the soft layer thickness, the enhanced magnetostatic contribution combined with the interlayer perpendicular exchange coupling produces an increase of the positive critical field as well as a reduction of the perpendicular remanent ratio and coercive field, and the bilayer ,as a whole, behaves like an exchange spring system. However, since the overall magnetization reversal process cannot be satisfactorily described by the model, a numerical micromagnetic calculation of the perpendicular hysteresis loop of sample with t_{Fe} = 5 nm has been developed to better describe the actual reversal process. Figure 4.7 shows experimental and micromagnetic data for the components

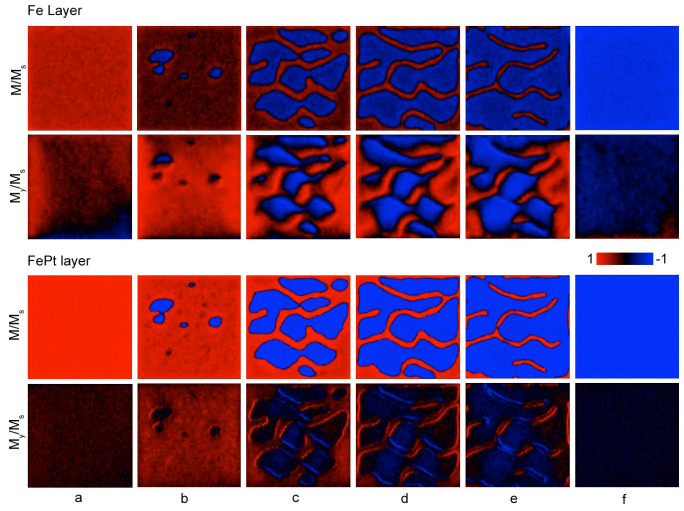

Figure 4.7: - Numerical micromagnetic simulation of magnetization parallel (M/M_s) and perpendicular (M_y/M_s) to the applied field for the hysteresis cycle of sample with the thickest Fe layer.

of the magnetization parallel to the film surface (M_y/M_s) and to the external field (M/M_s). The LLG-L equation, described in section 1.1.1, has been solved by subdividing the simulated volume with a regular mesh of prismatic cells (256x256x8 nm^3 in our case). To allow a meaningful comparison with experimental results, material parameters such as saturation magnetization M_s and uniaxial magnetic anisotropy K_u have been chosen consistently with the experimental values determined by vVSM measurements. Namely, for FePt, M_s = 750 emu/cm^3 and K_u= (0.5-1.0) erg/cm^3; a value of A$\approx 1\times10^{-6}$ erg/cm have been chosen for the exchange stiffness constant. The interlayer Fe/FePt exchange coupling (A_{int}) has been left as a free parameter in order to give the

best agreement between simulation and experiment, that is $A_{int} = 0.4\times10^{-6}$ erg/cm, in our case, which is a plausible value considering the interface roughness and possible intermixing. The simulation well reproduces the field dependence of both magnetization components, with a satisfactorily agreement between calculated and experimental squareness ratio and coercive field values. The calculation, however, tends to underestimate the field at which the loop closes in the third quadrant. Such deviations may be attributed to material microstructural features (such as defects, grain boundaries, strain relaxation and related magnetostriction in the Fe film). The LLG-L simulation software allows following the micromagnetic state during the application of the magnetic field in terms of the direction cosines of local magnetization of both soft and hard layers, thus providing detailed information on the magnetization reversal mechanism. Initially, the sample is fully saturated in the z-direction beyond $\mu_0 H_{sat}$= 2 T. As a reverse field is applied, in the range $0 < H < H_{c1}$ (point a), an in-plane component of magnetization appears in the soft layer, confirming the rotation of the Fe moments toward the in-plane direction due to the magnetostatic effects. In the same field range, the FePt moments are not affected by the reverse field and remain essentially oriented along the direction of the saturation field. At the sharp edge in the magnetization curves perpendicular reverse regions form in the soft layer which also extend in the FePt layer (point b), thus indicating that the Fe phase supports the nucleation processes of the hard phase leading to a reduction of the coercive field (point c) as expected for an exchange spring system. The MFM image of the remanent state (Fig. 4.8)

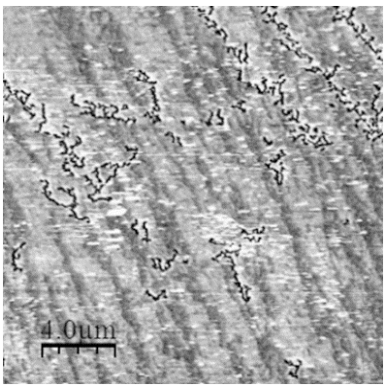

Figure 4.8: - MFM images at remanent state obtained after saturating the sample in a field perpendicular to the film plane for sample with Fe=5 nm.

shows the presence of perpendicular reverse domains and bigger stripe-like domains

with a reduced contrast, probably due to a slight tilting of the magnetization vector away from the surface plane.The micromagnetic simulation is able to reproduce the presence of magnetization reverse regions whereas large stripes domains are too wide to be handled by the computation facility available. Below the coercive field (point d-e) there is a change of the magnetization curve slope, which is not predicted analytically and could be related to a complex evolution of magnetic domains whose magnetization is directed close to the surface normal for the hard layer and close to the film plane for the soft layer. The reversal process ends with the saturation of the hard phase followed by the rotation of the Fe moments along the field direction (point f). In conclusion, the analytical model proposed by Asti can properly account for features of the reversal mechanism such as a positive nucleation fields and its decrease (increase) with increasing the soft layer thickens t_{Fe}. Nevertheless, in real systems, due to the presence of microstructural defects, interface disorder, when the thickness of soft layer is above two times the λ_{ex}, a more complete description of experimental magnetization curves can be given by numerical micromagnetic calculation. Just below the coercive field, the magnetization reversal does not proceed in a single step switching as predicted by the model, but in a more complex process: formation and evolution of magnetic domains whose magnetization is directed close to the surface normal for the hard layer and close to the film plane for the soft layer; rotation of the Fe moments along the field direction.

4.3 Exchange-spring nanostructures

Following the results obtained with FePt/Fe bilayers, the possibility to epitaxially grow on the hard $L1_0$-FePt layer a soft Fe_3Pt layer was taken into account. The objective is to improve the exchange coupling between the two magnetic layers, the structural quality and achieve a better grains separation. In addition, we have considered to exploit the growth on $SrTiO_3$ substrate. The FePt alloy can be obtained (see section 3.2) in $L1_0$-phase, which is magnetically hard, or in the ordered cubic $L1_2$-phase, which is magnetically soft, simply changing the alloy stoichiometry ratio. Moreover, exploiting the low misfit (2.86%) between two materials, a Fe_3Pt layer can be epitaxially grown on top of $L1_0$-FePt layer.

The choice of the right soft phase composition has been made after the growth of Fe_xPt_{1-x} alloy at $450°C$, with a thickness of 10 nm, on thermal oxidized Si substrate.

The Fe atomic content Fe (x) has been changed from 0.52 to 0.8 within six steps. The structural analysis on the samples (Fig. 4.9) show that increasing x from 0.52 to 0.60 fct-FePt peaks are visible. Transition from fct-phase to fcc-phase starts when fct-peaks disappears at x=0.75, which corresponds to soft phase stochiometry.

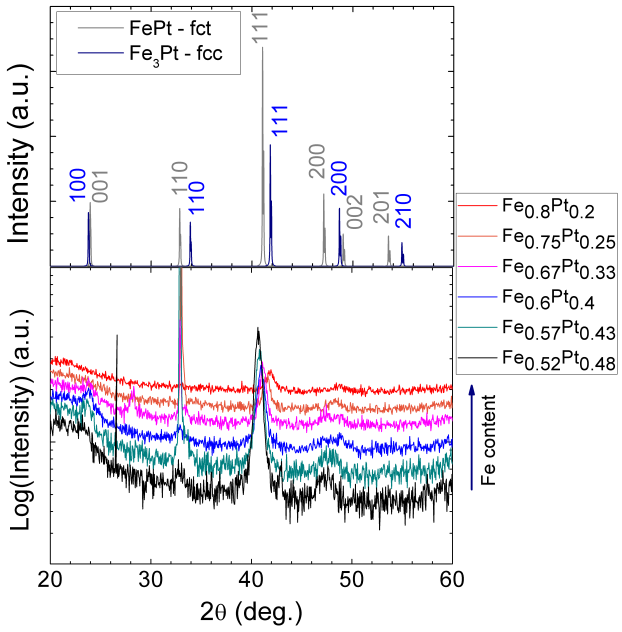

Figure 4.9: - Top figure: simulated XRD spectra of ordered FePt (gray) and Fe_3Pt (blue). Bottom figure: measured XRD spectra of samples with different Fe content.

Thus, magnetic characterization has been done on samples by AGFM (Fig. 4.10(a)) and H_C and M_S values are reported in figure 4.10(b) as a function of Fe content. As shown in figure 4.10, the soft magnetic behavior comes out when Fe content is closer to the Fe_3Pt stochiometry. Thus, the lowest coercive field and the highest saturation magnetization value have been obtained for $Fe_{0.75}Pt_{0.25}$ and $Fe_{0.8}Pt_{0.2}$ (Fig. 4.10). Bilayers have been obtained by depositing $L1_0$-FePt/Fe_xPt_{1-x} on both MgO and $SrTiO_3$ (STO) using a RF sputtering apparatus. The nominal thickness of the hard phase has been fixed to 3.5 nm, while the soft phase thickness has been varied from 2 to 5 nm. The growth has been performed at temperatures in the range 400-420 °C. Two different Fe content have been chosen to be deposited on $L1_0$-FePt underlayer: x=0.75 and 0.8. As discussed in section 3.2, in this growth temperature FePt film grows epitaxially on both MgO and STO, with (001) orientation and high degree of chemical order. Due to the

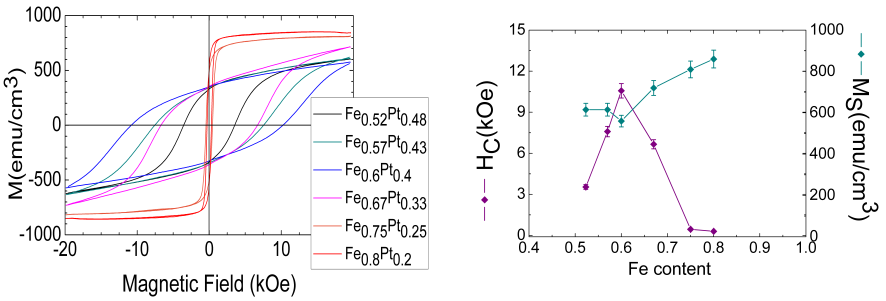

(a) (b)

Figure 4.10: a) hysteresis loops measured of Fe_xPt_{1-x}//Si grown at 450°C as a function of Fe content. Magnetic field is applied parallel to the film plane; b) H_C and M_S values as a function of Fe content.

smaller misfit, FePt on STO shows a slightly higher structural quality, well-separated and faceted grains. These morphology features have been kept after the growth of Fe_3Pt layer on top of $L1_0$-FePt. Moreover, the morphology evolution with increasing Fe_3Pt thickness is similar to the evolution found when growing $L1_0$-FePt with the same thickness and no differents in morphology have been found due to the Fe content.
Comparing AFM images taken on samples covered by Au capping layer and grown on MgO with one on STO, it is evident that surface morphology is similar both without Fe_3Pt and until Fe_3Pt thickness of 2 nm (Fig. 4.11) with a average grains diameter of 20 and 44 nm, respectively. When soft layer thickness is increased to 5 nm, surface morphology remains similar between substrates, but the grain size increases up to 56 nm on MgO and 78 nm on STO where grains are more separated than on MgO. Nanoparticles size increases with soft layer thickness, indicating that ledge, and mushroom shaped composite nanostructures have been obtained [155].

Exhaustive TEM analysis has been done on selected samples grown on STO substrate to study the nanoparticle shape and try to understand how the two crystalline phases are distributed along the thickness. High angle annular dark field (HAADF) images, taken tilting the sample, confirm grains separation shown by AFM (see figure 4.12(a)). Cross section HAADF images (Fig. 4.12(b)) show changes in Z-contrast along film thickness in which a brighter area (FePt), with a thickness of about 5 nm, and a darker area (Fe_3Pt), with a thickness of about 6.2 nm can be distinguished. HR-TEM images (Fig. 4.13(a)) show structural order and epitaxy along the film thickness, thus Fe_3Pt

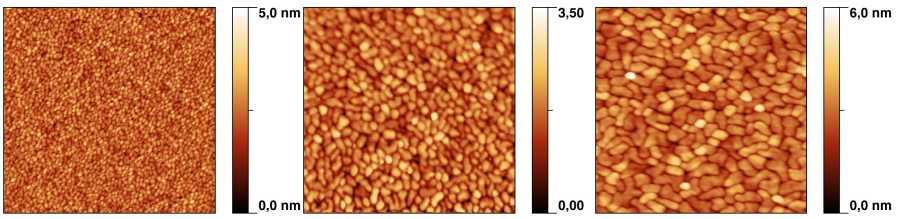

(a)

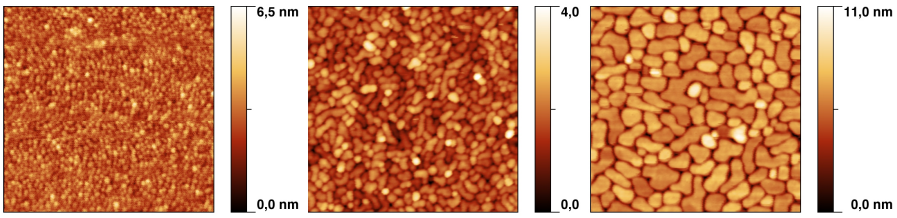

(b)

Figure 4.11: a) AFM images taken on MgO//L1$_0$-FePt/Fe_3Pt taken at different Fe_3Pt thickness (I) 0 nm ,(II) 2 nm, (III) 5 nm and (b) taken on STO//FePt/Fe_3Pt at different Fe_3Pt thickness (I) 0 nm ,(II) 2 nm, (III) 5 nm. Capping Au layer is present.

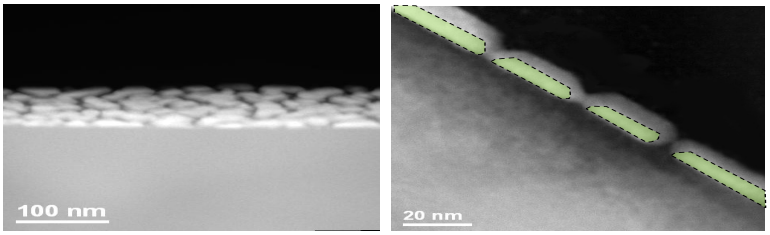

(a) (b)

Figure 4.12: a) HAADF-TEM image taken on STO//L1$_0$-FePt/Fe_3Pt sample, (b) cross section HAADF-TEM in green are with different contrast.

layer grows well ordered and pseudomorphic on the top of $L1_0$-FePt. Whereas, EDS images can not give more information about interface in the nanostructures, since no revealing different in the chemical order have been observed along the thickness (Fig. 4.13). These analysis point out a hard/soft nanoparticles epitaxially grown both MgO

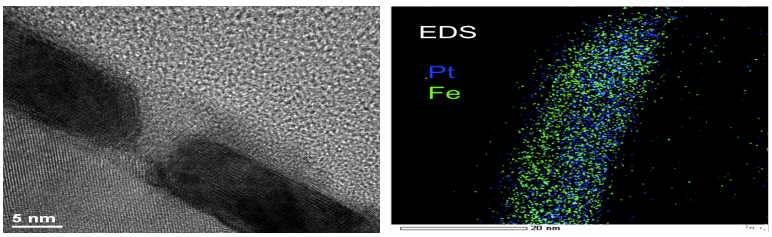

(a) (b)

Figure 4.13: a) HRTEM image taken on STO//$L1_0$-FePt/Fe_3Pt (b) EDS image taken on a single grain with in green the distribution of Fe and in blue Pt atoms.

and STO, no other crystallographic directions except those of $L1_0$ phase are present. Nanoparticles are well-separated and faceted with an average size in the range 20-80 nm , increased by soft layer thickness. Anomalous Hall Effect measurements have been done on reported samples (Figg. 4.14 and 4.15) and show a strong coercivity reduction respect to single $L1_0$-FePt layer (Figg. 4.14(a) and 4.15(a)). Comparing the measurements with different Fe content in the soft phase, on both substrates, it is evident that coercive field reduction is larger with higher Fe content (see figg. 4.14(b) and 4.14(c) for MgO substrate and 4.15(b), 4.15(c) for STO substrate). This is due to the softer magnetic behavior of $Fe_{0.8}Pt_{0.2}$ as shown in the figure 4.10(a). The coercive field reduction is larger in the samples grown on STO, this is due to the better structural quality reached for the growth on this substrate, compared with MgO, which increases exchange interaction and reduces H_C. Moreover, in these samples H_C is reduced from 24.5 to 5.2 kOe when increasing Fe_3Pt thickness to 5 nm. On both substrates, at the lowest soft phase thickness the composite nanoparticles systems exhibit a rigid magnet behavior, with an irreversible demagnetization process starting directly from the saturated state. For higher Fe_3Pt thickness, the hysteresis loops are two-step processes, typical of the Exchange-Spring regime, and a positive nucleation field, which increases with the soft phase thickness, appears for a Fe_3Pt thickness of 5 nm on MgO and for 3.5 nm on STO. Marked nucleation fields are evident in the samples grown on STO,

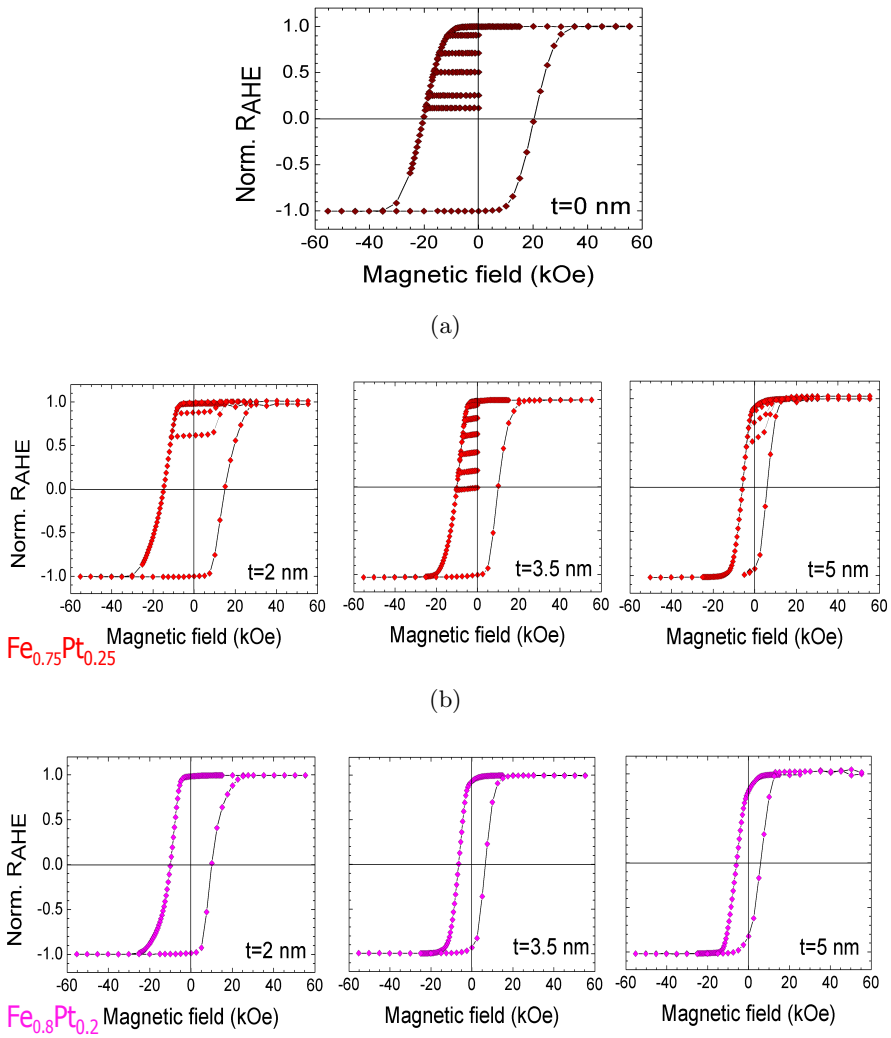

Figure 4.14: Hysteresis loops measured by the Anomalous Hall Effect on samples grown on MgO: a) 3.5 nm-tick $L1_0$-FePt; b) FePt/$Fe_{0.75}Pt_{0.25}$, c) FePt/$Fe_{0.80}Pt_{0.20}$; the Fe_3Pt layer thickness is labeled.

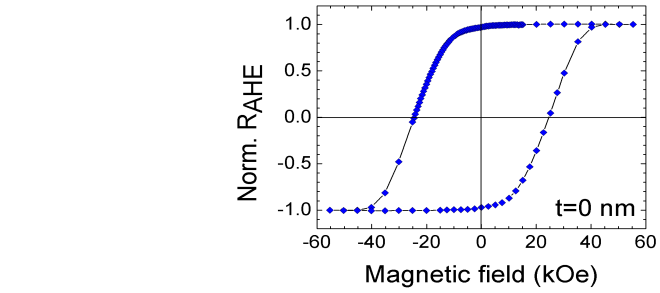

(a)

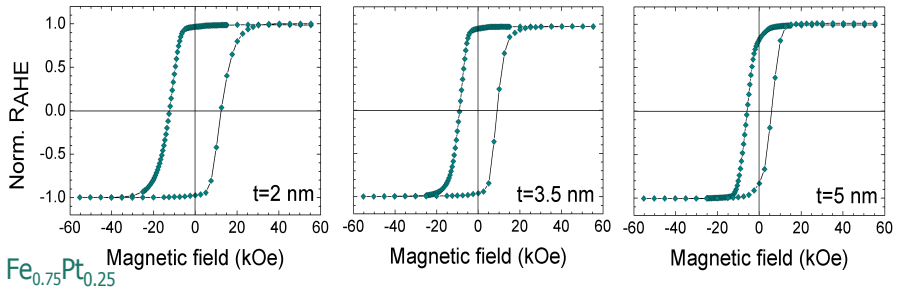

(b)

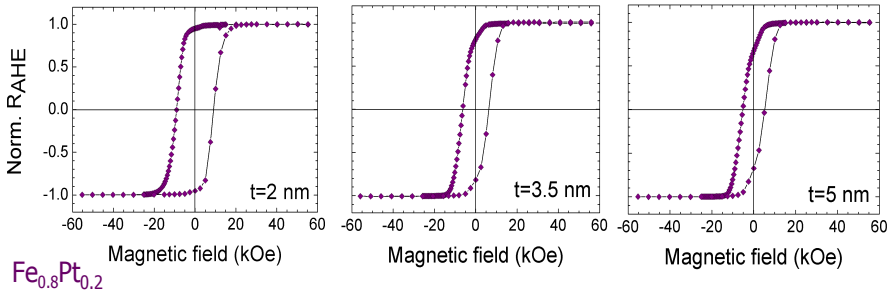

(c)

Figure 4.15: Hysteresis loops measured by the Anomalous Hall Effect on samples grown on $SrTiO_3$: a) 3.5 nm-tick $L1_0$-FePt; b) FePt/$Fe_{0.75}Pt_{0.25}$, c) FePt/$Fe_{0.80}Pt_{0.20}$; the Fe_3Pt layer thickness is labeled.

since the better structural quality obtained. With higher Fe content in the soft phase the transition thickness from rigid magnet to exchange-spring can be reduced. This is an indication of the presence of process with a reversible part that is influenced by substrate, soft layer thickness and Fe content.

The promising results obtained on sample grown on STO have been deeply studied by AHE recoil measurements (Fig. 4.16), with applied magnetic field from positive saturation down to -10 kOe. These measurements point out the reversible magnetization process, found on sample grown on STO (Fig. 4.15), as a function of Fe_3Pt layer thickness with Fe content of 0.75. With Fe_3Pt thickness of 2 nm, the magnetic behavior is Rigid Magnet (Fig. 4.16(a)), increasing the thickness up to 3.5 nm (Fig. 4.16(b)) the regime is still mainly RM only with the thickest Fe_3Pt layer of 5 nm the recoil curves slope changes and the nucleation field is dramatically reduced (Fig. 4.16(c)). In the latter case a exchange-spring regime is present. As discussed above, the magnetic

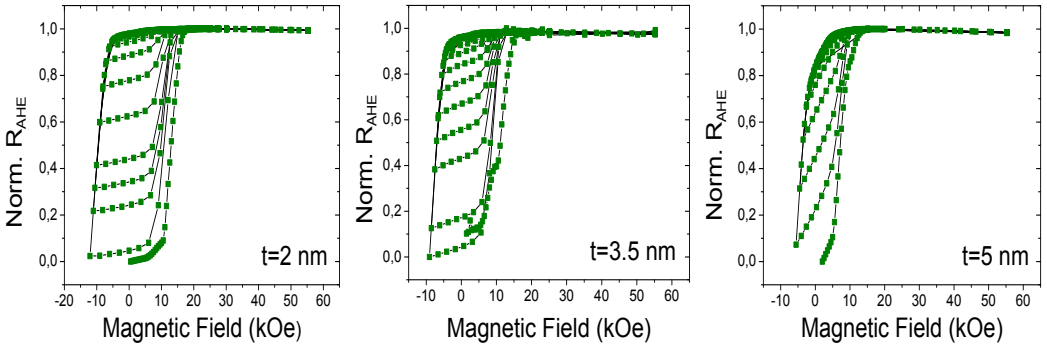

(a) (b) (c)

Figure 4.16: Recoil loops measured by the Anomalous Hall Effect on $L1_0$-FePt(3.5nm)/Fe_3Pt(x) grown on $SrTiO_3$with a) 2 nm-tick $Fe_{0.75}Pt_{0.25}$; b) 3.5 nm-tick $Fe_{0.75}Pt_{0.25}$, c) 5 nm-tick $Fe_{0.75}Pt_{0.25}$.

behavior is influenced not only by the thickness, but also by Fe content of the soft layer. As shown in figure 4.17, at the highest Fe content the slope of recoil curves is further increased respect with lower Fe content layer (Fig. 4.16) and, in addition, the nucleation field is moved towards positive value. A multistep magnetization process has been evidenced by virgin curves measurement. It is due to the coexistence of domain expansion and rotation of the soft phase moments, which are exchange coupled to the hard phase.

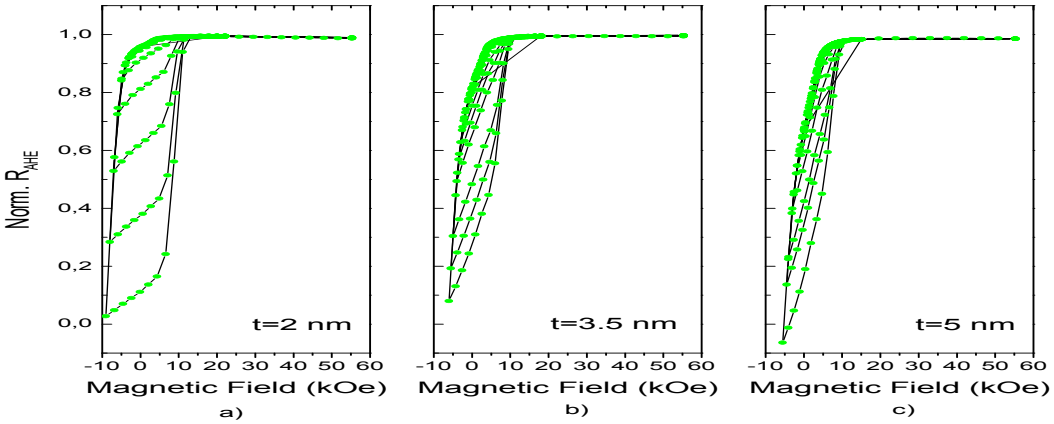

Figure 4.17: Recoil loops measured by the Anomalous Hall Effect on $L1_0$-FePt(3.5nm)/Fe_3Pt(x) grown on $SrTiO_3$with a) 2 nm-tick $Fe_{0.8}Pt_{0.2}$; b) 3.5 nm-tick $Fe_{0.8}Pt_{0.2}$, c) 5 nm-tick $Fe_{0.8}Pt_{0.2}$.

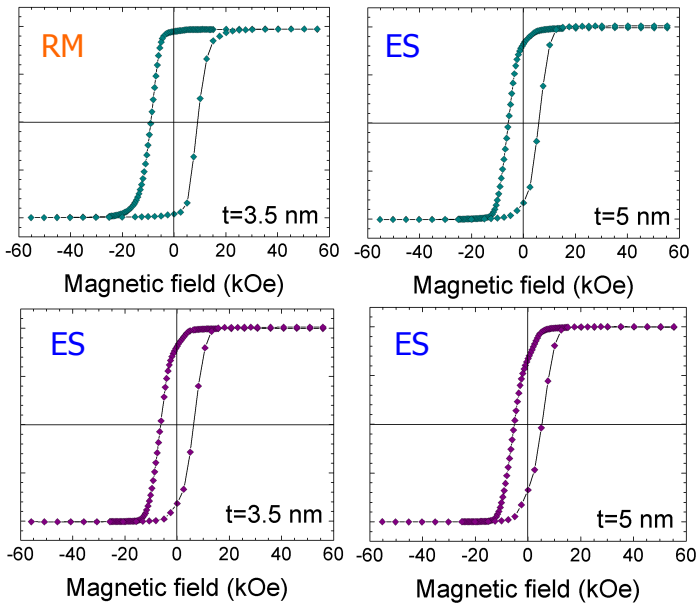

Figure 4.18: - Hysteresis loops measured by the Anomalous Hall Effect on samples grown on $SrTiO_3$. Top: $L1_0$-FePt/$Fe_{0.75}Pt_{0.25}$, bottom: $L1_0$-FePt/$Fe_{0.80}Pt_{0.20}$. The Fe_3Pt layer thickness is labeled.RM= rigid magnet regime; ES= exchange-spring regime

In conclusion, the magnetization reversal process has been fully investigated in the different magnetic regimes (Rigid Magnet and Exchange-Spring) in an attempt to demonstrate the strong and proper exchange coupling between bottom magnetic hard layer and top magnetic soft layer in FePt-based perpendicular recording media. A strong coercivity reduction with increasing Fe_3Pt thickness has been found in the bilayers grown on both substrates; the reduction is larger in the samples grown on $SrTiO_3$ and with higher Fe content in the soft phase (H_C/H_{Chard} down to 0.21).

4.4 Graded FePt media by ion irradiation.

Suess extended the concept of exchange spring media from bilayer structures to multilayer structures and demonstrated that coercive field reduction is proportional to 1 over number of layers and thermal stability of the media remains the same [45]. Thus, the coercive field reduces with the increase of number of layers. Extending this idea to a ideal stack with a infinite number of thin layers, in which anisotropy constant is gradually reduced, we get a graded media. This system represents another possible way to overcame the limits of magnetic recording media and It is expected to yield the largest reduction of the switching field with respect to multilayers systems. Moreover, in a graded system the coercive field is proportional to the gradient in the wall energy density and the energy barrier is equal to the energy of a domain wall in the hard storage layer [156]. This allows to tailor switching fields and energy barriers independently. Different ways have been exploited to control this anisotropy gradient, such as: growth temperature [157], composition gradients [158], post growth annealing and diffusion [159].

In our work, see in publication section [P-2], a novel procedure for the fabrication of anisotropy graded perpendicular media based on low energy (0.5-5 keV range), low dose (10^{13}-10^{15} ions/cm^2) and noble-gas ion irradiation has been used. Ion irradiation of FePt film with different thickness has been performed by a hot cathode Ar^+ sputtering gun operating at 5 keV, incidence angle 40° and 85° from sample normal, beam diameter approximately 10 mm at the S3-CNR laboratories in Modena. Our previous work [25] shows that the irradiation with Ga^+ions of $L1_0$-FePt thin film induce a complete transition from the ordered $L1_0$ to the disordered A1 phase, leading to a drastic decrease of the magnetic anisotropy and coercivity. Thus, exploiting the shorter Ar^+ ion

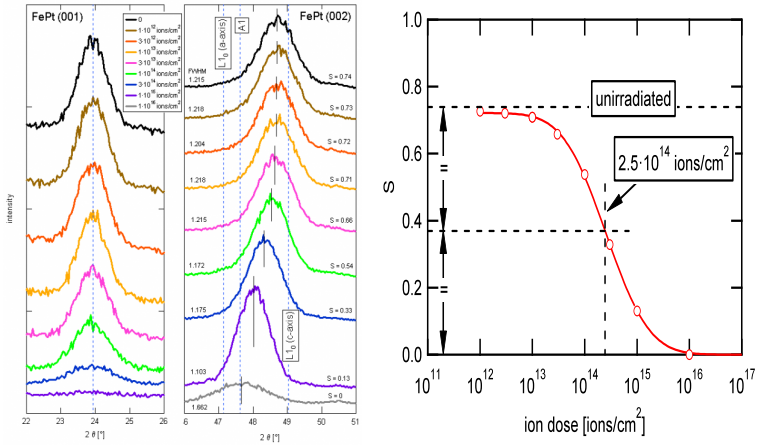

(a) (b)

Figure 4.19: a) XRD patterns of the FePt (001) chemical order superstructure, (left) and FePt (002) fundamental (right) peaks for a 10 nm film of FePt $L1_0$ for increasing irradiation doses of 5 keV Ar+ ions, (b) order parameter S of the 10 nm FePt film as a function of the irradiation dose, calculated from XRD spectra.

penetration depth into the film, it is possible to induce a controlled and graded structural transformation from ordered to disordered phases along the FePt film thickness by an appropriate choice of the ion beam parameters (i.e., ion energy and incidence angle). Thus, the spatial width of the transition region can be tuned in order to reduce the switching field.

In order to choose the suitable ion dose, a $L1_0$-FePt sample with thickness of 10 nm film has been irradiated with different ion doses and energies. Figure 4.19(b) shows the chemical order parameter S as a function of the irradiation dose for this sample as measured from the ratio of the (001) superstructure and (002) fundamental XRD peak ratio (Fig. 4.19(a)). For the unirradiated material the value of S is 0.74. Due to the large penetration depth of the X-rays, these structural data represent averaged values over the whole thickness of the film. Increasing irradiation dose (top to bottom of figure 4.19(a)) the (001) superstructure peak intensity decreases (left), while the (002) fundamental peak position shifts toward lower Bragg angle, indicating that the irradiated material progressively transitions from the $L1_0$ to the A1 crystal structure. Even if the partially disordered region is confined within the first 3-4 nm in depth, the (002) peak shows up as a single peak during the transition, that do not necessarily means

that the chemical disorder is uniformly distributed along the film whole thickness. The transition begins at $\approx 10^{13}$ ions/cm^2 and completes as the dose is increased to $\approx 10^{15}$ ions/cm^2 , indicating that ion irradiation is effective in reducing the value of S. At the highest dose (10^{16} ions/cm^2), i.e. one order of magnitude higher than the complete disordering dose, even the fundamental (002) peak is almost suppressed, indicating that significant film thinning took place due to the sputtering effect. Since the XRD

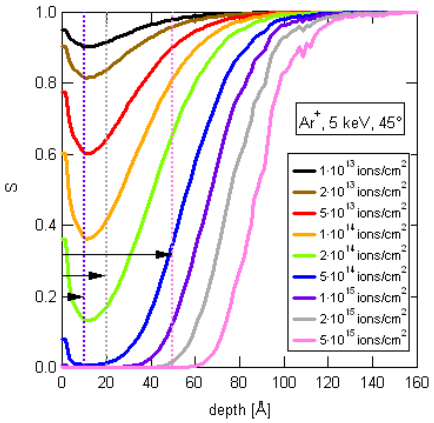

Figure 4.20: - Continuous lines: simulation of spatial distribution of the chemical ordering parameter for different ion doses in ions/cm^2 units; dashed line: vacancy production rate for Ar^+, 5 keV, 40° incidence angle on FePt.

measurements do not give information about in-depth distribution of chemical disorder because they are inherently integrated over the whole film thickness, more information has been obtained by a Monte Carlo simulation for transport of energetic ions in solids performed using SIMNRA software. Figure 4.20 shows the degree of chemical order S(z), at different irradiation doses, along FePt film thickness, which is calculated on the assumption that the effect of each atom vacancy induced by the ion irradiation is equivalent to a random swap between two atoms in the Fe and Pt sublattices. Moreover, the vertical dashed line in the figure represents the film erosion produced by 5 keV Ar^+ ion beam. Increasing the ion dose, S(z) reduces more quickly at depths where the vacancy production rate is larger, because the mixing effect is larger. At high doses, S(z) is zero in those regions, resulting in a quite defined front that moves deep in the film as the dose is increased and divides the region where S(z)$\approx$ 0 from that where S(z)$\approx$1. The comparison of the calculated and measured values of S(z) as a function of the ion dose are shown in the figure 4.21, with a fairly good agreement with the experimental data

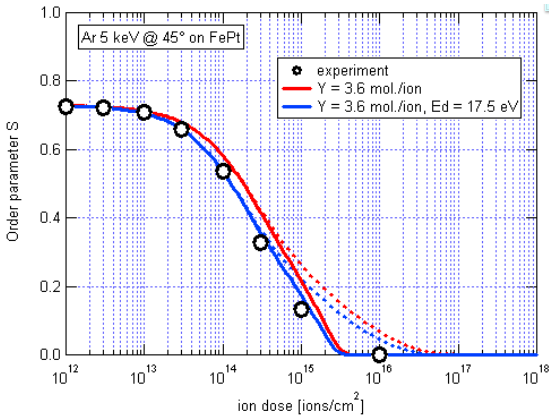

Figure 4.21: - Order parameter S of the 10 nm $L1_0$-FePt film as a function of the irradiation dose.Dot: experimental values; dashed lines (blue and red): simulated curve at different dislocation energy without erosion correction; continuos line (blue and red): simulated curve at different dislocation energy with erosion correction.

when the model takes into account also the film erosion. Simulation is also suitable to calculate thickness of the different magnetic phases in the graded system, values are resumed in table 4.2.

Since the magnetic anisotropy of $L1_0$-FePt is strictly related to the degree of chemical ordering and the relationship is approximately linear [25], figure 4.20 can also be assumed as a reasonable picture of the magnetic anisotropy depth profile induced by ion irradiation. For the optimal dose of 5×10^{14} ions/cm^2 three regions can be roughly defined in the film: a soft region that lies just below the film surface where S(z)$\approx$ 0, a hard region deep in the film where S(z)$\approx$1 and a graded region, where S(z) changes approximately linearly from 0 to 1.

In order to explore the effect of the ion irradiation on magnetic behavior of sample, four samples of different thickness have been irradiated at the optimal dose of 5×10^{14} ions/cm^2 at different angles obtaining different thickness for soft, graded and hard region.

FePt film with different thickness (10, 15 and 20 nm) have been grown on MgO substrate and characterized by AGFM measurements. The hysteresis loops of as-deposited samples (Fig. 4.22 (a), (b) , (c)), show a magnetic behavior typical of epitaxial $L1_0$-FePt films with easy magnetization axis oriented perpendicular to the film plane. The perpendicular coercive field ($\mu_0 H_c$), saturation magnetization (M_S) and remanence ratio ($M_R^{\parallel}//M_S$, where M_R is the in-plane remanence magnetization) are function of film

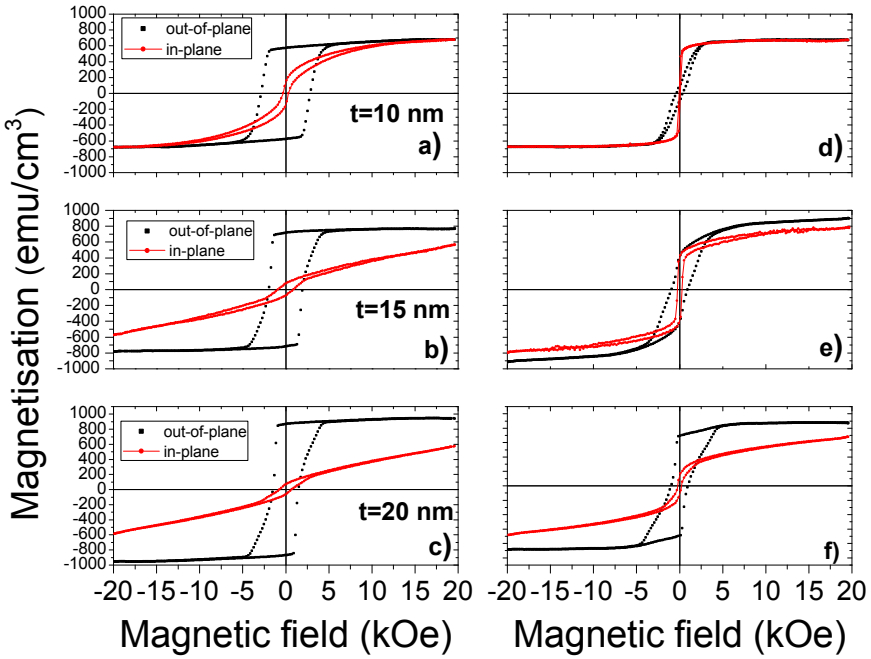

Figure 4.22: - Hysteresis loops of unirradiated $L1_0$-FePt film (left) and irradiated (right) with different thickness: (a) and (d) 10 nm; (b) and (e) 15; (c) and (f) 20 nm . Magnetic field is applied perpendicular to the film plane (dotted lines), and parallel to the film plane (dashed lines).

thickness. In particular, $\mu_0 H_c$ and $M_R^{\parallel}//M_S$ decrease with increasing the thickness, while M_S increases (see table 4.1). As the samples are irradiated, their magnetic

Table 4.1: Magnetic parameters of the unirradiated samples.

FePt thickness (nm)	Incidence angle	$\mu_0 H_c$ (kOe)	M_S (emu/cm^3)	$M_R^{\parallel}//M_S$
10	45	2.85 ±0.03	680 ± 30	0.2
15	45	1.96 ±0.02	760 ±40	0.1
20	45	1.48 ±0.01	940 ±50	0.09

Table 4.2: Thickness of the different S regions obtained by the simulation.

FePt thickness (nm)	Incidence angle	soft (nm)	graded (nm)	hard (nm)
10	45	2.9	5.6	1.5
15	45	2.9	5.6	6.5
15	85	0.9	5.0	9.1
20	45	2.9	5.6	11.5

properties are modified as a consequence of the magnetic softening of a part of the film, as reported in Table 4.3 and shown in figures 4.22 (d), (e), (f). This is mainly evident in the thinnest sample (10 nm) in which the irradiation induces disorder over most of the film thickness and therefore it induces a change in the direction of easy magnetization axis from perpendicular to parallel to the film plane. Thus, while M_S remains essentially unchanged (M_S =670 emu/cm^3), $\mu_0 H_C$ is reduced to 0.39 kOe. This low, but finite, perpendicular coercivity proves the presence of a residual ordered $L1_0$-phase in agreement with the irradiation model. By increasing the film thickness to 15 nm, the thickness of the residual $L1_0$-ordered layer increases to 6.5 nm (Table 3.1) and a positive nucleation field is observed (Fig. 4.22 (e)) suggesting the formation of a graded exchange material. The exchange coupling between the A1 and $L1_0$ fractions halves coercive field with respect to the as-deposited sample ($\mu_0 H_C$ reduces from 1.96 to 0.97 kOe), and increases the value of M_S (870 emu/cm^3), indicating that a composite graded material is obtained after irradiation. With further increase of the film thickness to 20 nm, the hard layer thickness becomes 11.5 nm and the graded part is just one quarter of the whole thickness. In this case, $\mu_0 H_C$ is reduced to 0.98 kOe and

M_S slightly reduces if compared to the as-deposited film (Fig. 4.22 (f)).

Furthermore, the sample with a thickness of 15 nm, which is the most promising, has

Table 4.3: Magnetic parameters of the irradiated samples.

FePt thickness (nm)	Incidence angle	$\mu_0 H_c$ (kOe)	M_S (emu/cm^3)	$M_R^{\parallel}//M_S$
10	45	0.39 ±0.04	670 ± 30	0.67
15	45	0.97 ±0.01	870 ±40	0.47
15	85	1.19 ±0.02	800 ±40	0.14
20	45	0.98 ±0.01	870 ±40	0.18

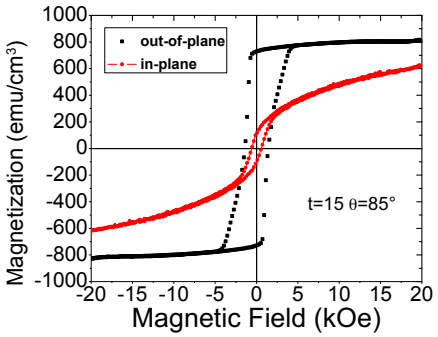

Figure 4.23: - Hysteresis loops of FePt with a thickness of 15 nm irradiated with an incident angle of 85°. Magnetic field is applied perpendicular to the film plane (dotted lines), and parallel to the film plane (red lines).

been chosen in order to exploit the capability to tune the magnetic properties. Starting from the optimized irradiation dose, the irradiation angle of 85° has been chosen as easy tuning parameter. At this irradiation angle a reduced effect on magnetic properties is shown. At grazing irradiation angle the change in the magnetic properties is less pronounced (see Table 4.3 and Fig. 4.23) with a reduction of $\mu_0 H_C$ to 1.19 kOe.

In order to better investigate the irradiation effect on the films of 15 and 20 nm, DCD, IRM and recoil curves have been measured on as-deposited and irradiated samples. As expected in a graded system, these samples show a reversible contribution in the magnetization reversal process (Fig. 4.24, 4.25). In the case of 15 nm-tick FePt that contribution is greater than 20 nm-tick FePt sample, leading to a reduction of 56% in the magnetization value between direct and remanence curves, see figure 4.24 (a) and (c). The reversible part of the magnetization reversal process has been identified

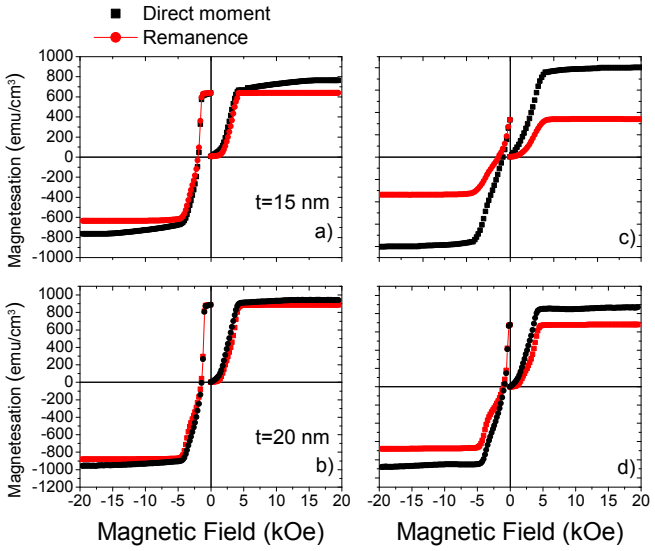

Figure 4.24: - IRM and DCD curves taken on FePt with thickness of 15 nm a) as-deposited , c) irradiated and with thickness of 20 nm b) as-deposited and d) irradiated with field applied perpendicular to the film plane. (dotted lines). Curves with solid dark dots correspond to the direct magnetization curve.

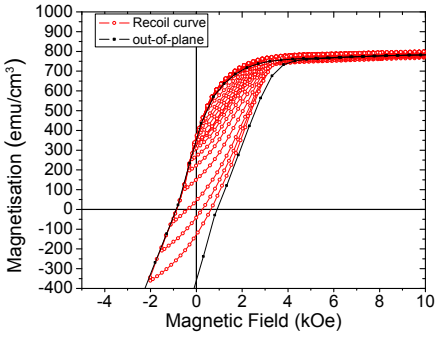

Figure 4.25: - Recoil curves taken on irradiated sample with thickness of 15 nm (red lines) and the out-of-plane hysteresis loop (black line).

in the range between 3 kOe and -3 kOe. The reversible contribution is smaller in the sample with thickness of 20 nm (Fig. 4.24 (d)), where only the 20% of magnetization value is due to the reversible process.

It has been found that different incident angles permit to tune the magnetic properties, in particular H_C value, though keeping the easy magnetization axis perpendicular to the film plane. Moreover, lower and upper limits for soft, graded and hard layer thickness can be defined in order to achieve optimal magnetic characteristics for magnetic recording purpose. In particular, for the soft layer thickness (t_s) should be $14\% \leq t_s \leq 20\%$ of the whole thickness value (t_{tot}), the graded layer thickness (t_g) should be $28\%\ _{tot} \leq t_g \leq 36\%\ _{tot}$ and the hard layer thickness (t_h) should be $43\%\ _{tot} \leq t_h \leq 57\%\ _{tot}$.

In order to understand the effect on morphology and quality of the sample surface

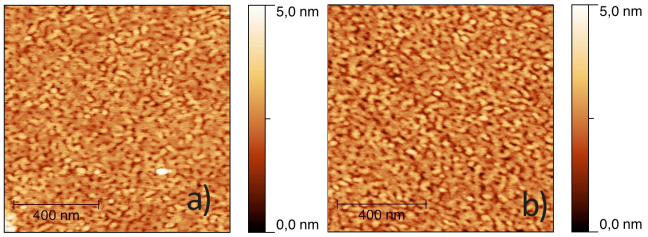

Figure 4.26: - AFM image (1 μm $\times$ 1 μm) taken on FePt with thickness of 15 nm a) as-deposited, b) after irradiation.

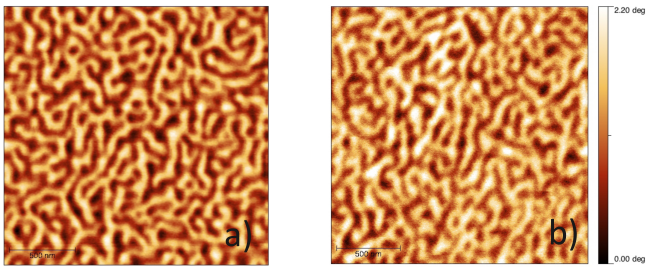

Figure 4.27: - MFM image (2 μm $\times$ 2 μm) taken on FePt with thickness of 15 nm a) as-deposited, b) after irradiation.

due to the ions irradiation, AFM and MFM images (Fig. 4.26, 4.27) have been taken on the samples with thickness of 15 nm as-grown and after irradiation. The surface morphology appears not damaged by ions, the RMS roughness is slightly increased from 0.32 nm (as-grown) to 0.52 nm (irradiated) and the morphology pattern is the

same of as-grown sample. Also the magnetic domains pattern is not influenced by ion irradiation, since domain shape and size remain unchanged before and after the irradiation. Thus, the ions irradiation with a suitable dose does not damage FePt surface. This is an advantage for magnetic recording media.
HR-TEM images confirm the gradual chemical disorder induced by ion irradiation along

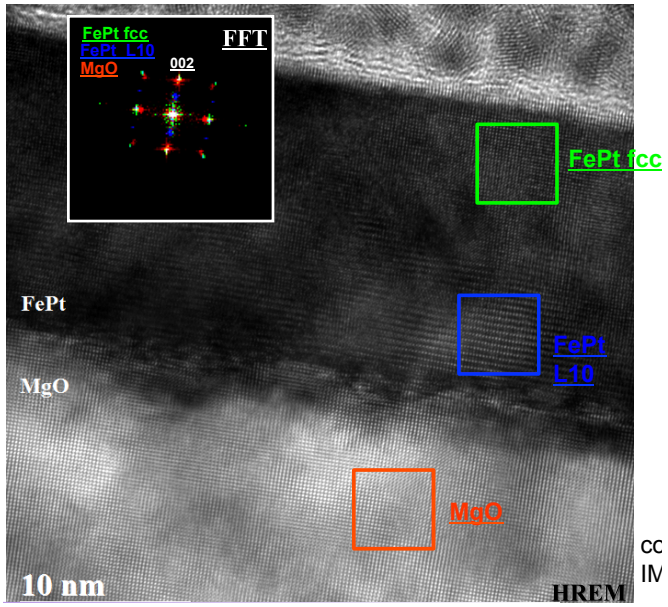

Figure 4.28: - HR-TEM cross section of irradiated FePt film with a thickness of 20 nm. Red square: MgO area; blue square: $L1_0$-FePt area; green square: A1-FePt area. In the inset FFT of the three crystalline structure.

the FePt film thickness. In particular, the figure 4.28 shows the change in the alternated stacking of single Fe and Pt elemental planes, typical of $L1_0$-FePt crystalline structure, towards a random distribution of Fe and Pt atoms, typical of A1-FePt crystalline structure. This transformation starts few atomic layers above the substrate interface and continues gradually closer to the film surface.
In conclusion, exchange-coupled composite media with continuously graded perpendicular anisotropy have been fabricated by low energy ion irradiation, at optimized dose, of chemically ordered FePt $L1_0$ thin films. A simple mixing model based on Monte Carlo simulations allowed us to design the spatial distribution of the chemical disorder. The magnetic properties of the irradiated material can be optimized by changing few significant ion beam parameters, e.g. ion energy, ion dose and incidence angle, parameters that are largely uncritical and tightly controllable and reproducible in different

production systems, making this technique easily scalable to large area samples.

5

FePt-based Magnetic Tunnel Junctions.

In the next decade, the current semiconductor technology based on the electron charge (i.e., CMOS technology) is predicted to still play a leading role in integrated circuit fabrication, in spite of more and more physical obstacles and performance limits discovered. The magnetic tunnel junction (MTJ) (see section 1.7.2) is one of the candidates with higher chance to replace the semiconductor based devices [5]. It is non-volatile and its typical electrical resistance value is compatible with MOS transistors, which allows it to be easily integrated with CMOS circuits. These are advantageous factors that make easier the exploiting of the actual CMOS manufacture technology to produce the future spintronics devices. Based on MTJ cells and CMOS technology, the first commercial magnetic RAM (MRAM) was successfully produced in 2006 by Freescale company. Two important discoveries for MTJ devices have led to the reconsideration of this technology as more suitable and closer to the mass commercial applications than other nanodevices. Firstly, the use of MgO as the oxide barrier inside the MTJ, which greatly increases the resistance ratio between the two magnetic states and improves its sensing stability and speed. Secondly, the spin transfer torque (STT) (see section 1.7.2) has allowed a significant reduction of the switching energy and data disturbance when compared with the conventional field-induced switching approach. In this section the results obtained on the fabrication and characterization of MTJs grown on MgO substrate will be described, with the new stacking structure Fe_3O_4/MgO/$L1_0$-FePt.

5.1 FePt-based spintronic devices: state of the art.

One of the problems found in the scaling down process of nanometer-scale magnetic media and devices is the thermal fluctuation of magnetization. $L1_0$-FePt alloy is a candidate ferromagnetic material, which could allow to overcome this problem because its high magnetocrystalline anisotropy energy [8]. However tunnel magnetoresistance (TMR) has been studied in MTJ based on $L1_0$-FePt alloys by few authors [8, 160, 161, 162]. The employment of $L1_0$-FePt electrodes could be useful in perpendicularly magnetized magnetic tunnel junctions (P-MTJs), which have a potential technological application as a new structure of spin-electronic devices because they have an advantage in large-scale integration due to a small aspect ratio [163, 164, 165]. Moreover, the introduction of high anisotropy materials pushes down the superparamagnetic limit.
A promising result has been obtained by Yoshikawa *et al.* [162] on a MgO-based MTJ device with perpendicular magnetic and $L1_0$-FePt as electrodes, a large TMR ratio over 100% at room temperature gas been measured. The development of P-MTJs has been driven by the STT-type devices, because they have the potential to reduce the critical current density of the STT switching, while maintaining a high thermal stability and size reduction [9, 166, 167, 168].

5.2 The choice of MgO barrier

The functional property of a MTJ device is the tunnel magnetoresistance (TMR), due to spin-dependent electron tunneling process. The MTJs with an amorphous aluminum oxide (AlO) tunnel barrier exhibit magnetoresistance (MR) ratios up to about 70% at room temperature (RT) due to the incoherent tunneling of polarized electrons through the amorphous barrier, but MR ratios significantly higher than 70% are needed for the next generation spintronic devices. In 2001 first-principle theories predicted that the MR ratios of epitaxial Fe/MgO/Fe MTJs with a crystalline MgO (100) barrier would be over 1000% because of the coherent tunneling of fully spin-polarized electrons through $\triangle_1$ band. This huge TMR effect in MgO-based MTJs is now called the giant TMR effect and is of great importance not only for device applications but also for clarifying the physics of spin-dependent tunneling. A clear explanation of this phenomenon was given by Yuasa [169].
Coherent and incoherent tunneling are illustrated schematically in figure 5.1. In the

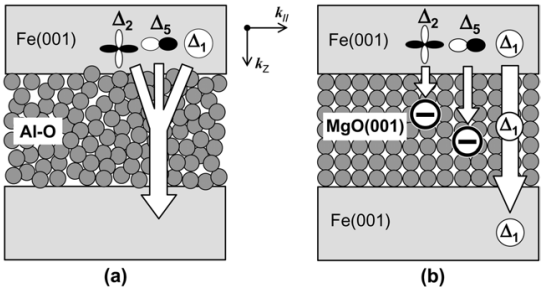

Figure 5.1: - Schematic illustrations of electron tunneling through (a) an amorphous Al-O barrier and (b) a crystalline MgO (100) barrier taken by [169].

case of ideal coherent tunneling, Fe $\triangle_1$ states are theoretically expected to dominantly tunnel through the MgO (100) barrier because the $k_{\|}$=0 direction ([0 0 1] direction in this case) is that with the highest tunneling probability and matchs with three kinds of evanescent states (tunneling states) in the band gap of MgO(100), these are: $\triangle_1$, $\triangle_5$ and $\triangle_{2'}$. When the orbital symmetries of tunneling wave functions are conserved,

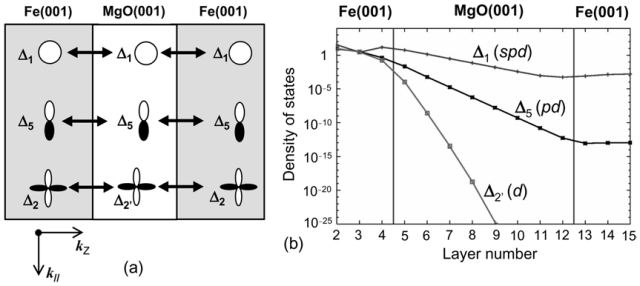

Figure 5.2: - (a) Coupling of wave functions between the Bloch states in Fe and the evanescent states in MgO for the $k_{\|}$=0 direction. (b) Tunneling DOS of majority-spin states for $k_{\|}$=0 in Fe(0 0 1)/MgO(100)(8 ML)/Fe(0 0 1) with parallel magnetic state taken by [170].

Fe $\triangle_1$ Bloch states couple with MgO $\triangle_1$ evanescent states, as shown in figure 5.2(a). Of these MgO states, the $\triangle_1$ evanescent states have the slowest decay (i.e. the longest decay length). The dominant tunneling channel for the parallel magnetic state is Fe $\triangle_1$ $\leftrightarrow$ MgO $\triangle_1$ $\leftrightarrow$ Fe $\triangle_1$. The net spin polarization of Fe is small because both majority-spin and minority-spin bands have many states at Fermi level (E_F), but the Fe $\triangle_1$ band is fully spin-polarized at E_F (P = 1). A very large TMR effect in the epitaxial Fe(001)/MgO(100)/Fe(001) MTJ is therefore expected when $\triangle_1$ electrons dominantly tunnel. It should also be noted that a finite tunneling current flows even for antiparal-

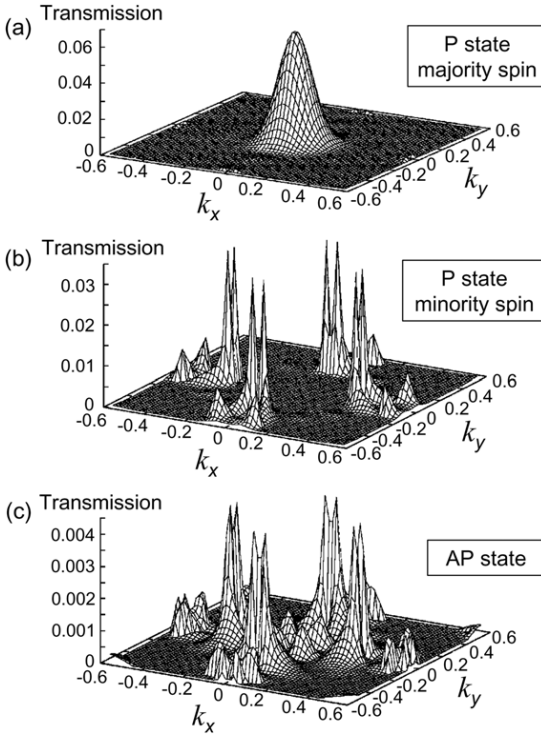

Figure 5.3: - Tunneling probability in a Fe(001)/MgO(100)(4 ML)/ Fe(001) MTJ as a function of k_x and k_y wave vectors taken from [170]. (a) Majority-spin conductance in the parallel magnetic state (P state), (b) minority-spin conductance in the P state, (c) conductance in the antiparallel magnetic state (AP state). After [169]

lel magnetic states. Tunneling probability as a function of $k_{\parallel}$ wave vectors (k_x and k_y) is shown in figure 5.3. For the majority-spin conductance in the parallel magnetic state (P state) (Fig. 5.3(a)), tunneling takes place dominantly at $k_{\parallel}$=0 because of the coherent tunneling of majority-spin $\triangle_1$ states. For the minority-spin conductance in the P state (Fig. 5.3(b)) and the conductance in antiparallel magnetic state (AP state) (Fig. 5.3(c)), spikes of tunneling probability appear at finite $k_{\parallel}$ points called hot spots. This hot-spot tunneling is resonant tunneling between interface resonant states [169, 170]. Although a finite tunneling current flows in the AP state, the tunneling conductance in the P state is much larger than that in the AP state, making the MR ratio very high. It should be noted that the $\triangle_1$ Bloch states are highly spin-polarized not only in bcc Fe(001) but also in many other bcc ferromagnetic metals and alloys based on Fe and Co (e.g. bcc Fe-Co, bcc CoFeB and some of the Heusler alloys). A very large TMR should be characteristic of MTJs with 3d-ferromagnetic alloy electrodes with bcc (001) structure based on Fe and Co. Note also that very large TMR is theoretically expected not only for the MgO(100) barrier, but also for other crystalline tunnel barriers such as $SrTiO_3$ (100) [171].

A tunneling magnetoresistance ratio of 18% has been observed at room temperature in the MTJs with $L1_0$-FePt electrode and an amorphous Al-O tunnel barrier [160]. The spin polarization in $L1_0$-FePt, calculated from the first principles band structure at the Fermi level, is 72% and 45% for s- and d-electrons, respectively [8]. According to the Jullier model (see section 1.7.2), the uppermost TMR ratio expected is about 220% for FePt/Al-O/FePt MTJs. Taking into account the TMR over 400% reached in Fe-based MTJ employing MgO barrier, it is worthwhile to investigate the possibility to improve the TMR ratio by using the MgO barrier also in FePt-based MTJs. Taniguchi *et al.* [172] published an important theoretical work on this argument. It was found that the totally symmetric $\triangle_1$-band in FePt crosses the Fermi level both in the majority- and minority-spin states, in contrast to ferromagnetic transition metals such as bcc Fe. Moreover, the minority-spin $\triangle_1$-band is predominantly composed of Fe and Pt d($3z^2$-r^2) orbital at the Fermi level, while the majority-spin $\triangle_1$-band is mainly constructed from Fe and Pt p(z)-orbitals. As shown above, the $\triangle_1$-band electrons predominantly transmit through the MgO barrier, thus, huge TMR ratios cannot be expected in the FePt/MgO/FePt(001) MTJs from the viewpoint of symmetry compatibility between the electronic band-structure in the bulk FePt and MgO. However, it has been shown

that when FePt interface with MgO barrier is Fe-terminated, it is more stable than the Pt-terminated one, due to the formation of Fe-O bonds. In this case, it is noted that the tunneling transmittance via the minority-spin channel is almost two orders of magnitude smaller than that via the majority-spin channel at the Fermi level showing a sharp peak around the center of the two-dimensional (2-D) Brillouin zone, typical of coherent tunneling transmittance of the $\triangle_1$-band electrons. Thus, the Fe-terminated interface is more desirable for obtaining larger TMR ratio in the FePt/MgO/FePt(001) MTJs. The Fe-terminated FePt/MgO(100) interface is found to be favorable energetically and thus it can be realized for appropriate growth conditions with the aim to improve the efficiency of spin injection from the FePt/MgO(100) junctions, since it possesses spin-filtering functionality originated from the interfacial scattering of tunneling electrons.

5.3 FePt-based MTJs.

Four different heterostructures have been grown on MgO substrate with the optimized growth parameters reported in section 3.2.1 and 3.3, exploiting the experience of INA institute to grown Fe_3O_4 and MgO films by PLD technique and the ability to grow highly ordered FePt films by RF sputtering technique at IMEM institute. Samples layer thickness are resumed in table 5.1. The structural characterization on the

Table 5.1: Heterostructure layers thickness

Sample number	Fe_3O_4 (nm)	MgO (nm)	FePt (nm)
1	38	0.72	10
2	38	3.36	15
3	27	1.59	10
4	37	3	10

samples by XRD show the (002) reflection from magnetite, (001) and (002) reflections from FePt and no other crystalline reflections in the XRD pattern. In figure 5.4 a spectra of sample number 2 is reported as an example. The θ-2θ scan points out the good crystalline quality of bottom and top layers and, in particular, the formation of ordered FePt in the $L1_0$-phase grown on top of the barrier layer. It is possible to estimate the FePt degree of order to be in the range from 0.67 to 0.75, with the

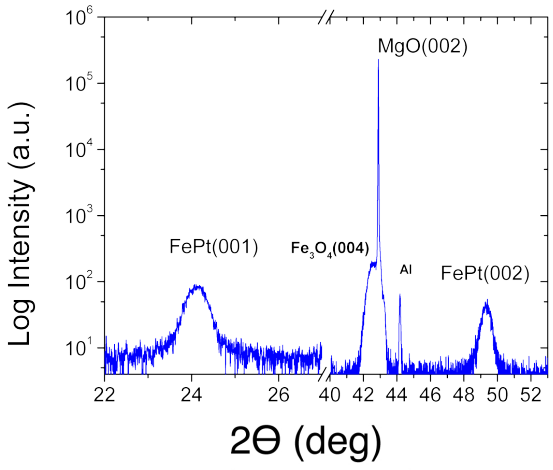

Figure 5.4: - θ-2θ scan from a Fe_3O_4/MgO/FePt heterostructure and sample number 2. Crystallographic peaks are labeled in the figure

highest degree corresponding with the thickest FePt layer (15 nm). Moreover, magnetic properties have been measured by VSM with applied field perpendicular to the film plane up to 20 kOe (Fig. 5.5).This is the field direction that will be used to measure TMR ratio in magneto transport measurements. The hysteresis loop shows a mixed behavior associated to the continuos rotation of the magnetization in the Fe_3O_4 layer (with the easy magnetization axis parallel to the film plane) and the sharp inversion of the magnetization at the coercive field in the FePt layer (with easy magnetization axis perpendicular to the film plane). Thus, a certain degree of exchange coupling can not be excluded looking at the loops shape of the heterostructure.

5.3.1 MTJ microfabrication

At INESC-MN in Lisbon, 35 MTJs devices have been microfabricated on every sample following the steps described in section number 2.5 and covered by TiW(N) metallization layer. They are arranged in 5 rows and 7 columns on 4×4 mm^2 area and along each row the junction area increases starting from 8×36 μm^2 to 32×36 μm^2 with steps of 4 μm (six total steps). In order to allow four-probe electrical characterization, each electrode is connected to 2 pads area. The surface of the samples has been analyzed by an optical microscope at the INA laboratories after microfabrication. At low magnification, most of the MTJ features are well replicated on the sample surface by optical lithography (Fig. 5.6). How it is possible to see in figure 5.7 lift-off process has not

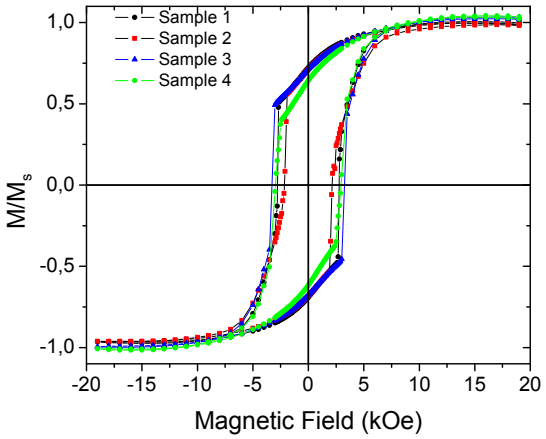

Figure 5.5: - Hysteresis loops of samples normalized to the saturation magnetic moment with applied field perpendicular to the film plane.

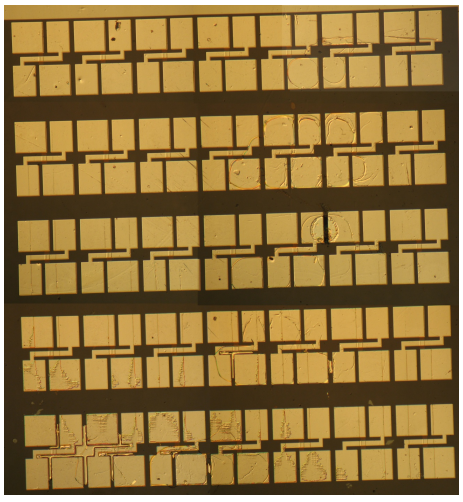

Figure 5.6: Surface of the lithography area after microfabrication.

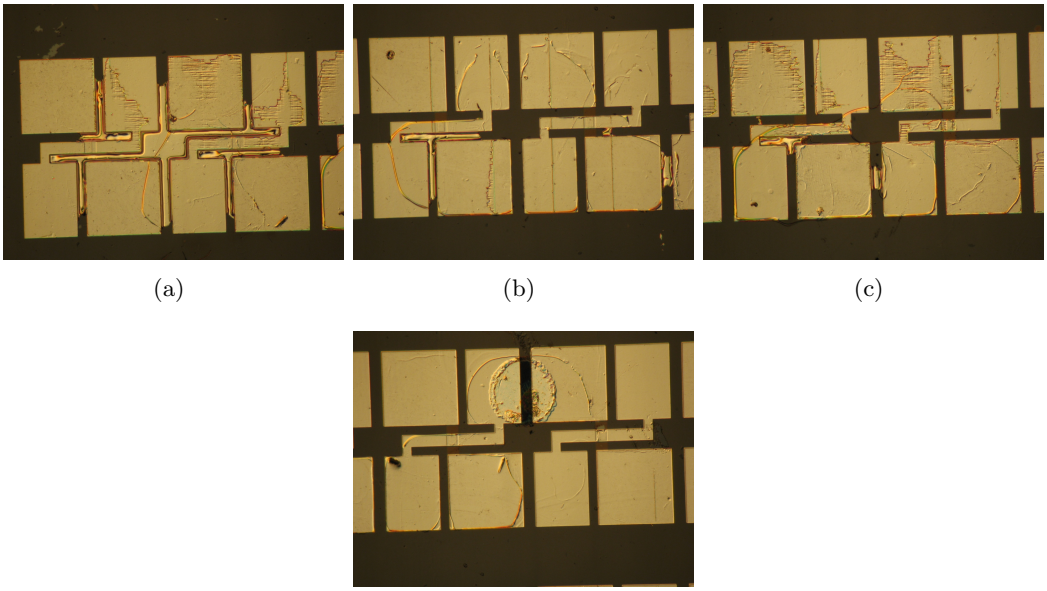

(a) (b) (c)

(d)

Figure 5.7: Optical microscope images taken at lower scale of microfrabricated sample. Defects are visible as a) and b) not etched material c) and d) electrode erosion.

been completely clear and sharp. In fact, there are some imperfections on the surface of device that are clearly visible at higher magnification. These can occur as non-etched material between pads (Fig.s 5.7(a), 5.7(b)) or electrodes damaging on surface (Fig. 5.7(c), 5.7(d)). However, the number of devices allow to characterize most of microfrabricated samples as a function of junction area.

5.3.2 Electrical characterization

At the beginning, current vs. voltage measurements at zero applied magnetic field on selected devices have been done to estimate the Resistance per Area (RxA) values and to test electrical transport. Values are reported in table 5.2.

These measurements (Fig. 5.10, 5.8 and 5.9) show an ohmic behavior and linear slope in I/V curve characterized by not constant value of RxA. This indicates that probably during microfabrication process electrode/barrier and/or top electrodes surface have been subjected to damage or degrade of electrical conduction properties. In fact, what is expected from this kind of measurement on well-fabricated device is a tunneling conduction behavior, which is characterized by a non linear slope for low value of

Table 5.2: RxA and resistance values for junction area on different samples. Four-probes measurements have been done on sample number 1 and 2, while two-probes on sample 3

Junction area (μm^2)	RxA ($\Omega\mu m^2$)	Resistance (Ω)
Sample number:		1
8x36	4.6×10^4	162
12x36	1.5×10^5	360
20x36	2.74×10^5	371
28x36	3.22×10^4	160
Sample number:		2
8x36	$4.5\text{x}10^4$	156
12x36	$4.57\text{x}10^4$	106
32x36	$1.8\text{x}10^5$	160
Sample numer:		3
8x36	3.86×10^6	13×10^3
24x36	9.1×10^6	10.5×10^3
32x36	1.17×10^7	10×10^3

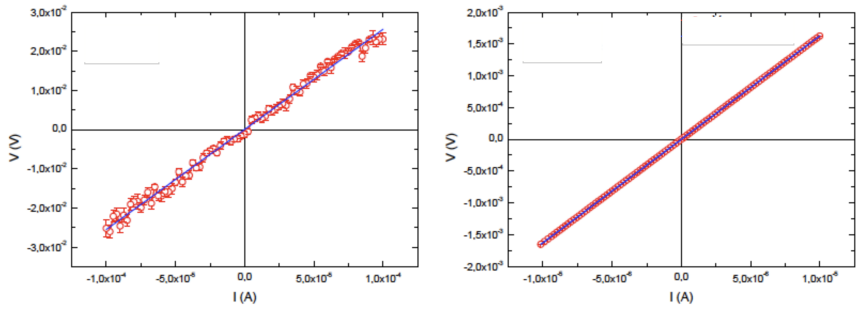

(a) (b)

Figure 5.8: I-V measurements for two different devices a) 8x32 μm^2 junction area and b) 28x36 μm^2 junction area of the sample number 1 at RT

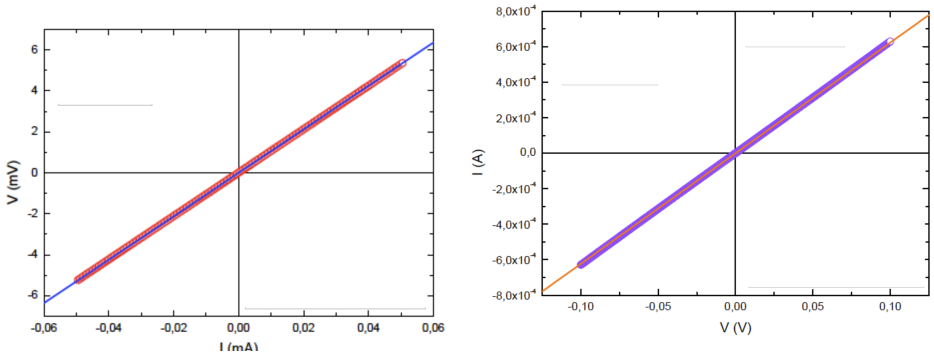

(a) (b)

Figure 5.9: I-V measurements for two different devices a) 12x32 μm^2 junction area and b) 32x36 μm^2 junction area of the sample number 2 at RT

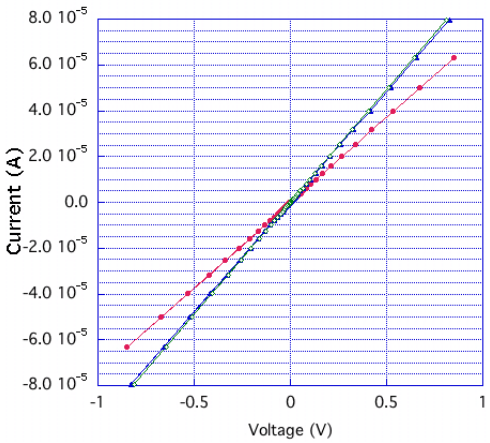

Figure 5.10: I-V measurements for different devices on the sample 3

applied voltage. Anyway, this conduction behavior may be present, but at the lowest voltage (very close to zero) and generates a signal too low to be discriminated between electrical noise by the instrument.

5.3.3 Electrodes magnetoresistance

The magnetoresistance of the single electrode (i.e., Fe_3O_4 and FePt) have been studied before TMR measurements on heterostructures. Magneto resistance ratio has been calculated as

$$MR = \frac{(R_h - R_c)}{R_c} \times 100 \tag{5.1}$$

,where R_c is measured resistance at coercive field.

For magnetite electrodes we have found similar result to those reported in [173], see figure 3.26. For the magnetite films MR effect is normal (negative), that is resistance is lower at higher applied field, and arises from misaligned magnetization in adjacent ferromagnetic grains (APBs). In our case, the magnetic field was applied along the film plane and the value calculated is about 2% that increases with increasing film thickness.

In the case of FePt electrode, magnetoresistance has been measured on 15 nm thin

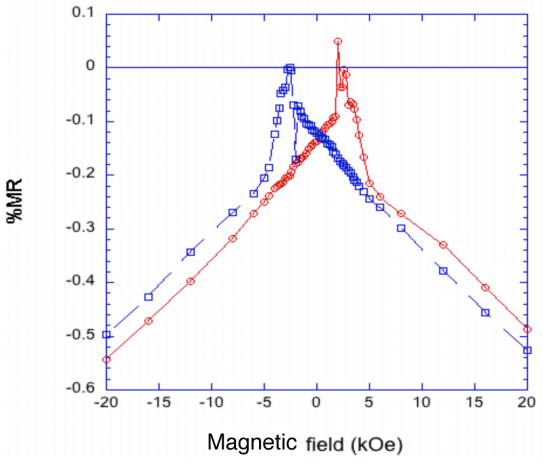

Figure 5.11: - 15nm FePt MR. Red curve (-○-): from positive saturation to negative saturation, blue curve (-□-): return from negative saturation to positive saturation.

film, with magnetic field perpendicular to the film plane. As showed in figure 5.11, FePt MR is normal and the value is 0.5% at RT. The magnetoresistance value for FePt film is related to the crystal order (S), and different concurrent causes can drive MR

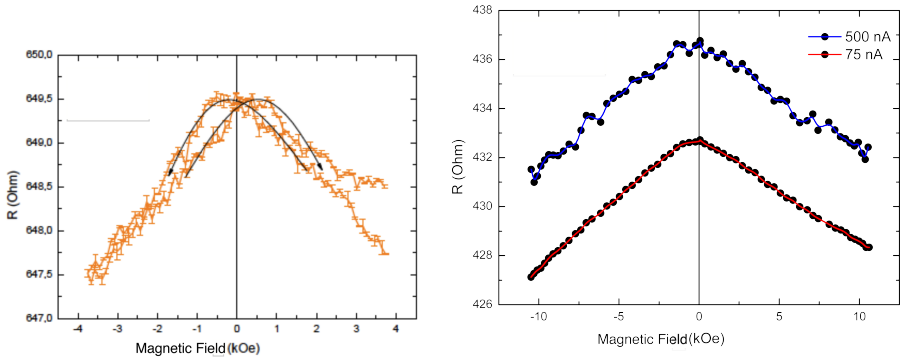

(a) (b)

Figure 5.12: TMR on a) sample number 1 on device with 20x36 μm^2 junction area and b) sample number 2, on device with 32x36 μm^2 junction area. In this latter case with two different applied current.

in FePt. In particular, at lower magnetic field the domain wall resistance (DWR) is predominant and can be the cause of the two peaks at critical field in figure 5.11, hence at higher field magnon magneto resistance (MMR) plays an important role contrasting MR saturation [174]. This effect is probably responsible for the linear slope as shown in figure 5.11 at higher field.

5.3.4 Tunnel magnetoresistance measurements

After measuring MR of single thin film electrodes, TMR has been measured on selected devices. Electrical resistance variations have been measured as a function of magnetic applied field, from positive to negative values and viceversa, exchanging the injection current direction between top and bottom layers.

Samples number 1 and 2 have been measured at INA institute with applied field perpendicular to the film plane up to 10 kOe and applied electrical current of 0.075 and 0.5 mA, injected parallel to the magnetic field direction. To reduce the thermal noise and/or drift, measurements have been done at low temperature (160 K). Anyway, a normal TMR effects has been found, shown in figure 5.12, with a peak corresponding to zero applied field. The results are comparable with those of the magnetite film (Fig. 3.26), thus Fe_3O_4 magnetoresistance contribution is dominant. The calculated values of MR on these tested devices are in the range of 0.4% to 1.3%, and no dependence from barrier or electrodes thickness has been found.

Measurements on sample 3 and 4 have been done at IMEM on devices with 8x36 μm^2 and 28x36 μm^2 junctions. TMR has been measured at room temperature with applied magnetic field up to 20 kOe and electrical current of 1 mA, with the same directions of applied field and current described above . Measurements on sample number 4, on device with a junction area of 8x36μm^2, are shown in figure 5.13. TMR effect is

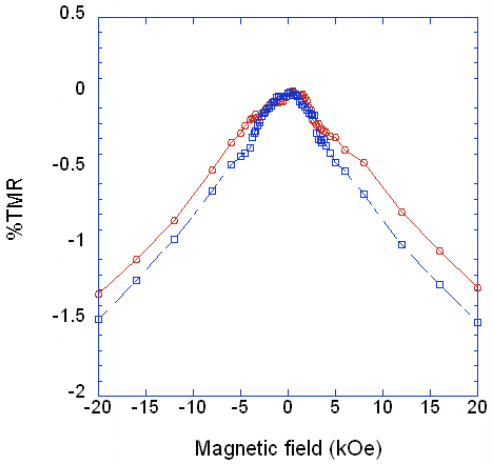

Figure 5.13: - TMR measurement on 8x36μm^2 junction area device on sample number 4. Applied current of 1 mA: red curve (-○-) from +20 kOe to -20 kOe; blue (-□-) from -20 kOe to +20 kO.

normal and absolute value is 1.5%, with a peak corresponding to zero applied field. Looking carefully at the figure 5.13, when magnetic field value is about 5 kOe a small slope variation of the curve is present, this can be an effect correlated with the critical field for magnetization reversal of the whole heterostructures. Also this sample shows a TMR effect similar to what has been found on sample number 2 and thus, probably related to the Fe_3O_4 magnetoresistance.

A completely different result has been obtained on sample number 3. In particular, measurements have been done on the device with junction area of 28x36μm^2 (Fig. 5.14), and show an inverse TMR effect with a value of 0.4%. Two peaks are present at the applied magnetic field corresponding to heterostructure critical fields (see figure 5.5).

Furthermore, TMR of the same devices on samples numbers 3 and 4 have been measured with applied field parallel to the sample surface up to 10 kOe (Fig. 5.15). In this geometry it possible to assume that FePt electrode magnetization is pinned along

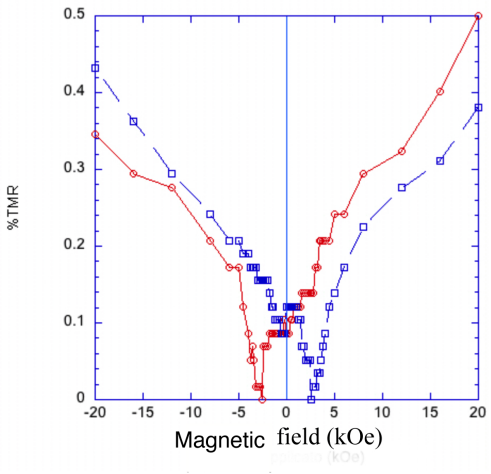

Figure 5.14: - TMR measurement on 28x36μm^2 junction area device on sample number 3. Applied current of 1 mA: red curve (-○-) from +20 kOe to -20 kOe; blue (-□-) from -20 kOe to +20 kO.

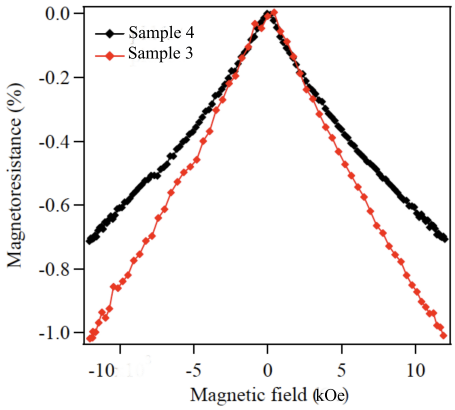

Figure 5.15: - TMR measurements on sample number 3 and 4 with applied field along film surface, courtesy of Federico Spizzo-University of Ferrara.

an hard magnetization direction, and the magnetization of Fe_3O_4 layer is free to move, following the hysteresis loop in figure . The result found in this geometry, on both samples, is similar to that obtained in the previous sample, where the only contribution to normal TMR probably comes from magnetite electrode.

5.3.5 TEM analysis on MTJ devices

With the objective to understand the electrode/barrier interface quality, a sample similar to sample number 3 (i.e., MgO (001) // (42.9 nm)Fe_3O_4 / (1.3 nm) MgO / (17.4 nm) FePt) and grown in the same way has been studied by HR-TEM.

Magnetite layer is characterized by a main set of fringes at 2.98 $\AA$ corresponding to

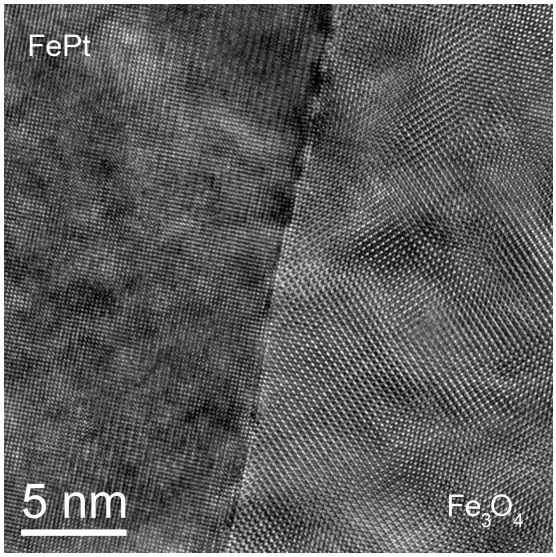

Figure 5.16: - HR-TEM image taken on sample similar to MgO (001) // (42.9 nm)Fe_3O_4 / (1.3 nm) MgO / (17.4 nm) FePt. Image courtesy of César Magén (INA-Zaragoza)

the (220) planes at 45° with respect to the interface when it is observed in the (001) zone axis. MgO thin layer should give a square lattice of 2.1 $\AA$ fringes of (200) planes parallel and perpendicular to the interfaces, but it is nearly imperceptible in most parts of the sample. For example, in figure 5.16 the superstructure of Fe and Pt alternating elemental layers, typically of $L1_0$-FePt, extends right to the Fe_3O_4 layer. Thus, barrier does not look like a neat continuous MgO layer. In addition, the high roughness at magnetite interface is evident in figure 5.17. These features at the electrode/barrier

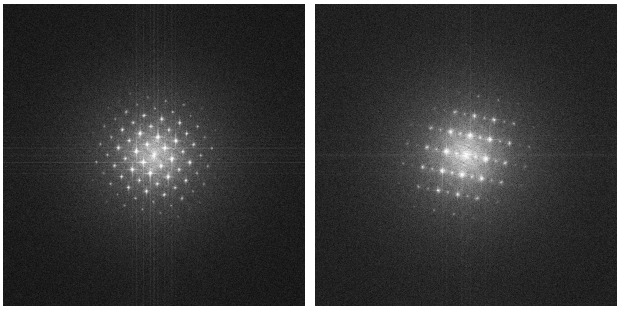

(a) (b)

Figure 5.17: a) FFt of FePt. First set of spots at 0.193 nm and the second set of spots (strong, at 90 of the weak ones) at 0.377 nm. b) FFt of magnetite. The first set of spots (220) at 0.295 nm and the second at 0.298 nm. Images courtesy of César Magén (INA-Zaragoza).

interfaces, easily present in studied samples, lead to the formation of pinholes and, thus, degrade the tunneling conductivity and TMR value.

5.3.6 Conclusions

The only measurement that indicates a possible inverse TMR effect has been found in sample number 3 at room temperature. Its value is low and two peaks are present at applied field equal to H_c value (Fig. 5.14). This effect is closely related to the Fe_3O_4/MgO barrier, as shown in the literature [175], and can be measured only in presence of an inverse TMR effect. Understanding these measurements involves different aspects [169, 170, 176, 177]:

- TMR is strongly sensitive to the electrode/barrier interface quality, in particular the density of defects, which is mainly affected by growth parameters (i.g.,temperature, annealing). In addition, the interface quality influences the matching between electron conduction band between electrodes and barrier layers.

- The MgO barrier thickness affects the spin transmission through the barrier. In particular, other authors found that in Fe/MgO-based devices TMR is sensitive to barrier thickness:

- with thick barrier (t_{MgO} ≥1.8 nm) transmission by majority spin band is favored through the barrier due to Bloch states conduction;
- with thin barrier, band transmission by minority spin is favored due to the formation of resonance states at both electrode/barrier interfaces.

We think that, MR effects of FePt and Fe_3O_4 electrodes are comparable with TMR effect. The low absolute value (≈ 3%, in the best case) can be considered as a possible consequence of the poor quality of Fe_3O_4/MgO interface or a complete lack of TMR effects. Thus, the resulting magnetoresistance is affected by electrode MR contributions whose values are a function of layer thickness and it is strongly related to barrier thickness. In the case of thicker barrier, TMR contribution is small and MR dominates giving rise to normal magnetoresistance (MR > TMR) (fig. 5.12(b), 5.13). In the case of thinner barrier, TMR is larger and a small inverse effect is measured (MR <TMR) (fig. 5.14). In sample number 1, the thinnest barrier is not a continuous layer and in some point the two electrodes are in contact, thus the inverse TMR effect is canceled. It is quite clear that the lithography process has to be improved to reach an optimal degree of quality for this type of MTJ microfabrication, since the lithography process is not optimized for this kind of MTJ and that may cause the formation of conduction channel trough and outside the barrier. For example, residual metallic material, non-etched, can keep in contact the two electrodes. The latter is related to the difficulties found in a sharp and clear FePt etching process. Moreover, in some case has been found an electrical contact between the electrodes due to pin-holes trough the barrier. On the other side, the growth process should be improved to avoid mixing at the electrode/barrier interface and reducing the roughness, on the basis of TEM analysis (Fig. 5.16). Another possibility is that electrodes are perforated by applied current, but this hypothesis have to be confirmed. Moreover, the competition between metallic transport through possible pinholes channels and tunneling transport through the barrier should be considered. A next step will be the completion of TMR measurement on every MTJ devices in order to obtain a complete scenario.
Finally, some improvement of the growth conditions have to take into account to ease microfabrication process, such as:

- complete heterostructures should be grown in the same chamber, avoiding exposure to atmosphere;
- extra buffer layer under magnetite electrode;
- capping layer (Au or Ta);
- samples have to be grown on bigger substrate.

The thickness optimization in these devices could make them of interest for the employment as magnetic spin-torque devices, since results are not as promising as magnetic tunnel junctions, so spin-torque measurements could be attractive.

6

Conclusion

This study is focused on the role of FePt alloy as a promising material in applications such as magnetic recording media and spintronic devices. The key property of this material, in $L1_0$-phase, is the high perpendicular magnetic anisotropy that has been achieved after the optimization of growth conditions. Since in nanometer scale systems the film morphology (i.e., continuous or island pattern) plays an important role in the final magnetic behavior, also the roughness and interface quality have been taken into account.

FePt thin films, with different thicknesses from 2 nm to 15 nm, have been grown on commonly used MgO substrate, with higher lattice misfit (8.3%), and on less investigated $SrTiO_3$ (STO) substrate, with lower misfit (1.5%). Overall, the possibility to obtain epitaxial (001) $L1_0$-phase films on both substrates, with tailored magnetic and morphological properties, have been demonstrated. Film morphology has been changed from continuous to island-like pattern by a control of the growth parameters, keeping low RMS roughness and reaching, on STO substrate, a definite islands separation and grain faceting. Growth parameters affect magnetic properties, making tunable the anisotropy energy in the range from 0.8 to 3.6 $\times$ $10^7 erg/cm^3$ and the coercive field from 2 to 29 kOe.

The satisfactory results have been exploited to obtain exchange coupled composite systems (ECC), characterized by a hard and soft layers coupled by exchange interaction, epitaxially grown on MgO and STO substrates. An innovative choice of soft material in ECC bilayers, with the $L1_0$-FePt/Fe_3Pt structure, has allowed the reduction of H_C value of about 80% compared to single FePt thin film, higher than in the previous studied $L1_0$-FePt/Fe systems [119]. The presence of the exchange-spring regime

is deeply influenced by soft layer parameters, such as thickness (2-5 nm), Fe content (75-80 at.%) and also by the substrate choice (STO or MgO). A micromagnetic model has been developed to study the magnetization reversal process in ECC systems, taking into account extrinsic properties (i.e. magnetic domain and layer interfaces).
In order to obtain ECC systems with graded anisotropy, as suggested to overcome the superparamagnetic limit and achieve higher areal densities in recording media [43, 56], an original approach has been proposed. In particular, the magnetic anisotropy has been graded along the FePt film thickness by Ar^+ ions irradiation, creating regions with different magnetic properties. Changing ion beam parameters (i.e., ion dose, energy, angle of incidence) has given rise to changes in the magnetic regimes (from irreversible to partially reversible behavior) and a large reduction of coercive field without causing morphological damage on film surface. The magnetic properties have been studied as a function of film thickness and angle of incidence at optimized ion beam parameters, also taking advantages of Monte Carlo simulations.
Finally, high quality epitaxial Fe_3O_4/MgO/FePt heterostructures have been grown and microfabricated to obtain magnetic tunnel junctions (MTJs) by means of optical lithography. Magnetic resistance has been studied for different barrier thickness showing an inverse tunnel magnetic resistance (TMR) for a barrier thickness value of 1.5 nm. The appearance of inverse TMR is due to the presence of Fe_3O_4/MgO interface [175]. The low barrier interface quality is accountable for the low absolute value of TMR ($\approx$ 0.5-1.5 %), and appears of normal TMR with thicker barrier. These aspects need to be optimized by modifying the growth conditions.
FePt alloy has been shown to be a versatile material for application in new nanocomposites recording media. In particular, innovative exchange-spring systems can be obtained exploiting the interface between a hard and soft FePt magnetic phases or a graded anisotropy profile obtained by irradiating a $L1_0$-FePt film. The goal achieved in both cases is the possibility to tailor the magnetic properties changing system characteristics (i.e., thickness or Fe content of the soft phase, substrate choice, ion irradiation).
Moreover, in the heterostructure for magnetic tunnel junctions (MTJs), the original choice of $L1_0$-FePt layer as electrode has introduced a suitable magnetization geometry for spin-torque oscillator devices, highlighting the potential use of $L1_0$-FePt, with perpendicular magnetic anisotropy, for high-density spintronic applications [9].

Bibliography

[1] F. Akagi. et al. *J. Magn. Magn. Mat.*, 324:309, 2012.

[2] Y. Wang. et al. *J. Appl. Phys.*, 109:07B730, 2011.

[3] S.N. Piramanayagam. et al. *J. Magn. Magn. Mat.*, 321:485, 2009.

[4] D.P. Arnold. et al. *J. Microelectromech S.*, 18:1255, 2009.

[5] S. Wolf. et al. *Science*, 294:1488, 2001.

[6] J. Camarero. et al. *J. Mat. Chem.*, 19:1678, 2009.

[7] Sun C.-J. *Ieee T. Magn*, 46:1795, 2010.

[8] T. Moriyama. et al. *J. Appl. Phys.*, 95:6789, 2004.

[9] S. Mangin. et al. *Nat. Mater.*, 5:210, 2006.

[10] Paoluzi A. Lectures on magnetism and magnetic materials. Technical report, PhD in Material Science, University of Parma., 2009.

[11] Lifshitz L.D., Landau E.M. *Electrodynamics of Continuous Media, Second Edition: Volume 8*. 1986.

[12] J.C. Slonczewski. *J. Appl. Phys.*, 44:1759, 1973.

[13] F. Casoli. et al. *J. Appl. Phys.*, 103:043912, 2008.

[14] S. Okamoto. et al. *Phys. Rev. B*, 66:024413, 2002.

[15] L. Callegaro. et al. *J. Phys. D.*, 36:2036, 2003.

[16] W. F. Brown. *Phys. Rev.*, 105:1479, 1957.

[17] S. Goolaup. et al. *Eur. Phys. J. B.*, 44:259, 2005.

[18] E. C. Stoner and E.P. Wohlfarth. *Phil. Trans. Roy. Soc.*, A240:599, 1948.

[19] T. Kaneyoshi. et al. *J. Phys.: Condens. Matter*, 3:4497, 1991.

[20] M.R. Scheinfein. et al. *Phys. Rev. Lett.*, 63:668, 1989.

[21] R. Bergholz. et al. *J. Magn. Magn. Mat.*, 45:389, 1984.

[22] M. Getzlaff. *Fundamentals of Magnetism*. Springer, 2008.

[23] F. Casoli. et al. *Acta Materialia*, 58:3594, 2010.

[24] P.J.H. Bloemen. et al. *Phys. Rev. B*, 50:13505, 1994.

[25] F. Albertini. et al. *J. Appl. Phys.*, 104:053907, 2008.

[26] D. Ravelosona. et al. *Appl. Phys. Lett.*, 76:236, 2000.

[27] J. F. Ziegler, J. P. Biersack, and M. D. Ziegler. *The Stopping and Range of Ions in Matter*. 1985.

[28] D. Litvinova. et al. *Journ. Magn. Magn. Mat.*, 283:128–132, 2004.

[29] D. Ravelosona. et al. *J. Phys. D.*, 37:R179, 2004.

[30] J.P. Nozieres. et al. *Nucl. Instrum. Methods Phys. Res. B*, 146:250, 1998.

[31] S. Konings. et al. *J. Appl. Phys.*, 98:054306, 2005.

[32] V. Parekh. et al. *J. Appl. Phys.*, 101:083904, 2007.

[33] E. Kneller. et al. *IEEE Trans. Magn.*, 27:3588, 1991.

[34] D. Suess. et al. *Appl. Phys. Lett.*, 87:012504, 2005.

[35] R. Skomski. et al. *Phys. Rev. B*, 48:15812, 1993.

[36] T. Leineweber. et al. *J. Magn. Magn. Mat.*, 176:145, 1997.

[37] N. Sousa. et al. *Phys. Rev. B*, 82:104433, 2010.

[38] G. Asti. et al. *Phys. Rev. B*, 69:174401, 2004.

[39] K. Mibu. *J. Magn. Magn. Mat.*, 163:75, 1996.

[40] E. Fullerton. et al. *Phys. Rev. B*, 58:12193, 1998.

[41] Y.S. Lin. et al. *J. Appl. Phys.*, 40:604, 1969.

[42] R.F. Sabityanov. et al. *Phys. Rev. B*, 58:12071, 1998.

[43] R.H. Victora. et al. *IEEE Trans. Magn.*, 41:3136, 2005.

[44] J. Dean. et al. *Appl. Phys. Lett.*, 92:142505, 2008.

[45] D. Suess. *Appl. Phys. Lett.*, 89:113105, 2006.

[46] D. Suess. et al. *Appl. Phys. Lett.*, 92:173111, 2008.

[47] G. T. Zimanyi. *J. Appl. Phys.*, 103:07F543, 2008.

[48] M. Johnson. et al. *Phys. Rev. Lett.*, 55:1790, 1985.

[49] M. N. Baibich. et al. *Phys. Rev. Lett.*, 61:2472–2475, 1988.

[50] G. Binasch. et al. *Phys. Rev. B*, 39:4828, 1989.

[51] R. Wood. et al. *J. Magn. Magn. Mat.*, 321:555, 2009.

[52] N. Robertson. et al. *IEEE Trans. Magn.*, 33:2818, 1997.

[53] S. Iwasaki. et al. *IEEE Trans.*, 15(6), 1979.

[54] M. Futamoto. et al. *J. Magn. Magn. Mat.*, 235:281, 2001.

[55] D. Weller. et al. *Appl. Phys. Lett.*, 61:2726, 1992.

[56] D. Suess. et al. *IEEE Trans. Magn.*, 41:537, 2005.

[57] D. Goll. et al. *Physica B.*, 403:338–341, 2008.

[58] A.Y. Dobin. et al. *Appl. Phys. Lett.*, 89:062512, 2006.

[59] M. Ghidini. et al. *J. Magn. Magn. Mat.*, 316:159, 2007.

[60] D. Suess. *J. Magn. Magn. Mat.*, 308:183, 2007.

[61] D.C. Crew. et al. *J. Magn. Magn. Mat.*, 233:257, 2007.

[62] F. Casoli. et al. *IEEE Trans. Magn.*, 41:3877, 2005.

[63] D. Hahn. et al. *IEEE Trans. Magn.*, 46:1866, 2010.

[64] R. Skomski. et al. *J. Appl. Phys.*, 103:07F531, 2008.

[65] B.D. Terris. et al. *J. Phys. D.*, 38:R199, 2005.

[66] R. Sbiaa. et al. *J. Appl. Phys.*, 105:073904, 2009.

[67] T. Bublat. et al. *Nanotechnology*, 22:315301, 2011.

[68] K. Naito. et al. *IEEE Trans. Magn.*, 38:1949, 2002.

[69] A. Kikitsu. et al. *IEEE Trans. Magn.*, 43:3685, 2007.

[70] Z. Li. et al. *Phys. Rev. B*, 69:134416, 2004.

[71] T. Matsumoto. et al. *Appl. Phys. Lett.*, 93:031108, 2008.

[72] W.A. Challener. et al. *Nature Photon*, 3:220, 2009.

[73] V. Rivkin. et al. *Appl. Phys. Lett.*, 89:252507, 2006.

[74] S. Li. et al. *J. Appl. Phys.*, 105:07B909, 2009.

[75] N. H. Mott. *Proc. Roy. Soc. London Ser. A*, 153:699, 1936.

[76] J.S. Moodera. et al. *Phys. Rev. Lett.*, 74:3273, 1995.

[77] E.I. Rashba. *Phys. Rev. B*, 62:R16269, 2000.

[78] S. Tehrani. et al. *Magnetics*, page 32783, 1999.

[79] J.C. Slonczewski. et al. *J. Magn. Magn. Mat.*, 159:L1, 1996.

[80] L. Berger. *Phys. Rev. B*, 54:9353, 1996.

[81] W. Weber. et al. *Science*, 291:1015, 2001.

[82] D.C. Ralph. et al. *J. Magn. Magn. Mat.*, 320:1190, 2008.

[83] A. Nazarov. et al. *J. Appl. Phys.*, 103:07A503, 2008.

[84] S. Sanvito. et al. *J. Comput. Theor. Nanosci.*, 3:624, 2006.

[85] V.I. Krinichnyi. *Synth. Met.*, 108:173, 2000.

[86] F.J. Jedema. et al. *Nature*, 410:345, 2001.

[87] J. Akerman. *Science*, 308:508, 2005.

[88] J.M. Manriquez. et al. *Science*, 252:1415, 1991.

[89] B. Gohler. et al. *Science*, 331:894, 2011.

[90] G.K. Wehner and G.S. Anderson. *Handbook of thin film technology.* Mc Graw-Hill, 1970.

[91] B. Chapman. *Glow Discharge Processes: Sputtering and Plasma Ecthing.* Wiley, 1980.

[92] G. Binning. et al. *Phys. Rev. Lett.*, 49:57, 1982.

[93] G. Binning. et al. *Phys. Rev. Lett.*, 56:930, 1986.

[94] S. Kumar. et al. *IEEE Trans. Magn.*, 41:1200, 2005.

[95] S. Onoda. et al. *Phys. Rev. Lett.*, 97:126602, 2006.

[96] O.A. Ivanov. et al. *Fiz. Metal. Metalloved.*, 35:81, 1973.

[97] L. Graf. *Physik Z.*, 36:544, 1935.

[98] B. Zhang. et al. *Scripta Met. Mater.*, 25:1577, 1991.

[99] W.A. Soffa. et al. *Solid State Phenomena*, 172-174:608, 2011.

[100] T.B. et al. Massalski. *Binary alloy phase diagrams.* American Society for Metals, 1986.

[101] Y.K. Takahashi. et al. *Jpn. J. Appl. Phys.*, 40:L1367, 2001.

[102] S. Jeong. et al. *IEEE Trans. Magn.*, 37:1299, 2001.

[103] C.H. Lai. et al. *Appl. Phys. Lett.*, 85:4430, 2004.

[104] C.H. Lai. *Appl. Phys. Lett.*, 83:4550, 2003.

[105] Z.L. Zhao. et al. *Appl. Phys. Lett.*, 88:052503, 2006.

[106] T. Maeda. et al. *Appl. Phys. Lett.*, 80:2147, 2002.

[107] T. Bublat. et al. *J. Appl. Phys.*, 108:113910, 2010.

[108] M. Weisheit. et al. *Thin Solid Film*, 515:3952, 2007.

[109] T. Itoh. et al. *Ieee T. Magn*, 41:3217, 2005.

[110] F. Casoli. *Perpendicular anisotropy and exchange-spring properties in magnetic thin films and multilayers*. PhD thesis, Matter Physics, University of Parma, 2005.

[111] D.C. Berry. et al. *J. Appl. Phys.*, 102:024912, 2007.

[112] Y.S. Yu. et al. *J. Phys. D.: Appl. Phys.*, 41:245003, 2008.

[113] T. Seki. et al. *J. Appl. Phys.*, 96:1127, 2004.

[114] J.S. Chen. et al. *Journ. Magn. Magn. Mat.*, 303:309, 2006.

[115] M. Bibes. et al. *IEEE Trans. Electron Device*, 54:1003, 2007.

[116] S.N. Hsiao. *Appl. Phys. Lett.*, 94:232505, 2009.

[117] L.T. Nguyen. et al. *J. Appl. Phys.*, 95:7492, 2004.

[118] A. Mougin. *J. Phys. D.: Appl. Phys.*, 43:365002, 2010.

[119] F. Casoli. et al. *Appl. Phys. Lett.*, 92:142506, 2008.

[120] Y.F. Ding. et al. *J. Cryst. Growth*, 276:111, 2005.

[121] C. Zha. et al. *Ieee T. Magn*, 44:3539, 2008.

[122] J.S. Kim. et al. *J. Appl. Phys.*, 99:053906, 2006.

[123] Y.K. Takahashi. et al. *J. Magn. Magn. Mat.*, 267:248, 2003.

[124] A. Cebollada. et al. *Phys. Rev. B*, 50:3419, 1994.

[125] G.R. Harp. et al. *Mater. Res. Soc. Symp. Proc.*, 313:493, 1993.

[126] M.R. Visokay. et al. *Appl. Phys. Lett.*, 66:1692, 1995.

[127] Y.F. Ding. et al. *J. Magn. Magn. Mat.*, 303:238, 2006.

[128] A. Cebollada. *Magnetic Nanostructures*. American Scientific, 2002.

[129] R.A. Ristau. et al. *J. Appl. Phys.*, 86:4527, 1999.

[130] H.X. Li. et al. *J. Appl. Phys.*, 101:093911, 2007.

[131] Y.K. Takahashi. *J. Magn. Magn. Mat.*, 267:248, 2003.

[132] S. Hong. et al. *J. Appl. Phys.*, 97:084315, 2005.

[133] J Honolka. et al. *Phys. Rev. Lett.*, 102:067207, 2009.

[134] Shima T. et al. *Appl. Phys. Lett.*, 81:1050, 2002.

[135] Peng. et al. *J. Appl. Phys.*, 99:08F907, 2006.

[136] Z. Dai. et al. *Nano Letters*, 1:443, 2001.

[137] P. Seneor. et al. *Appl. Phys. Lett.*, 74:4017, 1999.

[138] Z. Szotek. et al. *J. Phys.: Condens. Matter*, 16:S5587, 2004.

[139] E.J.M. Verwey. *Nature*, 144:327, 1939.

[140] Julia Maria Orna Esteban. Epitaxial growth of half-metallic magnetic oxide thin films by pulsed laser deposition. 2010.

[141] D.T. Margulies. et al. *J. Appl. Phys.*, 75:6097, 1994.

[142] M.G. Chapline. et al. *J. Appl. Phys.*, 97:123901, 2005.

[143] A. Fernandez-Pacheco. et al. *Phys. Rev. B*, 78:212402, 2008.

[144] A. Fernandez-Pacheco. et al. *Appl. Phys. Lett.*, 95:262108, 2009.

[145] J.M. De Teresa. et al. *Mic. Eng.*, 84:1660, 2007.

[146] T. Maruryama. et al. *J. Appl. Phys.*, 29:L810, 1990.

[147] J.S. Corneille. et al. *Surf. Sci.*, 306:269, 1994.

[148] S.M. Lee. et al. *Appl. Surf. Sci.*, 175:517, 2001.

[149] X.Y. Chen. et al. *Appl. Surf. Sci.*, 135:233, 1998.

[150] L. Dong. et al. *J. Appl. Phys.*, 89:4105, 2001.

[151] Y. Misaki. et al. *J. Vac. Sci. Technol.*, A15:48, 1997.

[152] B.D. Terris. *J. Magn. Magn. Mat.*, 321:512, 2009.

[153] E. Kondorsky. *J. Appl. Phys.*, 2:161, 1940.

[154] K.R. Coffey. et al. *J. Appl. Phys.*, 92:4553, 2002.

[155] D. Goll. et al. *Appl. Phys. Lett.*, 93:152512, 2008.

[156] A. Goncharov. et al. *Appl. Phys. Lett.*, 91:222502, 2007.

[157] T.-J. Zhou. *Appl. Phys. Lett.*, 94:152505, 2009.

[158] G. Choe. et al. *Ieee T. Magn*, 47:55, 2011.

[159] D. Goll. et al. *J. Appl. Phys.*, 104:083903, 2008.

[160] S. Mitani. et al. *Ieee T. Magn*, 41:2606, 2007.

[161] P. De Person. et al. *Phys. Rev. B*, 76:184402, 2007.

[162] M. Yoshikawa. et al. *Ieee T. Magn*, 44:2577, 2008.

[163] N. Nashimura. et al. *J. Appl. Phys.*, 91:5246, 2002.

[164] H. Ohmori. et al. *J. Appl. Phys.*, 103:07A911, 2008.

[165] D.A. Kent. *Nat. Mater.*, 9:699, 2010.

[166] D.A. Kent. et al. *Appl. Phys. Lett.*, 84:3897, 2004.

[167] R. Sbiaa. et al. *Appl. Phys. Lett.*, 99:092506, 2011.

[168] T. Seki. et al. *Appl. Phys. Lett.*, 88:172504, 2006.

[169] S. Yuasa. et al. *J. Phys. D.: Appl. Phys.*, 40:R337, 2007.

[170] W.H. Butler. et al. *Phys. Rev. B*, 63:054416, 2001.

[171] J.P. Velev. et al. *Phys. Rev. Lett.*, 95:216601, 2005.

[172] Y. Taniguchi. et al. *Ieee T. Magn*, 44:2585, 2008.

[173] G. Zhou. et al. *J. Appl. Phys.*, 99:08J111, 2006.

[174] A.P. Mihai. et al. *Phys. Rev. B*, 77:060401R, 2008.

[175] T. Kado. *Appl. Phys. Lett.*, 92:092502, 2008.

[176] K.D. Belashchenko. et al. *Phys. Rev. B*, 72:140404R, 2005.

[177] J.M. Teixeira. et al. *Appl. Phys. Lett.*, 96:262506, 2010.

Publications

P-1 P. Lupo, J. Orna, F. Casoli, L. Nasi, S. Fabbrici, P. Ranzieri, R. Cabassi, F. Bolzoni, D. Calestani, P. Algarabel, L. Morellon, F. Albertini, *Tuning morphology and magnetism of epitaxial $L1_0$-FePt films by exploiting the misfit with $SrTiO_3$ (100) and MgO (100) substrates.*, submitted on *Acta Mat.* (2011).

P-2 A. di Bona, P. Luches, S. DAddato, S. Valeri, F. Albertini, F. Casoli, P. Lupo, *FePt graded media obtained by ion irradiation.*, submitted on *J. Appl. Phys.* (2011).

P-3 G. Varvaro, F. Albertini, E. Agostinelli, F. Casoli, D. Fiorani, S. Laureti, P. Lupo, P. Ranzieri and A.M. Testa, *Magnetization reversal mechanism in perpendicular exchange-coupled Fe/$L1_0$-FePt bilayers.*, submitted at *Phys. Rev. B* (2012).

P-4 A. di Bona, P. Luches, S. DAddato, S. Valeri, F. Albertini, F. Casoli, P. Lupo, *Graded anisotropy media by ion irradiation of $L1_0$-FePt.* to be submitted on *Appl. Phys. Lett.* (2012).

This Thesis work has produced over twenty contribution to national and international scientific conferences.